

**FABRICATION AND CHARACTERISATION OF GRAPHENE
OXIDE SATURABLE ABSORBER FOR Q-SWITCHED FIBER
LASER GENERATION**

AHMAD ZARIF BIN ZULKIFLI

**THESIS SUBMITTED IN FULFILMENT OF THE
REQUIREMENTS FOR THE DEGREE OF DOCTOR OF
PHILOSOPHY**

**FACULTY OF ENGINEERING
UNIVERSITY OF MALAYA
KUALA LUMPUR**

2015

UNIVERSITI MALAYA
ORIGINAL LITERARY WORK DECLARATION

Name of Candidate: ANIMAD ZARIF BIN ZULKIFLI (I.C/Passport No: 841211-14-6293)

Registration/Matric No: KMA110040

Name of Degree: DOCTOR OF PHILOSOPHY

Title of Project Paper/Research Report/Dissertation/Thesis ("this Work"):

FABRICATION AND CHARACTERISATION OF GRAPHENE OXIDE SATURABLE ABSORBER FOR Q-SWITCHED FIBER LASER GENERATION

Field of Study: PHOTONICS

I do solemnly and sincerely declare that:

- (1) I am the sole author/writer of this Work;
- (2) This Work is original;
- (3) Any use of any work in which copyright exists was done by way of fair dealing and for permitted purposes and any excerpt or extract from, or reference to or reproduction of any copyright work has been disclosed expressly and sufficiently and the title of the Work and its authorship have been acknowledged in this Work;
- (4) I do not have any actual knowledge nor do I ought reasonably to know that the making of this work constitutes an infringement of any copyright work;
- (5) I hereby assign all and every rights in the copyright to this Work to the University of Malaya ("UM"), who henceforth shall be owner of the copyright in this Work and that any reproduction or use in any form or by any means whatsoever is prohibited without the written consent of UM having been first had and obtained;
- (6) I am fully aware that if in the course of making this Work I have infringed any copyright whether intentionally or otherwise, I may be subject to legal action or any other action as may be determined by UM.

Candidate's Signature



Date: 1/8/2015

Subscribed and solemnly declared before,



Witness's Signature

Date: 01/08/2015

Name:

Designation: Dr. Sulaiman Wadi Harun
Professor
Dept. of Electrical Engineering
University of Malaya
50603 Kuala Lumpur

ABSTRACT

Graphene oxide (GO) material is produced through chemical oxidation of graphite to produce large scale of graphene material by chemical reduction of GO. Its hydrophilic property and kinetically stable in colloidal suspensions allows new saturable absorber (SA) fabrication technique to be explored suited with the optical fiber technology where the graphene and carbon nanotube could not achieve due to their chemical properties limitation. In this regard, GO can be used as an alternative material to build SA device in generating Q-switched fiber laser. Such fiber laser can be used in various applications such as in range finding, remote sensing and so on that utilize high pulse energy and short pulse width. In this thesis, two different types of GOSA devices have been successfully fabricated and characterised for Q-switched fiber laser generation at the telecommunication C-band and eye-safe 2 micron band. The first GOSA device is fabricated from pure graphite using simplified's Hummer's method to produce 0.5 mg/mL GO colloidal suspension. Then a film form is yielded on a 90 mm petri dish through drop-casting method. Raman spectrum analysis on the defect density of the film via the intensity ratio value (I_D/I_G) reveals that the fabricated GO has high degree of crystalline defect and some partially retain aromatic sp^2 carbon ring structure which is mainly responsible for saturable absorption. The Q-switched fiber laser at C-band, has a Q-switched threshold of 65 mW with a maximum average output power of 0.11 mW, and pulse energy of 4.3 nJ. The narrowest pulse width of 7.7 μ s and a maximum repetition rate of 27.2 kHz are obtained at the maximum pump power. The second GOSA device is fabricated via optical deposition method by having graphite oxide nanopowder dispersed in water-contained beaker and deposited on a fiber ferrule facet. A comparison analysis on the intensity ratio (I_D/I_G) and effective aromatic cluster correlation length, L_{Aeff} suggests that GOSA by optical deposition ($I_D/I_G=0.92$) has higher capacity for saturable absorption than the GOSA film ($I_D/I_G=0.86$) due to having

larger effective aromatic cluster size and more aromatic rings. The Q-switched fiber laser at 2 micron region using the optically deposited GO layers has a threshold of 125 mW with a maximum pulse repetition rate of 16.0 kHz and minimum pulse width of 9.8 μ s. The maximum average output power of 0.3 mW and pulse energy of 18.8 nJ were obtained. In the third system, a commercial GO in a paper form has been compared with the GO film to evaluate the structure issue of the film that leads to nonsaturable loss. The GO paper has been successfully been utilized to generate narrow spacing Q-switched dual-wavelength fiber laser at the C-band region which will find useful for terahertz signal generation. This research work in generating Q-switched fiber lasers using the GOSAs have shown some potential where further system optimization is required to find their practical applications. Moreover, the advantages of GO properties has proven to provide an efficient solution that reduce time and cost to fabricate the saturable devices.

ABSTRAK

Bahan GO dihasilkan melalui pengoksidaan kimia daripada grafit untuk menghasilkan bahan grafen yang berskala besar melalui kaedah pengurangan kimia GO. Sifat GO yang hidrofilik dan juga penggantungan akueus yang stabil secara kinetik membolehkan teknik baharu fabrikasi peranti penyerap penepuan (SA) diterokai melalui kaedah teknologi gentian optik di mana grafen dan CNT tidak dapat dicapai disebabkan oleh sifat-sifat kimianya yang terhad. Dalam hal ini, GO boleh digunakan sebagai bahan alternatif untuk membina peranti SA dalam menjana laser gentian suis-q. Laser gentian tersebut boleh digunakan dalam pelbagai aplikasi, termasuklah penemuan had jarak, penderiaan jauh, dan sebagainya yang menggunakan tenaga nadi tinggi dan lebar denyut pendek. Dalam tesis ini, dua jenis peranti GO penyerap penepuan yang berbeza telah berjaya difabrikasikan dan dicirikan untuk generasi laser gentian suis-q di telekomunikasi band-C dan mata-selamat 2 band mikron. Peranti GOSA pertama diperbuat dari grafit tulen menggunakan kaedah Hummer yang dipermudahkan untuk menghasilkan 0.5 mg/mL GO penggantungan koloid. Kemudian, pementukan filem dihasilkan di atas piring petri 90 mm melalui kaedah titisan pemutus. Raman analisa spektrum terhadap kepadatan kerosakan melalui nilai nisbah keamatan (I_D/I_G) mendedahkan bahawa fabrikasi GO mempunyai kadar kerosakan hablur yang tinggi di samping sebahagian struktur kelompok aromatik karbon sp^2 dikekalkan di mana ia bertanggungjawab ke atas penyerapan tepu. Laser gentian suis-q di band-C, mempunyai ambang suis-Q 65 mW dengan kuasa maksima purata pengeluaran 0.11 mW, dan tenaga nadi 4.3 nJ. Manakala, lebar denyut sempit 7.7 μs dan kadar pengulangan maksimum 27.2 kHz diperoleh pada kuasa pam yang maksimum. Peranti GOSA yang kedua telah difabrikasikan melalui teknik pemendapan optik di mana serbuk nano grafit oksida yang disuraikan di dalam bikar yang mengandungi air dan didepositkan ke atas permukaan sirat ferrule. Analisa perbandingan nisbah keamatan (I_D/I_G) dan keberkesanan kelompok

aromatik panjang korelasi, L_{Aeff} mencadangkan bahawa GOSA oleh pemendapan optik ($I_D/I_G=0.92$) mempunyai kapasiti yang lebih tinggi untuk penyerapan tepu berbanding filem GOSA ($I_D/I_G = 0.86$) kerana saiz keberkesanan kelompok aromatiknyanya yang lebih besar dan jumlah cincin aromatik yang lebih tinggi. Laser gentian suis-q pada 2 band mikron yang menggunakan GOSA oleh pemendapan optik mempunyai suis-q ambang 125 mW dengan kadar pengulangan nadi maksimum 16.0 kHz dan lebar denyut minima sebanyak 9.8 μ s. Maksimum purata kuasa keluaran yang diperoleh ialah 0.3 mW manakala tenaga nadi sebanyak 18.8 nJ. Dalam sistem yang ketiga, GO komersial dalam bentuk kertas telah dibandingkan dengan filem GO untuk menilai isu struktur filem tersebut yang membawa kepada kehilangan tidak tepu. Kertas GO telah berjaya digunakan untuk menjana jarak sempit dwi-panjang gelombang laser gentian suis-q di kawasan band-C yang didapati berguna untuk generasi isyarat terahertz. Kerja-kerja penyelidikan dalam menjana laser gentian suis-q yang menggunakan GOSA telah menunjukkan potensi dan pengoptima sistem lanjut diperlukan untuk membawa mereka kepada aplikasi yang praktikal. Selain itu, kelebihan ciri-ciri GO telah terbukti dapat memberikan penyelesaian yang cekap di mana ia mampu mengurangkan masa dan kos untuk membina peranti penyerap penepuan.

ACKNOWLEDGEMENTS

Throughout the time I spent at the Photonics Research Center (PRC) in University of Malaya, there have been many people whom have helped me to complete this research work. It is a pleasure to thank a few of them here. First and foremost, I would like to thank my supervisor, Professor Dr. Sulaiman for reviewing and guiding me in the thesis writing. He is a hard working person and always comes to the center even in weekend. Through his encouragement and motivation, I managed to complete this thesis.

I would like to thank my second supervisor Professor Dr. Harith Ahmad for his willingness to undertake supervision in my experimental work and for giving me so much multi-discipline training experience and exposure to researchers from other fields. This provided me a much broader view of the research environment and inspired many novel ideas. This work would not be possibly done without their invaluable advices and guidance. I have learned so much from them, not only how to perform research in the right and most effective way but also how to be a responsible person. I have been fortunate to work under them who cared about my developments both as a researcher and as a person. I have benefited a lot from learning Q-switched fiber lasers, laser diode and material analysis throughout the time spent here.

Also my special appreciation goes to my family and friends. I would have not continued my PhD without their continuous encouragement and supports. Lastly, I would like to thank University of Malaya for sponsoring my PhD program under BrightSparks scholarship and giving me a great education, and for making my life here enjoyable.

TABLE OF CONTENTS

Abstract	iii
Abstrak	v
Acknowledgements	vii
Table of contents	viii
List of figures	xi
List of tables	xvi
List of symbols and abbreviations.....	xvii
 CHAPTER 1: INTRODUCTION.....	1
1.1 Background.....	1
1.2 Research motivation	3
1.3 Objectives and scopes of present work.....	4
1.4 Thesis overview	6
 CHAPTER 2: THEORETICAL REVIEW ON PASSIVELY Q-SWITCHED FIBER LASER OPERATION AND SATURABLE ABSORBER PRINCIPLE	8
2.1 Introduction.....	8
2.2 Q-switching in fiber laser with saturable absorber	9
2.3 Differential rate equations	10
2.4 Q-switched threshold condition.....	13
2.5 Pulse-build up process	14
2.6 Saturable absorption parameters.....	17

2.7	Summary.....	21
-----	--------------	----

CHAPTER 3: FABRICATION AND CHARACTERISATION OF GRAPHENE

	OXIDE FILM AS SATURABLE ABSORBER	22
3.1	Introduction.....	22
3.2	Graphene Oxide molecular bonding and electronic band structures	23
3.3	Producing graphene oxide aqueous suspension from graphite flakes via chemical oxidation	29
3.4	Preparation of Graphene Oxide Film as Saturable Absorber via Drop-casting method33	
3.5	Characterization of Graphene Oxide Film using Raman spectroscopy technique	35
3.6	Summary.....	48

CHAPTER 4: Q-SWITCHED FIBER LASER BASED ON GRAPHENE OXIDE

	FILM USING A 21 CM LONG BISMUTH ERBIUM-DOPED FIBER AS THE GAIN MEDIUM.....	51
4.1	Introduction.....	51
4.2	Experimental arrangement for the proposed Q-switched Bi-EDF laser	52
4.3	Experimental results and discussion	57
4.4	Summary.....	72

CHAPTER 5: DEVELOPMENT OF GRAPHENE OXIDE SATURABLE

	ABSORBER VIA OPTICAL DEPOSITION FOR 2 μm Q-SWITCHED FIBER LASER APPLICATION.....	74
5.1	Introduction.....	74
5.2	Electric double layer of Graphene Oxide in water	76

5.3	Fabrication of Graphene Oxide Saturable Absorber via Optical Deposition	79
5.4	Characterization of GOSA and comparison study.....	87
5.5	Q-switched pulse train generation operating in 2 μm region using the developed GOSA 90	
5.5.1	Experimental arrangement	90
5.5.2	Performance of the Q-switched laser	93
5.6	Summary.....	102

CHAPTER 6: GRAPHENE OXIDE PAPER FOR THE GENERATION OF DUAL-WAVELENGTH Q-SWITCHED FIBER LASER.....104

6.1	Introduction.....	104
6.2	Reviews on the Fabrication Method and Structure of GO Paper	105
6.3	Characterisation of Graphene Oxide Paper	107
6.4	Experimental arrangement of Q-switched DWFL with Graphene Oxide Paper .	109
6.5	Performance of the Q-switched DWFL.....	112
6.6	Summary.....	118

CHAPTER 7: CONCLUSION AND FUTURE OUTLOOK.....120

6.1	Conclusion	120
6.2	Future work.....	125
	References	127
	List of Publications and Papers Presented	142

LIST OF FIGURES

Figure 2.1: Two- level system showing optically generated electron-hole pair formation in a saturable absorber with a) saturable absorption process and b) SA in saturation mode.....	9
Figure 2.2: The first pulse build-up process for Q-switched laser with saturable absorber	15
Figure 2.3: Pulse trains produced in a fiber laser with saturable absorber	16
Figure 2.4: Photon intensity, I versus distance, x for two different absorption coefficients.	18
Figure 2.5: The non-linear saturable absorption dynamics as a function of light intensity in Q-switching.....	20
Figure 3.1: 3-dimensional view of Crystalline Graphite's molecular structure.....	23
Figure 3.2: sp^2 carbon molecular bonding and geometry structures in a graphene sheet (a) 3-dimensional view (b) geometrical top view	24
Figure 3.3: Lerf–Klinowski model for a Graphene Oxide's molecular bonding structure (He et al., 1998, Lerf et al., 1998)	27
Figure 3.4: The electronic band structure (left panel) and density of states (DOS: right panel) of GO as calculated by Shang et al. (2012).....	28
Figure 3.5: Graphene oxide colloid with concentration of 0.5 mg/mL.....	30
Figure 3.6: UV-visible spectroscopy components and setup	30
Figure 3.7: The $\pi \rightarrow \pi^*$ and $n \rightarrow \pi^*$ transitions based on UV-visible absorption.....	31
Figure 3.8: Absorbance spectrum of graphene oxide aqueous suspension across UV-visible wavelengths at a steady state.....	32
Figure 3.9: Process flow in preparing Graphene Oxide Film	34
Figure 3.10: GO film on a FC/PC fiber ferrule face.....	34
Figure 3.11: SWCNT/PEO composite deposited on fiber ferrule facet	35

Figure 3.12: Energy diagram showing light scattering effect when light interact with molecule	37
Figure 3.13: Renishaw Raman Spectrometer components and setup	38
Figure 3.14: Raman spectrum of Graphene Oxide Film on a fiber ferrule.....	40
Figure 3.15: Raman spectrum of carbon nanotube on a fiber ferrule.	40
Figure 3.16: A_{1g} phonon eigenvectors (indicated by the red arrows) at the sp^2 aromatic ring cluster in GO sheet showing the alternating ring stretching behaviour.....	42
Figure 3.17: Electron band diagram showing the intervally process for the Raman scattering and A_{1g} phonon scattering (red line indicates the electron-phonon scattering event and the blue dotted line represents the Rayleigh scattering event).	42
Figure 3.18: E_{2g} phonon eigenvectors (indicated by red arrows) at the sp^2 aromatic cluster region at the GO sheet showing the in-plane bond-stretching motion of sp^2 carbon atoms pairs.....	43
Figure 3.19: Electron band diagram showing the intravalley process for the Raman scattering and E_{2g} phonon scattering.....	44
Figure 3.20: Top view of a graphene oxide plane showing the isolated aromatic cluster correlation length, L_A (blue circle indicates defect).....	46
Figure 4.1: Schematic of the GOSA assembly (not to scale).....	52
Figure 4.2: A ring Bi-EDFL configuration. WDM: wavelength division multiplexer; TBF: tunable bandpass filter; VOA: variable optical attenuator; PD: photodetector; OSC: oscilloscope; and OSA: optical spectrum analyser.	53
Table 4.1: Tunable band pass filter specifications.	56
Figure 4.3: Q-switched fiber laser measurement tools. Starting from the top left hand corner in clockwise direction: Optical spectrum analyser (Yokogawa-AQ6370C), radio frequency analyser (Anritsu - MS2665C) and oscilloscope (Le Croy 500 MHz).	57
Figure 4.4: ASE spectra of the Bi-EDF at various 1480 nm pump powers.....	58

Figure 4.5: Q-switched laser spectra at different wavelengths tuned by a TBF at a fixed pump power of 92 mW. The base power is set at 73 dBm for clarity.	59
Figure 4.6: Pulse train and a single pulse profile of the Q-switched Bi-EDFL under pump power of 92 mW at 1556 nm laser wavelength. The repetition rate of 21.8 kHz and pulse width of 11.7 μ s are obtained.....	61
Figure 4.7: Pulse train and a single pulse profile of the Q-switched Bi-EDFL under pump power of 118 mW at 1556 nm laser wavelength. The repetition rate of 27.2 kHz, and pulse width of 7.7 μ s are obtained.....	62
Figure 4.8: Pulse width and repetition rate characteristics of the Q-switched Bi-EDF laser at the wavelength of 1566 nm.....	64
Figure 4.9: Average output power and pulse energy of the Q-switched Bi-EDFL as a function of incident pump power.	67
Figure 4.10: Quasi-molecular orbital energy levels and electronic transitions for the saturable absorption process in graphene oxide material.....	67
Figure 4.11: Peak power of the Q-switched Bi-EDFL as a function of pump power.....	69
Figure 4.12: RF spectrum of a Q-switched pulse laser, at 1556 nm, as obtained from the RFSA at the pump power of 92 mW. The fundamental frequency of the pulse is 21.8 kHz. Inset shows the RF harmonics of the Q-switched pulse laser. The RFSA was set at a span of 25 kHz, with a Resolution Bandwidth and Video Bandwidth of 300 Hz.....	70
Figure 5.1: Simplified model of a graphene oxide basal plane with oxygen functional groups.....	76
Figure 5.2: Electric double layer of GO in water.....	77
Figure 5.3: An image of graphite oxide nanopowder.	79
Table 5.1: Graphite oxide nanopowder specifications.....	79
Figure 5.4: Optical deposition process for depositing GO layers on a fiber ferrule face.	80

Figure 5.5: Optical deposition mechanism which includes the heat convection and thermophoresis effects.	81
Figure 5.6: The optical fiber scope image of the GO-SA on a fiber ferrule face before (left) and after (right) optical deposition process. The dark areas are the GO layers, while the bright areas are the parts of the fiber ferrule not covered by the GO particles (Field of view = 400 μm x 300 μm , Resolution <1 μm).	86
Figure 5.7: Raman spectrum of the optically deposited Graphene Oxide on the fiber ferrule facet.	88
Figure 5.8: Setup of the proposed Q-switched TDFL with GO-based SA.	91
Table 5.2: Thulium-doped single mode fiber specifications.	91
Figure 5.9: Thulium-doped fiber ASE spectrum pumped at 128.8 mW.	93
Figure 5.10: Thulium-doped fiber laser spectra with and without the GO based SA and a curve fit that envelopes the Q-switched laser spectrum for FWHM measurement. The inset shows the ASE spectrum of the TDF.	94
Figure 5.11: Single pulse and a pulse train of a Q-switched laser at a pump power of 148mW.	96
Figure 5.12: Single pulse and a pulse train of a Q-switched laser at a pump power of 164 mW.	97
Figure 5.13: Repetition rate and pulse width curves as function of pump power.	98
Figure 5.14: Average output power and pulse energy curves as function of pump power.	100
Figure 5.15: Peak power as function of pump power.	100
Figure 5.16: Radio frequency measurement of Q-switched laser at a repetition rate of 12.2 kHz using RFSA, with inset showing the RF harmonics of the laser pulses.	102
Figure 6.1: Graphene oxide (GO) saturable absorber structures: a) GO paper, and b) GO film.	106

Figure 6.2: Microscopic image of a) Graphene Oxide (GO) paper surrounded by index matching gel b) Fiber ferule face showing the inner (dark area) and outer (bright area) sections of the ferule. The GO paper sits at the center of the inner section covering the fiber core.	108
Figure 6.3: Raman spectrum of Graphene Oxide paper measured using Renishaw Raman Spectroscopy.....	109
Figure 6.4: Experimental arrangement of the dual-wavelength Q-switched fibre laser.	110
Figure 6.5: Optical spectra of dual-wavelength laser; a) measured using low resolution OSA at CW operation, b) measured using high resolution OSA at (i) CW and (ii) Q-switched.....	113
Figure 6.6: The Q-switched dual-wavelength fiber laser pulse train pumped at 66 mW.	114
Figure 6.7: 6 different pulse traced of a single pulse profile pumped at 66 mW.....	115
Figure 6.8: Radio frequency spectrum of the Q-switched dual-wavelength fiber laser at the fundamental harmonic.....	116
Figure 6.9: Pulse width and repetition rate characteristics at different pump powers..	117
Figure 6.10: Average output power and pulse energy characteristics at different pump powers.	118

LIST OF TABLES

Table 4.1: Tunable band pass filter specifications.	56
Table 5.1: Graphite oxide nanopowder specifications.	79
Table 5.2: Thulium-doped single mode fiber specifications.	91

LIST OF SYMBOLS AND ABBREVIATIONS

γ	:	Inversion reduction factor
$h\nu$:	Photon energy
D_T	:	Thermophoretic mobility
E_g	:	Bandgap energy
I_D	:	Defect intensity
I_G	:	Graphitic intensity
L_D	:	Distance between defect
L_A	:	Correlation length
ASE	:	Amplified spontaneous emission
L_D	:	Distance between defect
L_A	:	Correlation length
Bi-EDF	:	Bismuth-erbium doped fiber
BNC	:	Bayonet Neill–Concelman connector
CNT	:	Carbon nanotube
Cr^{2+}	:	Chromium ion
CW	:	Continuous wave
DMF	:	Dimethylformamide
DWFL	:	Dual-wavelength fiber laser
EDF	:	Erbium-doped fiber
EDFL	:	Erbium doped fiber laser
Er^{3+}	:	Erbium ion
ER	:	Electrostatic repulsion
ESA	:	Excited state absorption
FC/PC	:	Ferrule connector/physical contact

FWHM	:	Full-width at half maximum
GO	:	Graphene Oxide
GOSA	:	Graphene Oxide Saturable Absorber
HUMO	:	Highest occupied molecular orbital
LD	:	Laser diode
LUMO	:	lowest unoccupied molecular orbital
OSA	:	Optical spectrum analyser
OSC	:	Oscilloscope
PC	:	Polarisation controller
PCF	:	Photonic crystal fiber
PD	:	Photodetector
PEO	:	Polyethylene oxide
PHB	:	Polarisation hole burning
PM	:	Power meter
RFSA	:	Radio frequency spectrum analyser
SA	:	Saturable Absorber
SESAM	:	Semiconductor Saturable Absorber Mirror
SMA	:	SubMiniature version A connector
SMF-28	:	Single mode fiber
SNR	:	Signal to noise ratio
TBF	:	Tunable band pass filter
TDF	:	Thulium-doped fiber
TDFL	:	Thulium-doped fiber laser
UV-vis	:	Ultra violet-visible
WDM	:	Wavelength division multiplexing

CHAPTER 1: INTRODUCTION

1.1 Background

The appearance of the Q-switching technology has a significant benefit in laser technology in many aspects due to the short pulse width and high pulse energy of the Q-switched laser. Such benefits include the development of non-linear optics (Geist et al., 1997, Stöppler et al., 2010) and technologies such as range finding, remote sensing, laser radar, telecommunication, spectroscopy and biotechnology (Stöppler et al., 2010, Kölbl et al., 2008, Kilpela et al., 2001, Vicente et al., 2004, Koechner, 2006, Skorczakowski et al., 2010, Wang et al., 2012). Q-switching a laser resonator will results in pulsed laser generation, having higher output power for short duration than would be achieved in continuous wave operation. Moreover, in some applications, Q-switched laser is much preferred to mode-locked laser due to having longer pulse duration and offer higher pulse energy.

Q-switching is enabled by modulating losses in a laser resonator either through actively such as using acoustic-optics (Delgado-Pinar et al., 2006, Zhao et al., 2007) and electro-optic modulators (El-Sherif et al., 2003, Michelangeli et al., 1986) or passively such as using saturable absorbers (Kurkov et al., 2011, Spühler et al., 1999, Hakulinen et al., 2007). Nevertheless, passively q-switching is still a prime choice for generating these high energy pulses due to its simpler in operation and provides important laser features such as compactness, high reliability and low cost. Furthermore, due to the advance development of optical fiber technology, Q-switched fiber based laser can be generated that offers small footprint, better beam quality and can easily dissipate heat as compared with laser based on bulk gain media (Svelto and Hanna, 1998).

Recently, passively Q-switched fiber lasers have been demonstrated using allotropes of carbon such as graphene (Wang et al. 2012, Sun et al. 2010) and carbon Nanotubes (CNTs) (Ahmad et al., 2013, Harun et al. 2012) which have been proven to be very capable as Saturable absorber (SA) for modulating losses in the resonator that works based on non-linear saturable absorption principle. These materials are proven to be capable as SAs which outperform the semiconductor saturable absorber mirror (SESAM) in terms of non-saturable loss, operation bandwidth, and fast absorber recovery time. Moreover, SESAMs exhibit complex and expensive quantum well structures and its fabrication requires molecular beam epitaxy on distributed Bragg reflectors (Okhotnikov et al., 2004, Agrawal et al., 2010). Meanwhile, graphene has seen substantial deployment as an SA due to its remarkable optical properties; having strong non-linear saturable absorption with a wide operating spectral range and ultrafast relaxation time.

Graphene sheets have been fabricated from many widely used methods such as micromechanical cleavage (Novoselov et al., 2004), epitaxial growth on silicon carbide (Berger et al., 2006), chemical vapour deposition (Reina et al., 2008) and chemical exfoliation (Stankovich et al., 2006, McAllister et al., 2007). Micromechanical cleavage technique has shown to be difficult to exfoliate single layer graphene from bulk graphite although it provides the lowest cost for fabricating graphene. Overall, the chemical exfoliation method is known to be the most effective and efficient way to prepare graphene sheets at large scale from bulk graphite (Stankovich et al., 2007), in which an intermediate process with graphene oxide (GO) sheets is involved (Stankovich et al., 2006, Stankovich et al., 2007). GO is produced through chemical oxidation of graphite (Hummers Jr et al., 1958, Brodie et al., 1860, Staudenmaier et al., 1898), that seems to provide the only solution for preparing highly dispersed and stable colloid of quasi two-

dimensional single layer crystallite carbon sheets. Then after which, pure crystallite graphene sheets are produced via chemical reduction of GO (Stankovich et al., 2007).

1.2 Research motivation

Recent research has discovered GO unique and useful properties (Haubner et al., 2010), where it can be used in many potential and practical applications such as in the electronics (Eda & Chhowalla, 2010, Eda et al., 2008, Wei et al., 2010), energy (Gao et al., 2011a, Li et al., 2010, Zhao et al., 2012), biosensor (Balapanuru et al., 2010) and optics (Loh et al., 2010, Gómez-Navarro et al., 2007, Eda et al., 2010). However, GO has lower quality of crystalline structure than graphene, due to the oxygen functional groups covalently bonded in its basal plane which makes it behave more of an insulator as compared to graphene.

A single layer of GO contains oxygen functional groups, with hydroxyl and epoxide are bonded at its basal plane, while carbonyl and carboxyl groups are located at the edges. These groups make GO highly hydrophilic and negatively charged in water or other solvent where the colloidal dispersion is found to be stable. As a result, these properties allow the colloidal suspension to be adaptable and able to process into macroscopic assemblies and structures at high volume. This opens up the possibilities in exploring new techniques of SA fabrication suited with the fiber technology where the CNT and graphene could not achieve due to their chemical properties limitation. The advantages of GO properties can provide an efficient solution that can reduce time, resource and cost to fabricate the SA device. With this background and abstraction, a research work is needed to provide the evident and necessary information regarding to the GO SA fabrication capability and its Q-switched fiber laser performance. This research work certainly can bring contribution to many fields such as in photonics, fiber laser industry, telecommunication and material engineering.

1.3 Objectives and scopes of present work

The main objective of this research work is to generate Q-switched fiber laser by using saturable absorber (SA) that will be fabricated based on graphene oxide (GO) material to provide simpler and cost-effective solution instead of using graphene, CNT and SESAM SAs. Specifically, the scopes of the research work and objectives are described as followed:

1) Fabrication and characterisation of GO film

- To fabricate pure GO colloidal suspension with a concentration of 0.5 mg/mL using simplified Hummers method as demonstrated by Huang et al. (2011).
- To characterise and analyse the GO colloidal suspension using the UV-visible spectroscopy technique to confirm the presence of GO material via the UV-visible absorption spectrum signatures.
- To fabricate GO in a film form on a 90 mm petridish through drop-casting method.
- To characterise the GO film using Raman spectroscopy technique and to make comparison with the measured CNT Raman spectrum.
- To specifically modify relationship model of I_D/I_G intensity ratio with an effective aromatic cluster correlation length based from Ferrari and Robertson (2000) for GO material, in order to evaluate the degree of defect and to estimate the saturable absorption.

2) Generation of Q-switched fiber laser at the C-band using the GO film

- To experimentally generate Q-switched fiber laser using 21 cm length of Bismuth-erbium doped fiber (Bi-EDF) as a gain medium and the GO film in a ring configuration setup.

-To measure and discuss the measured Q-switched laser performance with the established Q-switched laser theories.

3) Fabrication and characterisation of optically deposited GO layers on a fiber ferule.

-To deposit GO layers onto a fiber ferule facet using optical deposition method. This is performed by mixing Graphite oxide powder in a beaker-contained water to deposit GO layers on fiber ferule facet without the use of chemical agent or other techniques for material dispersion. In addition, the optical deposition theory will be presented in order to evaluate the fabrication process.

-To characterise the deposited GO layers using Ramanspectroscopy technique to confirm the presence of the GO material on the fiber ferule. In addition, a material comparison analysis with the GO film will be covered to evaluate the density of defect and the saturable absorption from the samples.

4) Generation Q-switched fiber laser at the 2 micron band using the deposited GO layers.

-To experimentally generate Q-switched fiber laser using thulium-doped fiber as gain medium and the deposited GO layers as SA.

-To measure and evaluate the Q-switched laser performance.

5) Generation of Q-switched dual-wavelength fiber laser using GO in a paper form.

-To review and compare the material structure of the GO paper with the GO film.

- To experimentally generate Q-switched dual-wavelength fiber laser at C-band using the GO paper.
- To make comparison on the optical spectra measurements of the dual-wavelength lasers using low and high resolution optical spectrum analysers.
- To measure and evaluate the Q-switched laser performance.

1.4 Thesis overview

This thesis is organized into 7 chapters. After this introduction, in chapter 2, the theoretical review and the modification of the differential rate equations and pulse-build up equations to describe Q-switched fiber laser operation in a unidirectional ring configuration setup will be presented. In addition, the saturable absorber principle which describes the non-linear saturable absorption at the micro- and macro-scopic scales will also be reviewed. Here, the ideas of generating Q-switched laser is clearly seen which motivate us to work on the GO based saturable absorber to generate Q-switched fiber lasers.

In Chapter 3, the GO molecular bonding and energy band structures will be presented to guide in the SA fabrication process and characterisation analysis. The fabrication method of a pure GO in solution form will be presented. Then, it will be characterised based on UV-visible absorption spectrum. The UV-visible spectrum analysis will provide the information regarding to the number of the sp^2 aromatic rings and confirm the yield of GO colloidal suspension. Then, the fabrication method of a solid-state GO in a film form will be demonstrated. The Raman spectrum analysis will be performed to characterise the film that gives valuable information regarding to its density of defect and saturable absorption. Here, the theory related to Raman spectrum

measurement specifically for carbon material will be covered to accurately analyse the GO Raman spectrum and comparison will be made with the CNT Raman spectrum.

In Chapter 4, the successfully fabricated GOSA will be incorporated in a fiber laser resonator to generate Q-switched laser. The setup will include a 21 cm long of Bi-EDF which is used as a gain medium to study the gain and loss dynamics along with the GOSA. This is accomplished by measuring the Q-switched fiber laser performance with the theories presented in chapter 2 to describe and explain the expected and the unexpected behaviours of the generated Q-switched pulse.

In Chapter 5, fabrication of GOSA based on optical deposition method is presented taking the advantage of GO hydrophilic behaviour to facilitate and reduce the cost of fabrication. Here, the optical deposition method based on thermophoresis and heat convection effects with GO dispersed in water will be discussed in detail. Moreover, Raman spectrum is used for the SA characterisation and comparison is made with the SA in chapter 3 in terms of density of defects and saturable absorption. Finally, an experiment with the fabricated GO on generating fiber laser in the 2 μm region will be demonstrated with a 2m long Thulium doped fiber is used as gain medium. Similar to chapter 3, the Q-switched laser performance will be analysed in detail.

In Chapter 6, a Q-switched dual-wavelength fiber laser will be demonstrated using commercialised GO paper. Here, the structure of GO paper will be compared with the GO film for evaluation. The dual-wavelength fiber laser is consists of photonic crystal fiber, polarization controller and tunable-band pass filter which act as the main components responsible for the generation of the dual-wavelength laser.

Finally, Chapter 7 concludes the contributions of present work and the directions of future work.

CHAPTER 2: THEORETICAL REVIEW ON PASSIVELY Q-SWITCHED FIBER LASER OPERATION AND SATURABLE ABSORBER PRINCIPLE

2.1 Introduction

The theory behind Q-switched pulse generation was first presented by Wagner and Lengyel (1963) based on ruby laser and followed by Saleh et al. (1991) and Davis et al. (2014). However, the presented differential rate equations by the respective researchers are suited for the Q-switched laser operation in an ideal instantaneous q-switch regime, with linear configuration setup and having non-continuous pump scheme.

In this research work, where graphene oxide (GO) material will be used as saturable absorber, more parameters needs to be considered to accurately model the more non-linear laser system which is based on using ring configuration setup with continuous pump scheme via laser diode. This allows us to characterise the Q-switched laser using GO material more accurately and to explain the expected and unexpected experimental results obtained which will be presented in later chapters.

Moreover, in this chapter, the principles related to Q-switched laser operation with a saturable absorber (SA) will be reviewed from the recent work made by several researchers and the necessary modification will be made to meet the laser specifications mentioned. The principles include the differential rate equations and Q-switched threshold condition that describe the Q-switched laser operation. In addition, the important saturable absorption parameters and relationships will also be reviewed and analysed which form the building block for the q-switching process.

2.2 Q-switching in fiber laser with saturable absorber

In passive q-switching, a modulator requires no external power, providing the advantages in terms of cost, compactness and design complexity as compared to active q-switching. There are many ways of approaching passively q-switching. Such example is using a SA, namely the Semiconductor Saturable Absorption Mirrors (SESAMs) (Hakulinen and Okhotnikov, 2007). The operation of the SA is based on the non-linear saturable absorption principle which is at high optical intensity, the transmission is larger than at low optical intensities.

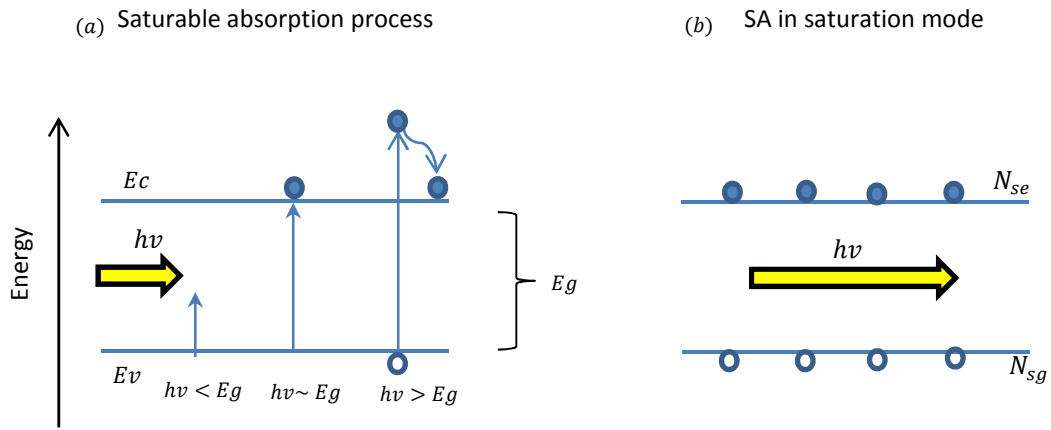


Figure 2.1: Two- level system showing optically generated electron-hole pair formation in a saturable absorber with a) saturable absorption process and b) SA in saturation mode.

The saturable absorption process can be described at a microscopic scale as shown in figure 2.1. At high optical intensity and with the right photon energy ($h\nu \geq E_g$, the band gap energy of the SA), saturable absorption will occur and electron-hole pair will be produced as shown in figure 2.1 a). The excess photon energy ($h\nu > E_g$) may give the electron kinetic energy which will dissipate as heat, resulting the electron relaxes at a more stable excited state. The large absorption of radiation due to high

optical intensity will cause large changes in the absorption rates of the SA. Based from Pauli Exclusion Principle, when the excited state is fully occupied, the net absorption becomes very small and the material is said to be saturated. Then the subsequent light could no longer be absorbed leaving the SA momentarily transparent for light transmission as shown in figure 2.1 b). Once the subsequent light passed through the SA, excited state absorption effect and electron-hole recombination can occur which reduces the transmitted light intensity and recovers the saturable absorption respectively.

2.3 Differential rate equations

For more accurate description of the highly non-linear Q-switched operation, the following differential rate equations and the supporting equations which have been modified slightly based on the ones presented by Savastru et al. (2013) and Savastru et al. (2012) are used. It is also noted that, the equations are valid for quasi-three level active medium (with inversion reduction factor, $\gamma = 1$ for Er^{3+} doped fiber), considering a ring resonator configuration (unidirectional light propagation), continuous pumping condition, including both the upper and ground states absorption of the SA and excluding the carrier interaction.

$$\frac{d\varphi}{dt} = \frac{\varphi}{\tau_{rt}} \{ \sigma_g N_g l_g - \sigma_{sg} N_{sg} l_s - \sigma_{se} N_{se} l_s - \alpha_{rt} \} + S \quad (2.3.1)$$

$$\frac{dN_g}{dt} = -c\sigma_g l_g N_g \varphi - \frac{N_g}{\tau_g} + R_p \quad (2.3.2)$$

$$\frac{dN_{sg}}{dt} = -\gamma_s c \sigma_{sg} l_s N_{sg} \varphi + \frac{N_{se}}{\tau_{se}} \quad (2.3.3)$$

$$\tau_{rt} = \frac{l_r}{c} \quad (2.3.4)$$

$$R_p \approx \frac{P_p}{h\nu A_g l_g} \quad (2.3.5)$$

The list of parameters and their definitions for equations (2.3.1-2.3.5) are summarized as follows:

φ : photon density,

S: spontaneous emission,

N_g : population inversion density of the gain medium,

N_{sg} : the population density of SA at the ground absorbing state,

N_{se} : the population density of SA at the excited absorbing state,

A_g : area of the fiber core

l_g : the length of the gain medium,

l_s : the length or thickness of the SA,

l_r : the resonator length,

c : the speed of light,

R_p : the pumping rate density of active medium,

α_{rt} : is the nonsaturable intracavity round-trip dissipative optical loss,

γ_s : inversion reduction factor of the SA,

σ_g : the stimulated emission cross sectional area of the gain medium,

σ_{sg} : the ground state absorption cross-section of the SA,

σ_{se} : the excited-state absorption cross-section in SA,

τ_{rt} : the round trip transit time in the laser resonator;

τ_g : the excited-state relaxation time for the gain medium,

τ_{se} : the excited state life time of the SA,

P_p : pumping power,

$h\nu$: energy of laser photon.

Both equations (2.3.1) and (2.3.2) describe how the increase rate of photon density and the decrease rate of population inversion behave respectively. Equation (2.3.1), the product of population density at ground state, N_{sg} with its ground absorbing cross section, σ_{sg} and the population density at the excited state, N_{se} with its excited state cross section, σ_{se} of the SA are included to model the non-linear passively q-switching operation. They have a decrement effect on the photon density increase rate while the spontaneous emission, S can contribute to the increase rate of photon density.

Equation (2.3.2) specifically introduces parameters related to the gain medium (specifically the quasi-three level fiber gain medium) and includes the pumping rate density, R_p which in turn proportionally relates to the pumping power, P_p as defined in equation (2.3.5) by considering continuous pump scheme. The equation states that the decrease rate of the population inversion increases as the population inversion density is increased with having the pumping rate of gain medium have an opposite impact to the decrease rate.

In equation (2.3.3), the behaviour of the decrease rate of absorption at the ground state of the SA is described, where the decrease rate is fast when the population density at the ground state of the SA, N_{sg} is large, the incident light intensity is high and the population density of the SA at the excited state, N_{se} is small.

2.4 Q-switched threshold condition

Based on the differential rate equations presented previously, the passively Q-switched threshold expression with a saturable absorber (SA) can be derived. The expression can be developed at a transition time; that is from the laser system of having high loss, $t=0$, to having net increment of photon density, $t>0$. At $t=0$, the net increment experienced by a photon in the laser resonator is zero, where rate equation (2.3.1) = 0, and subsequently must be increasing, where the derivative of rate equation (2.3.1) > 0 at $t>0$. This leads to the passively Q-switched threshold condition (Gupta & Ballato, 2006),

$$\alpha_r = \frac{\sigma_{sg} l_s}{\sigma_g l_g} > \frac{N_s \sigma_{sg} + (\alpha_{rt}/l_s)}{N_s (\sigma_{sg} - \sigma_{se})} \quad (2.4.1)$$

where N_s is the total population density of the SA which includes the population at the ground and excited states and α_{rt} is the resonator round-trip loss. The left hand side of the expression dictates that the absorption cross-section state of the SA, σ_{sg} must be greater than the stimulated emission cross-section area of the gain medium, σ_g to enable q-switching. Meanwhile, the right hand side of the expression describes the ratio of the total round-trip loss to the saturable round trip loss at $t = 0$. In a system where the loss is dominated by SA ($\alpha_{rt,t}/\alpha_{rt,s} \approx 1$), expression (2.4.1) simplifies and states that the loss of the SA saturates more quickly than the gain of the gain medium and q-switching can be initiated. In contrast, laser will tend to oscillate in CW regime when the expression (2.4.1) is unsatisfied.

Furthermore, the excited-state lifetime, τ_{se} of the SA has to be long enough, to enable the right amount of depletion of the ground-state population density upon illumination for q-switching operation, where the dynamics of this depletion has been described in the rate equation (2.3.3). In addition, the excited state absorption (ESA) cross section, σ_{se} must be considerably smaller than that of the ground-state, σ_{sg} to prevent the ESA effect and to enhance the saturable absorption of the ground state. The ESA effect can occur typically when the SA saturates (when the excited state becomes significantly populated via one-photon absorption) which lead to the possibility of these excited electrons being further photo-excited to another higher excited state. This effect will cause parasitic absorption at the high-intensity side of the Q-switched pulse transmission and form a source of loss in the laser resonator. Therefore, it is desirable to use a material of minimum σ_{se}/σ_{sg} ratio for good passively Q-switched laser performance (Burshtein et al., 1998).

2.5 Pulse-build up process

The first pulse-build up process with the SA and a quasi-three level active medium and by considering continuous pumping condition can be illustrated in figure 2.2. It is noted that, the loss curve represent the saturable absorption of the SA and the nonsaturable loss from the resonator and the SA, while the gain curve represent the population inversion dynamics and the pulse curve represent the photon density dynamics. Both the SA and the gain medium are used to modulate the Q-value in the laser resonator and by the continuous pump scheme via laser diode pumping, the resonator will repeatedly Q-switched producing a train of pulses. The SA create loss (by absorbing light) thus delaying laser generation due to the suppression of stimulated emission in the gain medium. This allows the population inversion or gain to be raised at a high amount. When the laser gain has reached the initial

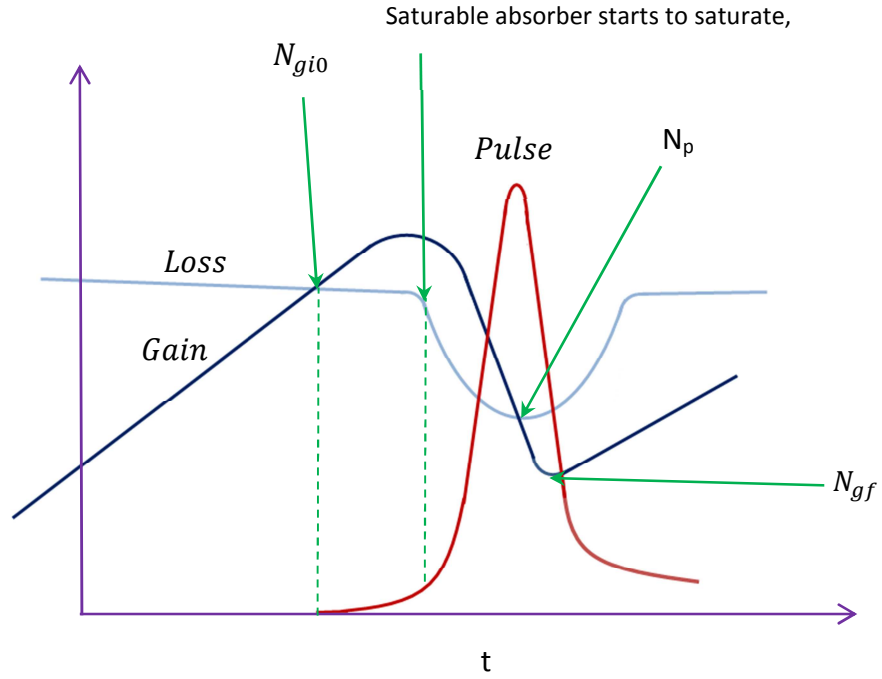


Figure 2.2: The first pulse build-up process for Q-switched laser with saturable absorber

population density inversion value, N_{gio} , that is where the gain exceeds the total resonator loss, the photon density or pulse will then start to build up from amplified spontaneous emission (ASE) noise (Kashiwagi & Yamashita, 2010). The N_{gio} can be described by the following equation with some modification is made by Savastru et al. (2012) and Gupta and Ballato (2006), to meet the laser system specifications as mentioned previously,

$$N_{gio} = \frac{N_s \sigma_{sg} l_s + \alpha_{rt}}{\sigma_g l_g} \quad (2.5.1)$$

Equation (2.5.1) is derived by assuming the pulse build-up time is generally quite short compared with the pumping and relaxation times of the gain medium. Moreover, it is derived by setting the left -hand side of the rate equation (2.3.1) to zero and assume that the population of the ground state of SA is equal to the total population density of the SA, $N_{sg} = N_s$. And after time, the photon density will become large enough that it begins to saturate the SA and in subsequent, the total resonator loss will be reduced dramatically and high intensity of light will be transmitted. Due to the pulse generation, the gain will start to reduce and a pulse peak is formed after it has reached the N_p value (Dong, 2003),

$$N_p = \frac{N_s l_s \sigma_{se} + \alpha_{rt}}{\sigma_g l_g} \quad (2.5.2)$$

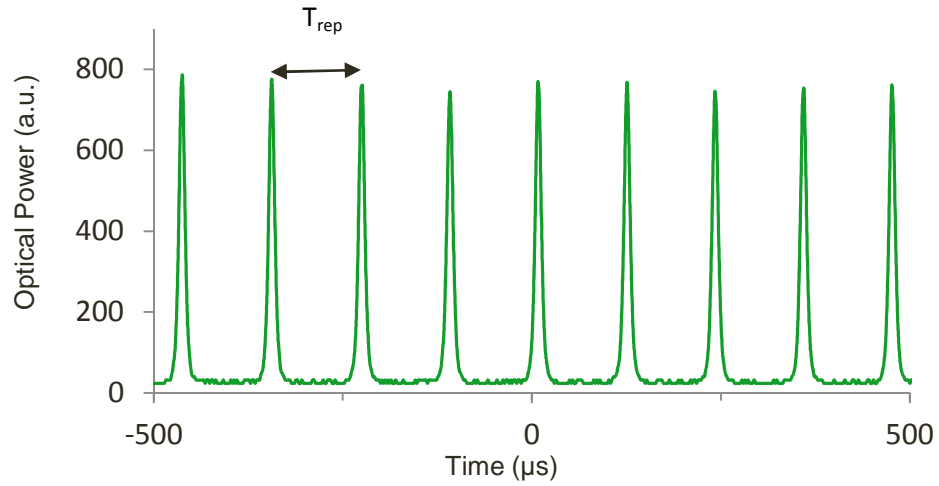


Figure 2.3: Pulse trains produced in a fiber laser with saturable absorber

Equation (2.5.2) is derived by setting the left hand side of the rate equation (2.3.1) equal to zero and assuming at this time that the population density at the ground state is almost equal to zero, $N_{sg} \cong 0$.

Once the Q-switched laser begins to oscillate in the resonator, the population density at the ground state of SA and population inversion of the gain medium begin to change rapidly, where a train of pulses can be generated as shown in figure 2.3. It is noted that, for the second and subsequent pulses, the initial population inversion will be different by considering the residual population inversion density, N_{gf} (Savastru et al., 2012, Dong, 2003),

$$N_{gi} = N_{cw} - (N_{cw} - N_{gf}) \exp(-T_{rep}/\tau_g) \quad (2.5.3)$$

$$N_{cw} = R_p \tau_g \quad (2.5.4)$$

where T_{rep} is the time interval between laser pulses and N_{cw} is the population inversion of the gain medium by continuous pumping.

2.6 Saturable absorption parameters

The most important properties of a SA for passively q-switching are the saturable absorption, nonsaturable absorption, saturation intensity, absorber recovery time and absorption bandwidth. These properties are governed by the chemical composition and atomic arrangement of the SA material and as well as the structure of the SA device. Moreover, the properties can be combined and described in a simple two-level non-linear saturable absorption coefficient as shown in equation (2.6.1). It is noted that, due to normalisation, the saturable absorption is equivalent to modulation depth and nonsaturable absorption is now expressed as a percentage of linear absorption (Bao et al., 2011),

$$\alpha(I) = \frac{\alpha_0}{1 + \frac{I}{I_s}} + \alpha_{ns} \quad (2.6.1)$$

Where α_0 is the modulation depth, I is the incident light intensity, I_s is the saturation intensity, and α_{ns} is the nonsaturable absorption.

On the other hand, the saturable absorption can be expressed as,

$$\alpha_s = \sigma_{sg} N \quad (2.6.2)$$

The σ_{sg} and N are the absorption ground cross section and concentration of the material respectively. The saturable absorption dictates the relative number of photons absorbed per unit distance from the SA material. If the saturable absorption coefficient is large, the photons are absorbed over a relatively short distance rather than deeper into the SA.

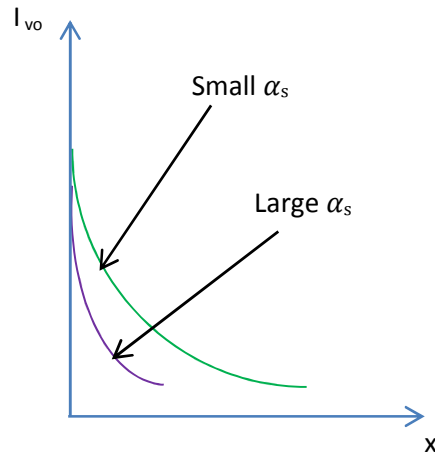


Figure 2.4: Photon intensity, I_{vo} versus distance, x for two different absorption coefficients.

This matter can be further illustrated by figure 2.4 where it shows the photon intensity, I_{v0} as a function of distance, x for two general values of absorption coefficient. The figure shows that if the absorption coefficient is large, the photons are absorbed over relatively short distance with the photon intensity decreases exponentially with distance through the SA.

On the other hand, the nonsaturable absorption is the loss that cannot be saturated by the SA due to scattering loss, transmission loss, nonsaturable defect absorption, free carrier absorption, Auger recombination, and many more. The cause of the scattering loss might be due to the material surface roughness, rough interfaces, and lattice defect. Moreover, the minimum Q-switched pulse width that can be generated depends on the modulation depth of the SA that governs by both from the saturable absorption and nonsaturable loss properties.

Furthermore, the saturation intensity from equation (2.6.1) can be defined as the intensity required in a steady state to reduce the absorption into half of its unsaturated value,

$$I_s = \frac{hf}{\sigma_{sg}\tau_{se}} \quad (2.6.3)$$

where h is plank constant, f is the light frequency operation, σ_{sg} is the absorption cross section at the ground state of the SA, and τ_{se} is the excited state life time or the absorber recovery time. Equation (2.6.3) suggests that the longer excited state life time before recombination, the less continuous wave intensity is required to saturate the SA.

In order to demonstrate the absorption dynamics of the SA, figure 2.5 shows a plot of the normalized non-linear absorption at different normalized light intensity as described in equation (2.6.1). From the figure, when light intensity produced in the laser resonator is less than the saturation intensity ($I < I_s$) of the SA, the optical absorption is high and lasing is prevented. When the light intensity, $I \geq I_s$, the absorption decreases and transmissivity gradually becomes greater. Finally, when $I \gg I_s$ the absorption is saturated thus, the resonator is in high Q-value and Q-switched laser oscillation commence. However, the nonlinear saturable absorption could not reach 0% as shown is due to the nonsaturable loss property, α_{ns} of the SA.

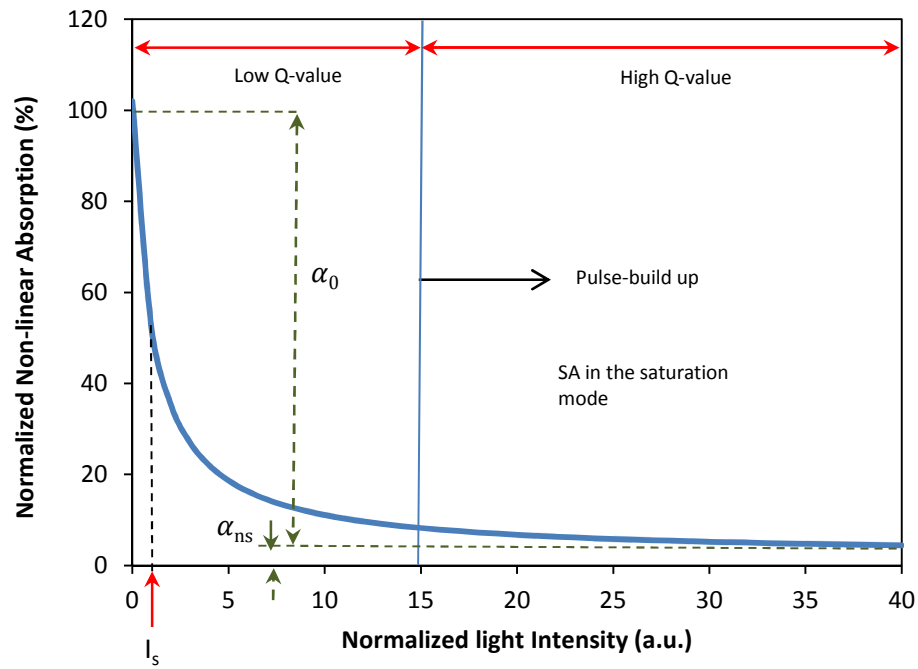


Figure 2.5: The non-linear saturable absorption dynamics as a function of light intensity in Q-switching.

2.7 Summary

In this chapter, we have reviewed and modified the differential rate equations and pulse build-up equations to suit the need the interest of laser system specifications which will be presented in later chapter. Moreover, the non-linear of saturable absorption principle at the microscopic scale based on the two-level energy diagram have also been reviewed. In addition, the important properties of SA such as the non-linear absorption coefficient, nonsaturable absorption, saturation intensity and with the relationship of light absorption in respect to the thickness of the SA having different absorption coefficients have been reviewed and analysed.

CHAPTER 3: FABRICATION AND CHARACTERISATION OF GRAPHENE OXIDE FILM AS SATURABLE ABSORBER

3.1 Introduction

Graphene oxide (GO) has a unique characteristic due to its polar surface properties (Haubner et al., 2010) that makes it different than the well-known sp^2 carbon allotropes such as graphene (Wang et al., 2012, Sun et al., 2010) and carbon nanotube (CNT) (Ahmad et al., 2013, Harun et al., 2012). This raises the interest to build a saturable absorber (SA) device from this material. In this chapter, the fabrication process to build a GOSA in a film form will be demonstrated. Initially, pure GO will be produced via chemical oxidation from pure graphite flakes using simplified Hummer's method (Huang et al., 2011) which provide faster reactant mixing time and the fabrication process required without any cooling treatment.

The produced GO in a colloid form will be characterised using UV-visible spectroscopy technique. Then, a GO film will be yield on a 90 mm petri dish via drop-casting method for the ready of integration with an optical fiber. Raman spectroscopy technique will be used to characterise the solid-state GO in terms of disordered (amorphous) and ordered (crystalline) structures. Moreover, an indepth analysis on the intensity ratio (I_D/I_G) from the Raman spectrum will be discussed using a model modified from Ferrari and Robertson (2000) that relates to the retained crystal structure size of GO. This parameter is important because it relates to the saturable absorption coefficient of the GO which are useful in predicting the material limits and its performance to generate Q-switched laser.

3.2 Graphene Oxide molecular bonding and electronic band structures

This section will begin by reviewing on the molecular bonding and electronic band structures of GO. This step is essential in order to be familiarised with chemical terms and principles that will be used extensively in the SA fabrication and characterisation sections. Moreover, this section also provides the information related to the optical response, chemical, and electronic band structure of GO. Nevertheless, graphite and graphene molecular bonding structures will be reviewed first as a platform in order to understand the more sophisticated GO molecular structure.

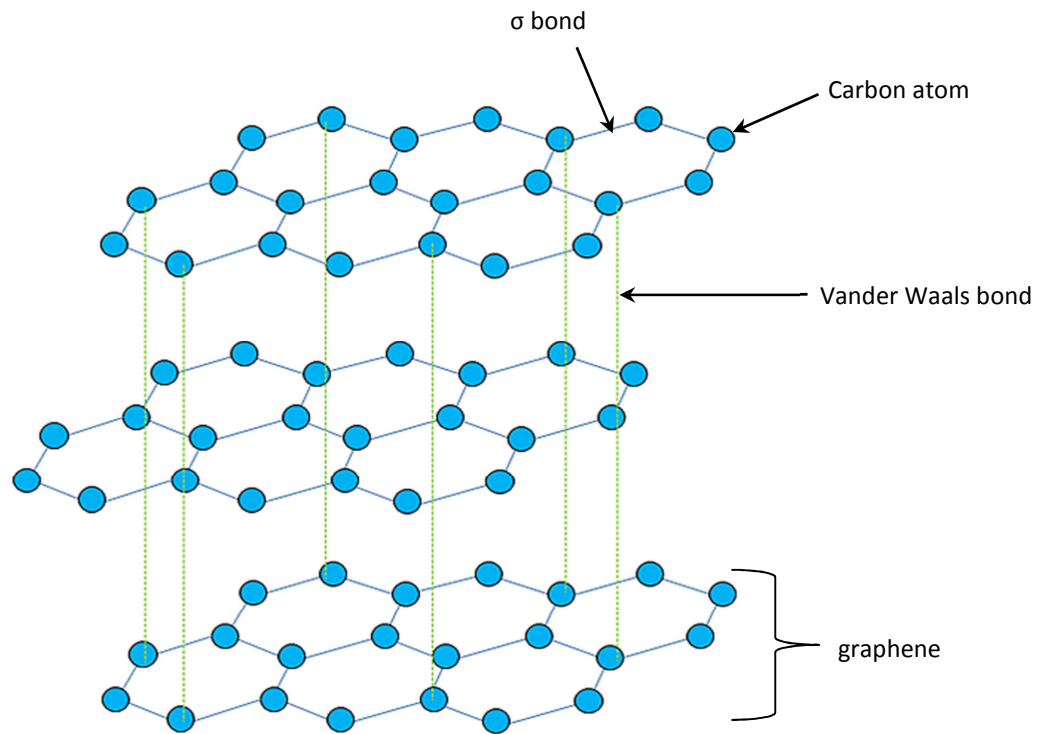
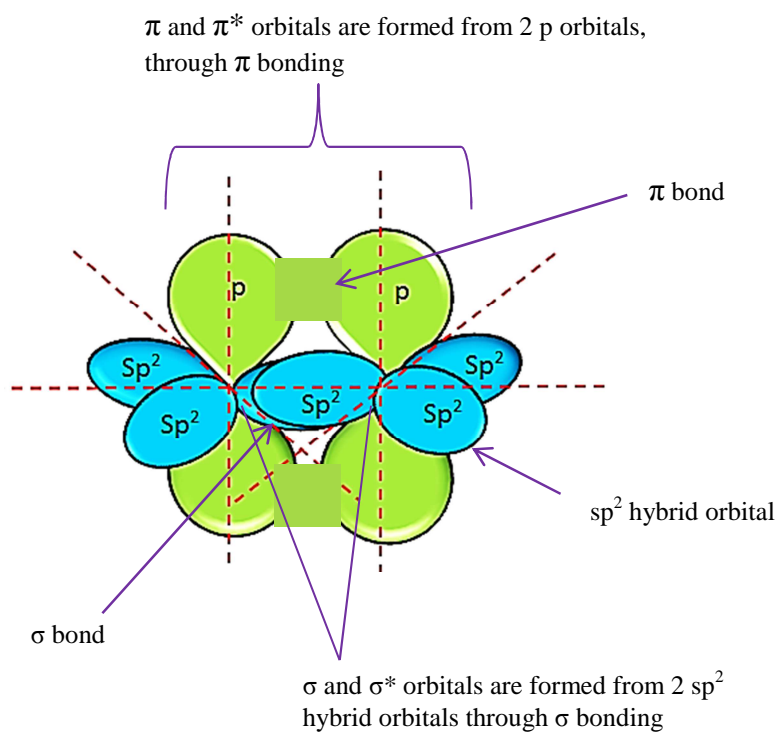
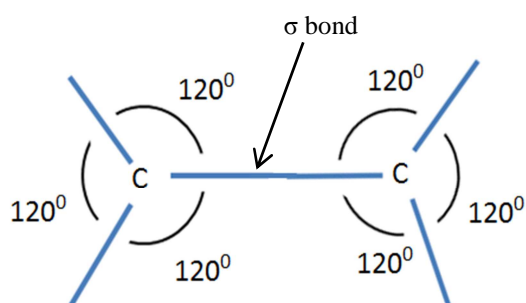


Figure 3.1: 3-dimensional view of Crystalline Graphite's molecular structure



(a) 3-dimensional view



(b) Geometrical top view on a plane

Figure 3.2: sp^2 carbon molecular bonding and geometry structures in a graphene sheet
(a) 3-dimensional view (b) geometrical top view

The crystalline graphite molecular structure that composes many layers of graphene sheet stacking on top of each other is shown in Figure 3.1. A single sheet of graphene, has a planar structure with an array of carbon atoms that are covalently bonded and arranged in a honeycomb lattice (Avouris, 2010). The aromatic ring of graphene exhibits strong single σ bond and double bonds (σ and π bonds) between the carbon atoms arranged in an alternatively manner that consists of 6 carbon atoms to form a ring-like hexagon shape. This ring are repeated and bonded in array to form that honeycomb lattice. On the other hand, the weak Van der Walls bond in between the sheets gives graphite the lubricant property; which explains that graphene flakes can be extracted easily using the scotch tape method (Chang et al., 2010). However that method suffers in controlling the thickness layer of graphene and the process is poor in repeatability.

In graphene, the carbon atoms are sp^2 hybridized and covalently bonded to form strong bonds as shown in Figure 3.2. The lobe-like structure of the orbitals in the figure is due to the electrons behaved like waves. In the double bonding region between two carbon atoms, one σ bond is formed contributed from two sp^2 hybrid orbitals and creates σ and σ^* orbitals. The σ bonds in graphene are arranged in trigonal manner having equal angles of 120° at a plane as shown in the figure. In addition, a π bond is formed from two p orbitals that are normal from the plane to form the secondary bonding. Through this molecular bonding system, a planar of sp^2 aromatic ring cluster is built to form the graphene sheet. Owing to this bonding structure, graphene has been proven to exhibit a breaking strength of two hundred times stronger than steel (Lee et al., 2008) and a linear optical absorption of 2.3% across all low-photon energies of light at low intensity (Stauber et al., 2008).

In comparison, a single sheet of graphene oxide (GO) contains a mixture of non-oxidized carbon bonds (sp^2 bonds) and oxidized carbon bonds (sp^3 bonds) (Shang et al., 2012) with water molecules are bonded in between the GO layer. The most favourable and often use model to describe the GO molecular structure is based on the Lerf–Klinowski model (He et al., 1998, Lerf et al., 1998) as shown in Figure 3.3. The figure clearly shown that the GO has more complex and disordered structure as compared to the single crystalline structure of graphene. The atomic force microscope studies suggest that a sheet of GO has a thickness of about 1 nm, which is considerably larger than that of ideal graphene due to the presence of oxygen-containing functional groups and adsorbed water above and below the carbon basal plane (Paredes et al., 2009, Jung et al., 2008, Akhavan, 2010). The basal planes of GO are contained with epoxide and hydroxyl groups, while carboxyl and carbonyl groups are located at the edges. These oxygen functional groups make GO highly hydrophilic, but degrade the aromaticity of the graphene framework (Zhou et al., 2010). The disruption of aromatic regions in the GO basal plane, makes the GO consists of both sp^2 aromatic regions and oxidized aliphatic six-membered rings that exhibit sp^3 hybridized geometry. At the sp^3 site, there exist only σ bond while the sp^2 site contain both the σ and π bonds. Due to the small size of the conjugated sp^2 site, the electronic band gap of GO tends to be larger than graphene and CNT; and in subsequently, GO behaves more of an insulator (Bykkam et al., 2013). The conjugation here is defined as the amount of series of alternating double bond and single bond that exists in the sp^2 aromatic ring and in the extended conjugation form found in the GO structure. Moreover, at the conjugation site, the π electrons are delocalized, enabling them to move freely throughout the carbon molecule structure that raises electrical conductivity of the material.

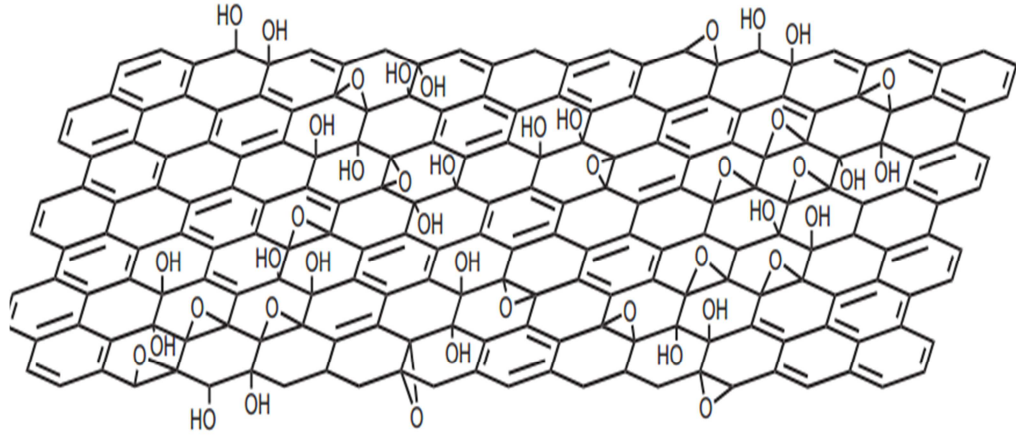


Figure 3.3: Lerf–Klinowski model for a Graphene Oxide's molecular bonding structure (He et al., 1998, Lerf et al., 1998)

Since electrical conductance is proportionally related to the optical absorption, thus one could also say that the GO has weaker optical absorption than graphene and CNT, where the relationship can be described as followed,

$$\alpha = \frac{4\pi\sigma}{nc} \quad (3.1)$$

Here, α is the absorption coefficient, σ is the electrical conductance, n is the refractive index, and c is the speed of light. Moreover, many literatures report that the band gaps of GO are varies from 0 to few eV (Yan et al., 2009, Yan et al., 2010), dependant on the ratio of carbon bonds to oxidation functional groups and their different arrangements. Fig. 3.4 shows the electronic band structure and density of states (DOS) for the GO based on the calculation done by Shang et al. (2012) and Shang et al. (2014). GO basically has two band-gap systems; highest occupied molecular orbital (HUMO) and lowest unoccupied molecular orbital (LUMO) and these HUMO and LUMO band-gaps are found to be ~ 0.6 eV, contributing to the sp^2 regions. On the other hand, the secondary band-gap structure is separated by H-1 and L+1 energy levels that are formed

by the sp^2 - sp^3 boundary sites where the defect or trap energy levels contributed by the oxygen functional groups are located above and below the HOMO and LUMO energy levels but within the secondary band-gap structure. Furthermore, report made by Pacilé et al. (2011) stated that the electronic structure of GO is largely insensitive to the number of layers, due to the layers are decoupled and filled with intercalated water molecules. The understanding on the molecular bonding and electronic band structure of GO is important in predicting the performance of this material for SA application in Q-switched laser. The preparation of the GOSA material will be discussed in the next section.

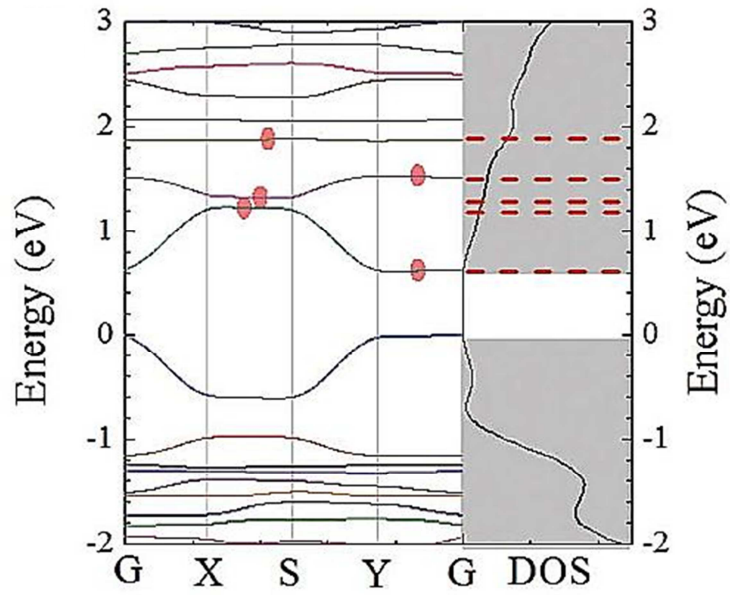


Figure 3.4: The electronic band structure (left panel) and density of states (DOS: right panel) of GO as calculated by Shang et al. (2012).

3.3 Producing graphene oxide aqueous suspension from graphite flakes via chemical oxidation

The fabrication of GOSA begins by producing graphene oxide colloid from graphite flakes using the simplified Hummer's method as described by Huang et al. (2011), which provides faster reactant mixing time. Moreover, the fabrication process can be performed without the need of any cooling treatment. Firstly, graphite flakes is oxidised by mixing the flakes with $\text{H}_2\text{SO}_4\text{:H}_3\text{PO}_4$ (320:80 mL) and 18 g KMnO_4 as oxidizing agent in a beaker with the aid of magnetic mixer device for proper stirring. The compound is stirred at room temperature for 3 days to allow the oxidation of graphite. Hydrogen peroxide solution is subsequently added to stop the oxidation process, forming the desired graphite oxide. The graphite oxide is then washed with 1 mol hydrochloric acid and repeatedly with deionized water till a pH level of between 4 and 5 is obtained. It is noted that, the graphite oxide will experience exfoliation after the washing process, after which the graphite oxide colloid will become thick, producing graphene oxide (GO) gel-like colloid. The gel-like colloid is where the GO sheets are dispersed, randomly oriented and form a porous three-dimensional network with the cavities filled with water (Compton et al., 2012). It is noted that, GO is a non-stoichiometric compound, because the density of oxygen groups cannot be precisely controlled and its properties vary depending on its synthesis, processing, and environmental conditions.

Figure 3.5 shows the obtained GO colloid, which was dispersed in distilled water to achieve a concentration of 0.5 mg/mL. This colloid is then used for effective and accurate Ultraviolet-visible (UV-vis) spectrum measurement. The measurement is performed using Thermo Scientific Evolution 300 spectrophotometer and its main components are shown in Figure 3.6. The GO colloid is placed in a curvette to ensure minimum light reflection upon contact. Xenon lamp is used as light source where it is

monochromated prior contact with the sample for wavelengths selection. This measurement technique is used to confirm the presence of GO material in the sample. This can be identified owing to the GO molecules containing small amount of π -electrons due to having small size sp^2 aromatic clusters that will absorb the energy at UV wavelength and excite them to higher anti-bonding molecular orbital as shown in Figure 3.7.



Figure 3.5: Graphene oxide colloid with concentration of 0.5 mg/mL

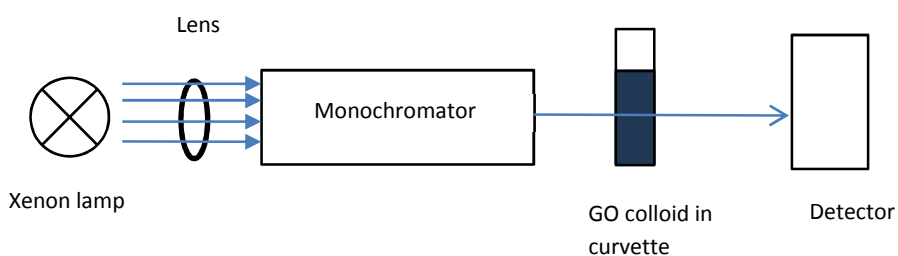


Figure 3.6: UV-visible spectroscopy components and setup

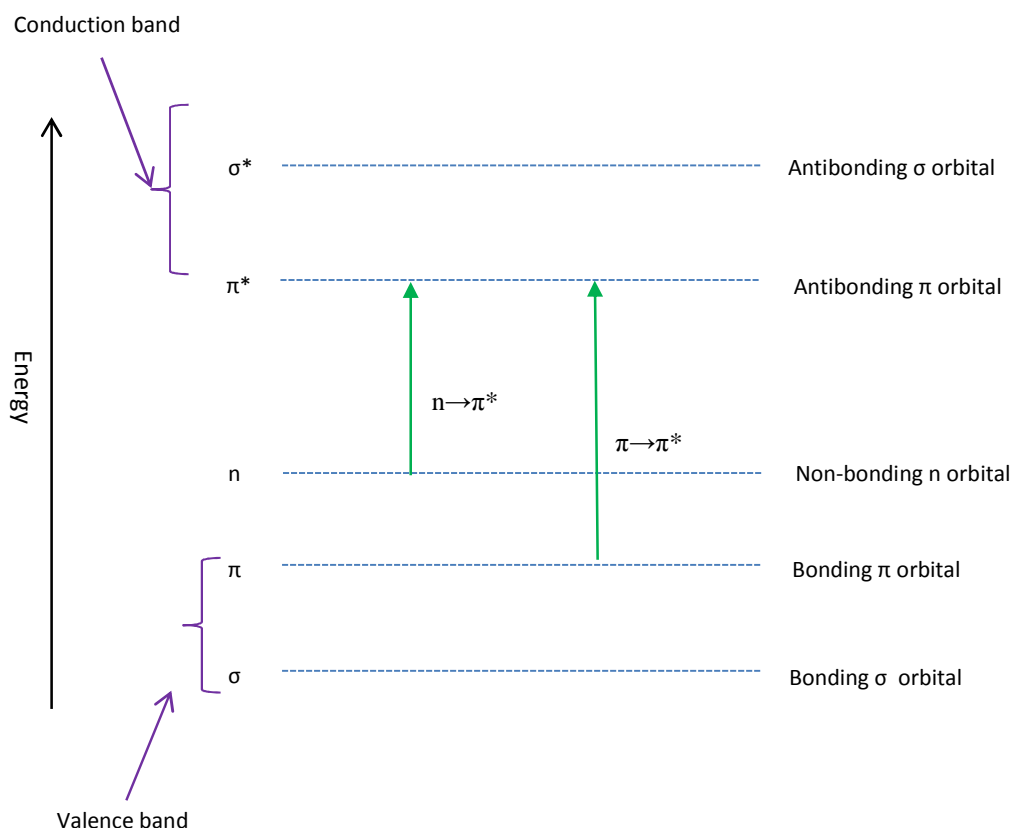


Figure 3.7: The $\pi \rightarrow \pi^*$ and $n \rightarrow \pi^*$ transitions based on UV-visible absorption

The UV-vis absorption spectrum of the GO at a steady state is shown in Figure 3.8 and plotted at wavelengths of 200–800 nm. At a UV wavelength of 228 nm, an absorption peak is observed, with an intensity of 2.29. The large absorption at that particular wavelength region is contributed by the $\pi \rightarrow \pi^*$ transition from the C=C bonds in the sp^2 aromatic cluster. The spectrum under 200 nm can be disregarded, due to inconsistency from baseline measurement, caused by deionized water. In addition, a small peak can be seen at around 300 nm, which is due to the $n \rightarrow \pi^*$ transition from the carbonyl groups in the sp^3 disordered region. This result agrees well with that of graphene oxide as reported by Shang et al. (2012). Moreover, the size of the extended

conjugation can be determined by the peak absorption wavelength from the spectrum (Marcano et al., 2010). Owing to the habitation of oxygen functional groups at the GO sheet the extended conjugated size is reduced, resulting the increased in band gap and the reduced of the peak absorption wavelength, typically at around 227-231 nm wavelength for GO material. A peak to shoulder absorbance intensity ratio with a value of 3.26 is obtained for this sample which is larger as compared to the ones reported by Marcano et al. (2010) with the ratio values of 3.14, 1.95 and 2.28 and from Mei et al. (2010) with the value of 2.17. This indicates that this GO sample has higher number of aromatic rings; with more rings provide larger absorption at that wavelength. Despite of having larger number of aromatic ring, the size of the extended conjugation is more or less the same; therefore the peak absorption wavelength does not differ by much.

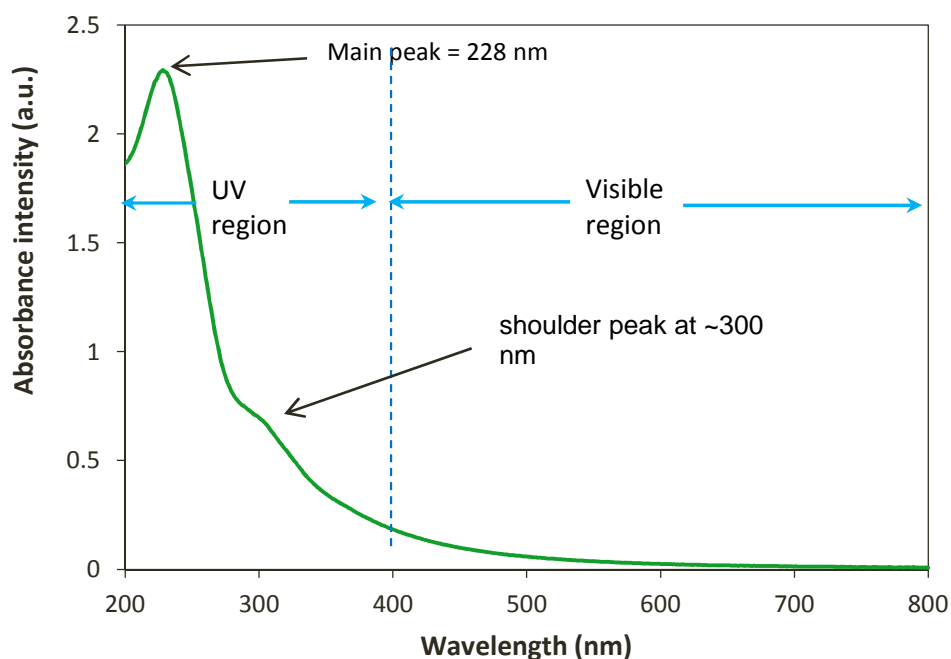


Figure 3.8: Absorbance spectrum of graphene oxide aqueous suspension across UV-visible wavelengths at a steady state.

It is noted that, by using the simplified Hummer's method proposed by Huang et al. (2011), GO with a larger sheet size is produced with higher degree of oxidation as compared to the other methods demonstrated by the researchers mentioned. In contrast, the previous observations made by Zhao et al. (2010) and Zhang et al. (2009) are different where the sheet size of GO is reduced with a higher degree of oxidation, which is caused by over oxidized graphite under elevated temperature and smaller size of graphite is used. Nevertheless, by using the simplified Hummer's method, the oxidation level can be increased and thus the sheet size and the number of aromatic rings can be increased as well. This is accomplished by controlling KMnO_4 : acid (H_2SO_4 : H_3PO_4) weight ratios, with higher ratio gives higher oxidation level.

3.4 Preparation of Graphene Oxide Film as Saturable Absorber via Drop-casting method

A film form of GO is fabricated in order to produce a solid-state SA for ease of integration with the optical fiber. Figure 3.9 shows a process flow in preparing GO film. It begins by pouring ten millilitre of the GO aqueous suspension (concentration of 0.5 mg/mL) onto a 90 mm Petri dish using Graduated Cylinder. The poured GO colloid is allowed to dry for 1 day and subsequently, a dried thin film is yield due to the loss of water molecules by the evaporation process. Since, the GO flakes tend to fold due to the resistance from collapsing into multilayers; some wrinkles are produced on the GO film surface after the drying process. In order to prepare the SA device, the film is carefully peeled off from the petri dish using a clean tweezer and a small piece from the peeled film is carefully cut using a sharp scissor. A small amount of index matching gel (IMG) is applied at the center-end-face (CEF) of a FC/PC fiber ferrule (SMF-28) and the piece of the film is carefully placed on top of the (IMG) covering the optical path as shown in Figure 3.10. A flat and clean object such as tweezer is used to carefully ensure that the whole surface of the film is flattened and stick at the CEF of the ferrule. It is noted that,

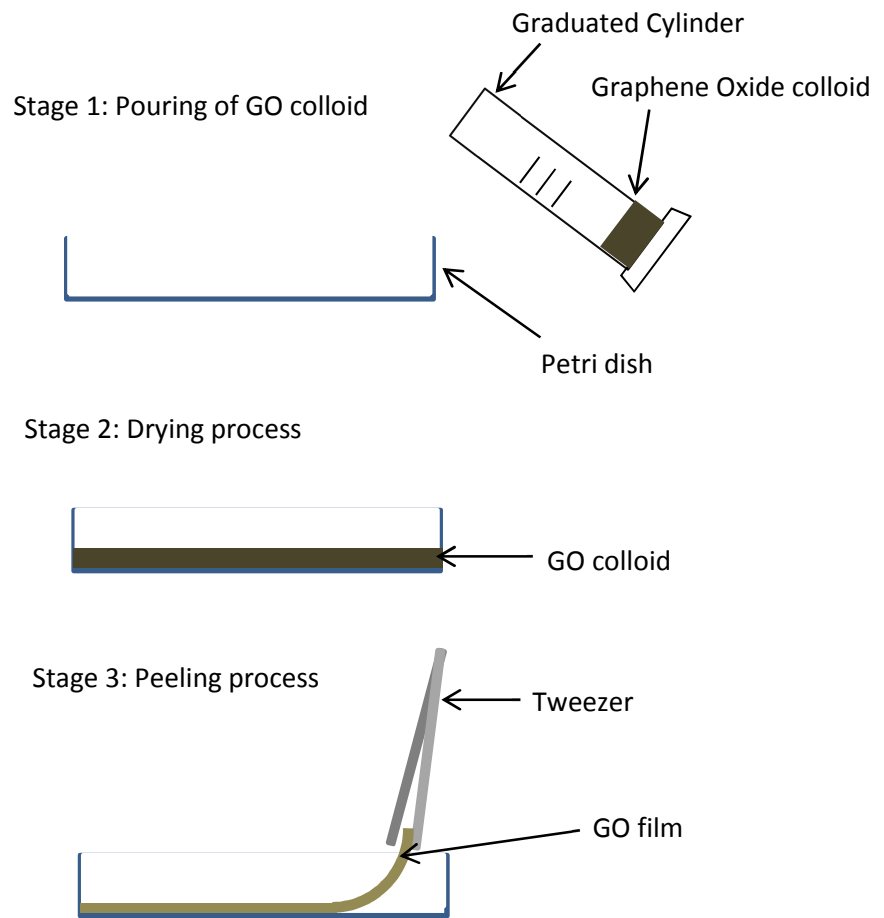


Figure 3.9: Process flow in preparing Graphene Oxide Film

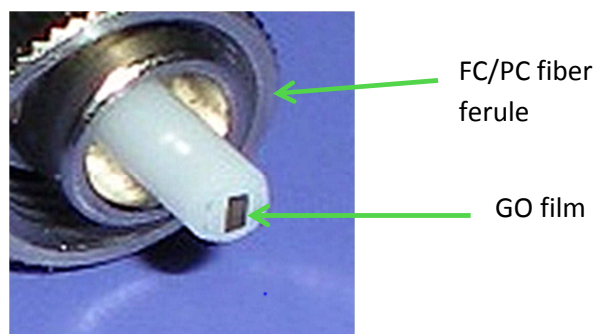


Figure 3.10: GO film on a FC/PC fiber ferule face

the IMG is used as an adhesive element to minimize displacement and to optimize the coupling of light from the optical fiber path to the film.

It is worth to mention that the solid film form of the GOSA has a practical benefit as compared to our previous work using carbon nanotube (CNT) to generate Q-switched laser (Ahmad et al., 2013). In the work, a liquid form of single-walled CNT/PEO polymer is dropped on a facet of the fiber ferule to yield a dried solid form of the SA as shown in Figure 3.11. The SA however is fixed on the ferule thus impaired its flexibility to be used on different laser setups such as required to use different fiber types.

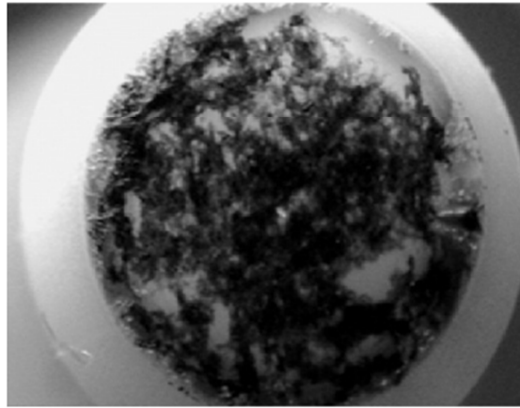


Figure 3.11: SWCNT/PEO composite deposited on fiber ferule facet.

3.5 Characterization of Graphene Oxide Film using Raman spectroscopy technique

In this section, we will analyse the GO film and the deposited CNT on the fiber ferule using Raman spectroscopy technique in terms of their crystalline structures and make the necessary comparison. Specifically, the Raman analysis will be focused on GOSA film where its retained crystalline size, density of defect, and saturable absorption can be estimated. This information is possible to obtain due to the specific

phonon modes and with the specific Raman scattering processes that contribute to each feature. In addition, the theories related to the Raman scattering also will be covered in this section which are crucial in order to analyse the complex Raman spectrum and characterise the GO film accurately.

In Raman Spectroscopy, a suitable laser wavelength, filter and detector technologies are used to measure the inelastically scattered lights which are produced at different photon frequencies when the laser hits the material under test. The inelastic scattering is also known as Raman scattering. A non-destructive technique and a simple sample preparation method of Raman spectroscopy allow it to be widely used for material identification, even for chemical species that are similar in identity. Raman scattered light is produced after a pump laser is radiated onto the material, where the light frequency is strongly depends on the vibrational modes in the molecules.

The effect of Raman scattering can be explained based on the quantum energy diagram as shown in Figure 3.12, where particle size is relatively small as compared to the wavelength of the incident light. When a pumped laser light with a photon energy ($h\nu_0$) hits a molecule, an electron in a ground state is excited to a higher energy level or at the virtual state as shown. It then relaxes and returns to the ground state while releasing the same amount of photon energy ($h\nu_0$) which is known as the Rayleigh scattered light or elastic scattered light which has higher probability to occur during the light and matter interaction than the inelastic scattered light.

In contrast, Raman scattering (inelastic scattered light) comprises of stokes and anti-stokes scatterings that behave differently as compared to Rayleigh scattering. In Stokes scattering, the electron begins in the ground state. It is excited to a virtual state by absorbing the laser pump energy, after which the excited electron is scattered by emitting phonons where the phonon modes emitted depends highly on the molecular

structure of the material. Due to the optical-phonon mode dependant, the electron relaxes to a ground state which is higher than the electron's original starting state, by releasing photon at lower energy ($h\nu_0 - h\nu_{m0} \dots h\nu_{mn}$ where $\nu_{m0} \gg \nu_{mn}$) than the pump energy. The lower energy light is called the Stokes scattering, where the loss of

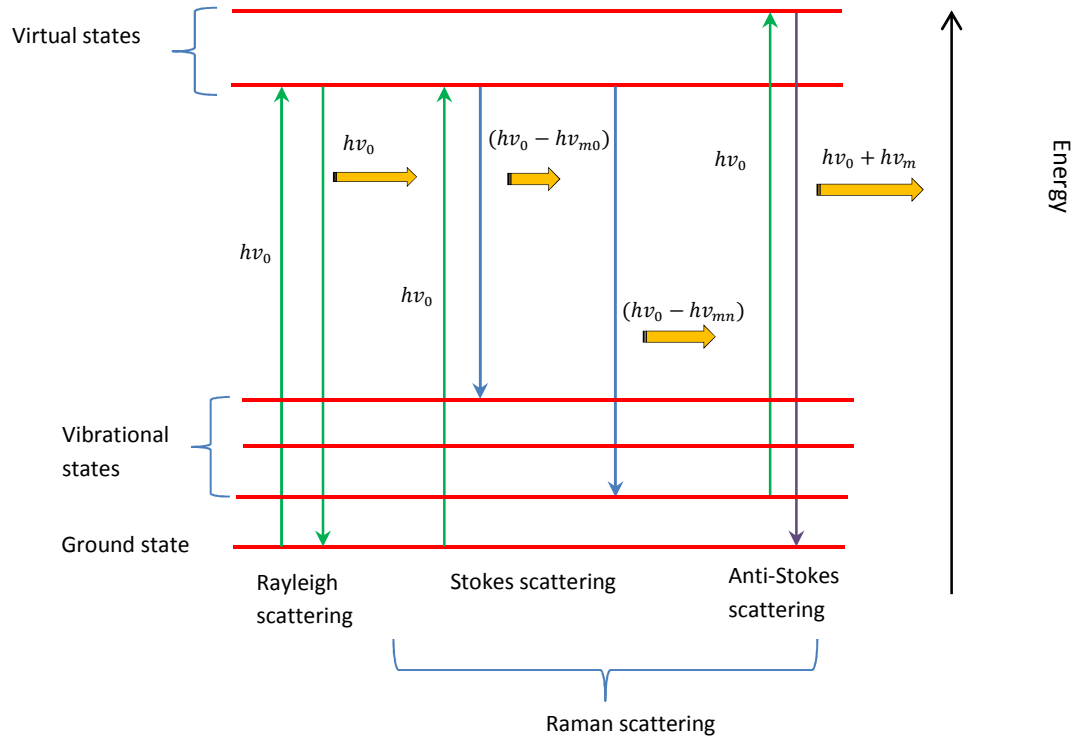


Figure 3.12: Energy diagram showing light scattering effect when light interact with molecule

energy is due to the energy transfer to the phonon mode. Most of the electrons are in ground state at room temperature, therefore Stokes is commonly observed in Raman spectrum than anti-Stokes scattering, where an electron begins at higher state due to certain condition before absorbing laser pump energy. It is noted however, Raman scattering is not only triggered by phonons, but any elementary excitation (such as a magnon, plasmon etc.) can be involved in a scattering process where the elementary excitation satisfies energy-momentum conservation. However, the characterisation of

GO will be involved only with the Raman and phonon scattering processes and the details of the process will be discussed later in this section. In order to characterise the GO film, a measurement setup based on Renishaw Raman Spectrometer is used as shown in Figure 3.13. From the figure, the fiber pigtail is perpendicular aligned in respect to the microscope lens at the translation stage so that the Raman scattered light

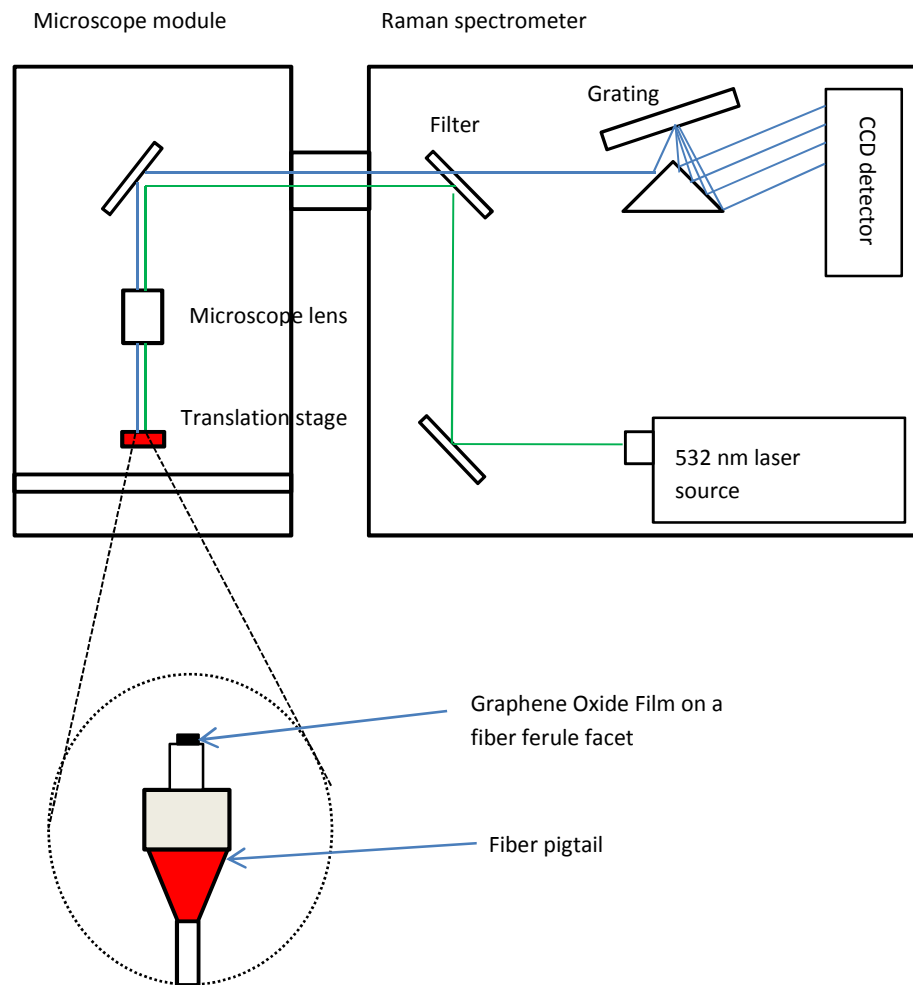


Figure 3.13: Renishaw Raman Spectrometer components and setup

(blue line) can be detected by the CCD (Charge-couple device) detector effectively when laser light (green light) hits the GO surface. A real-time microscope image of the GO surface is used as guidance in order to choose the location for laser contact. Raman

spectrum is generated when laser with wavelength of 532 nm (green light) at a power of 5 mW is radiated onto the GO film.

The laser radiation and Raman spectrum generation took place for about 10 seconds and the result obtained is shown in the Figure 3.14. The Rayleigh scattered light was also produced during the process. A filter is used to filter out the Rayleigh scattering component so that the Raman scattered signals can be clearly observed. In the Raman spectrum, the intensity of the scattered light (measured in CCD count with arbitrary unit, a.u.) is shown as a function of frequency downshift (losing energy) from the pump laser energy. More specifically, the horizontal-axis is measured as Raman shifts (cm^{-1}) or wave number and it is defined by,

$$R_{shift} = \left(\frac{1}{\lambda_0} - \frac{1}{\lambda_r} \right) \quad (3.2)$$

where λ_0 is the pump laser wavelength, and λ_r is the Raman scattered light wavelength.

All graphite-like materials that consist mainly of sp^2 carbon atoms such as CNT, graphene and graphene oxide will show the so-called D and G peaks, which lie at around 1350 cm^{-1} and $1580\text{--}1630 \text{ cm}^{-1}$ respectively (Ferrari & Robertson, 2000) . Fig. 3.15 shows the Raman spectrum of CNT saturable absorber, which was obtained and used in our previous work to generate Q-switched pulse (Ahmad et al., 2013). As shown in the figure, it has the G (1598 cm^{-1}), relatively small D (1352 cm^{-1}), D' or 2D (2684 cm^{-1}) peaks and very small two peaks at 186 cm^{-1} and 287 cm^{-1} which represent the Radial Breathing Modes (RBM) corresponding to the nanotube diameter. When we compare between GO and CNT Raman spectrum, it is observed that the GO has relatively higher D peaks than the CNT which dictates higher signature of defects in the crystalline structure of the sp^2 carbon lattice. It must be noted in advance, the entire

material analysis will be focus on the D and G peaks characteristic such as peak position and intensity ratio since those parameters have pronounce influence for GO characterisation, while a comparison study between the GO and CNT is not an accurate

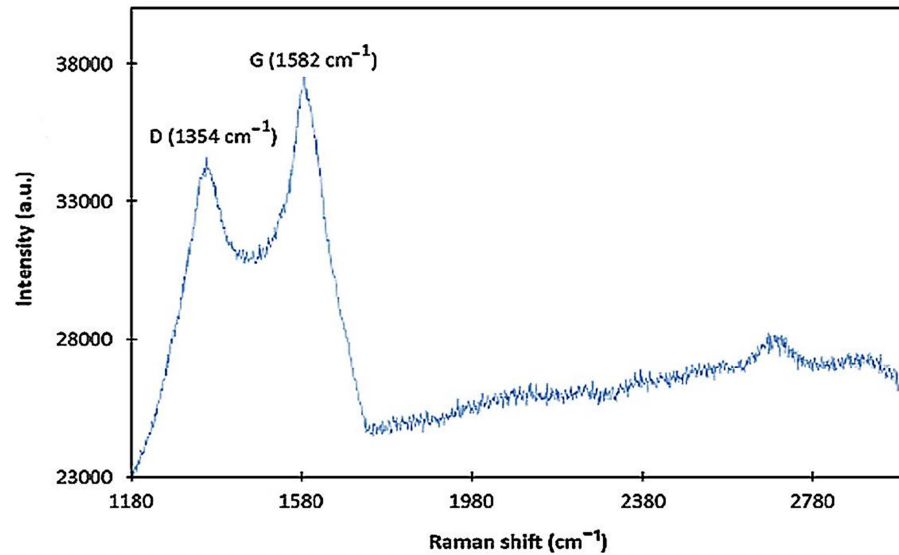


Figure 3.14: Raman spectrum of Graphene Oxide Film on a fiber ferrule.

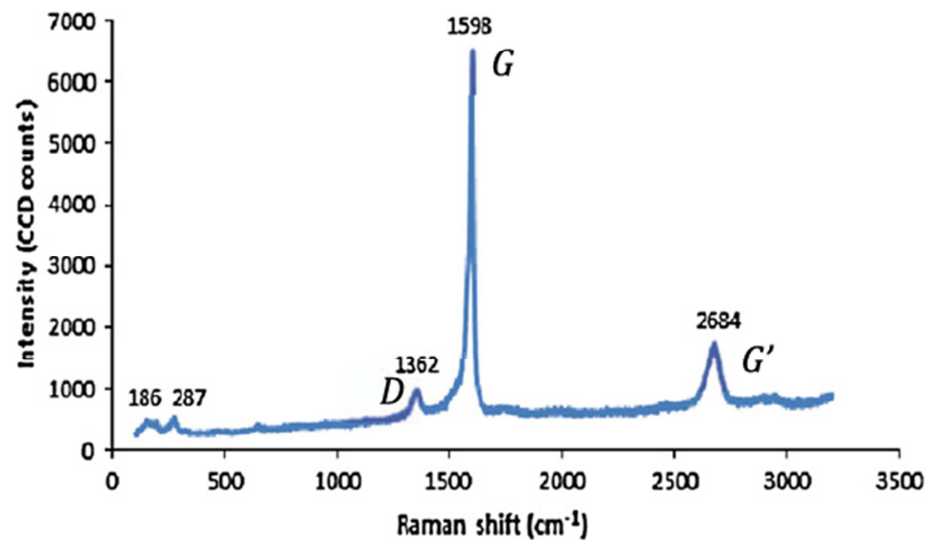


Figure 3.15: Raman spectrum of carbon nanotube on a fiber ferrule.

measurement especially if those parameters have close values. This due to different thickness of the material will alter the parameters mentioned and further discussion on this matter will be covered as we progress.

The D bands for both GO and CNT are produced from the Raman scattering by certain vibrational mode occurred in the sp^2 aromatic rings (Antunes et al., 2006, Ado et al., 2011). The vibrational mode mentioned is called the phonon A_{1g} breathing mode and it is activated only when defect is present which is caused by the microstructural disorder that breaks up the sp^2 aromatic rings structure. The D peak of GO obtained is located at 1354 cm^{-1} due to the vibrational mode arising from the alternating of sp^2 aromatic ring stretching, owing to the oxidation functional groups incorporated in the crystal lattice. In contrast, the D peak position for CNT is at higher frequency 1362 cm^{-1} , which could suggests that there exists more aromatic cluster in CNT.

It is noted that, the visible Raman spectrum (532 nm) depends fundamentally on the sp^2 sites and only indirectly on the fraction of sp^3 sites. Even though the D peak is a measurement of defect, such phonon A_{1g} breathing mode in GO sheet is occurred only at the sp^2 aromatic rings, where later we will discuss that the growth of the D intensity represent ordering instead of defect for high defect density material such as GO. Figure 3.16 shows the A_{1g} eigenvectors that dictates the alternating ring stretching behaviour in the lattice mentioned. The phonon and Raman scattering processes by the visible laser excitation for the D peak activation can be described through the inter-valley process as followed (Mohiuddin et al., 2009),

- 1) Laser-induced excitation of an electron/hole pair.
- 2) Electron-phonon scattering with an exchanged momentum $\vec{q} \sim K$ (A_{1g} breathing mode of phonon scattering).
- 3) Second elastic scattering by defect of the crystal lattice.

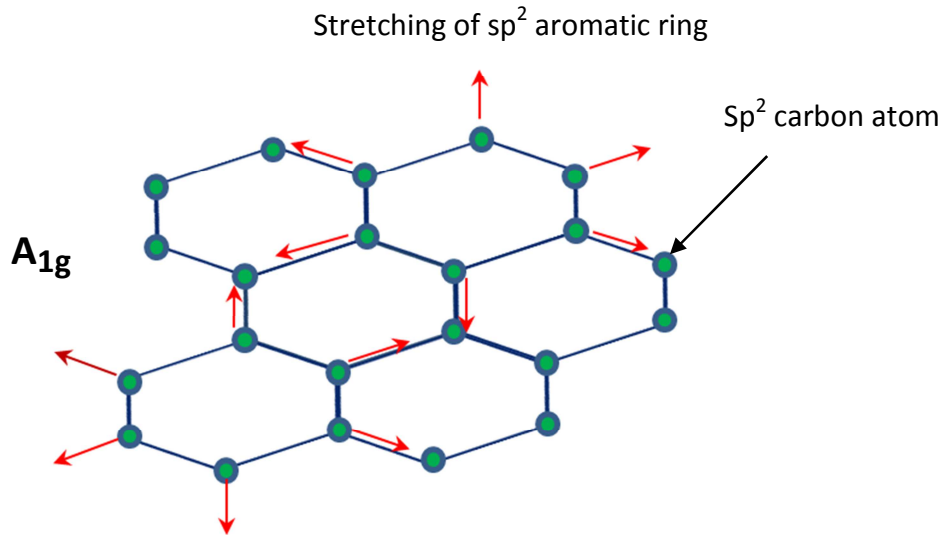


Figure 3.16: A_{1g} phonon eigenvectors (indicated by the red arrows) at the sp^2 aromatic ring cluster in GO sheet showing the alternating ring stretching behaviour.

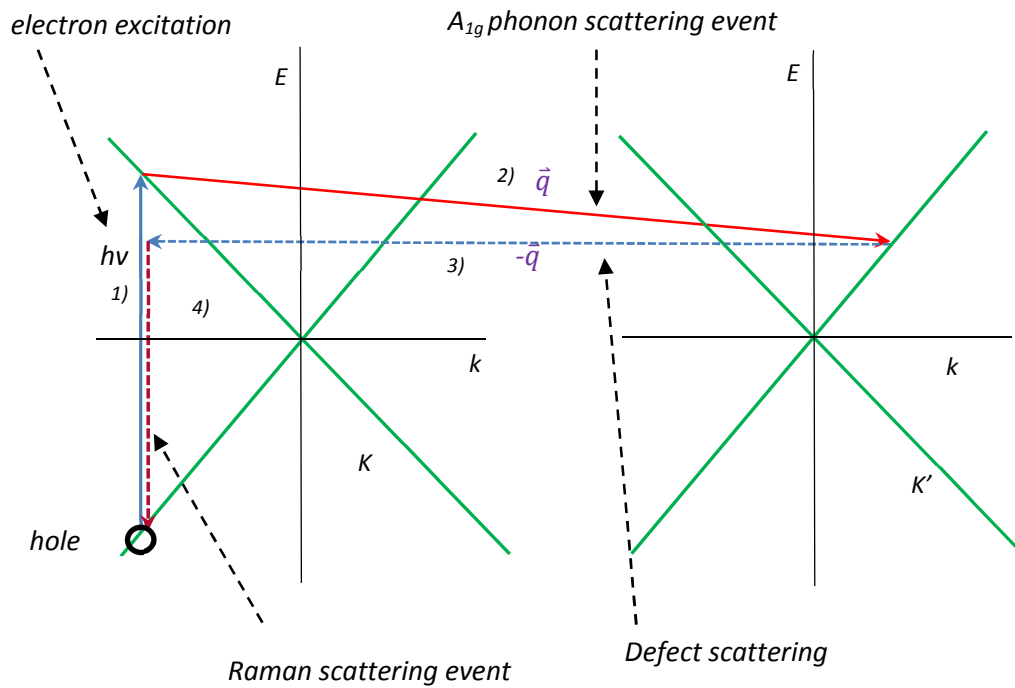


Figure 3.17: Electron band diagram showing the intervally process for the Raman scattering and A_{1g} phonon scattering (red line indicates the electron-phonon scattering event and the blue dotted line represents the Rayleigh scattering event).

- 4) Electron/hole recombination, while releasing Raman scattering light.

The above processes can also be mapped accordingly in the electron band diagram as shown in Figure 3.17, where q is the phonon wave vector.

On the other hand, the G band is activated by the first order scattering of E_{2g} phonon mode which relate to the motion of pairs of sp^2 carbon atoms. It is noted that, the E_{2g} phonon mode occurred at all the sp^2 sites not only in the sp^2 aromatic rings but in the sp^2 chain as well (Ferrari & Robertson, 2000), creating Raman scattering at around $1500\text{--}1630\text{ cm}^{-1}$. It is commonly used for measuring the density of crystallinity for low defect material such as in CNT, graphene and graphite. However, for high defect material such as in GO, the D intensity is used instead for measuring the crystallinity where the details on this matter will be discussed shortly.

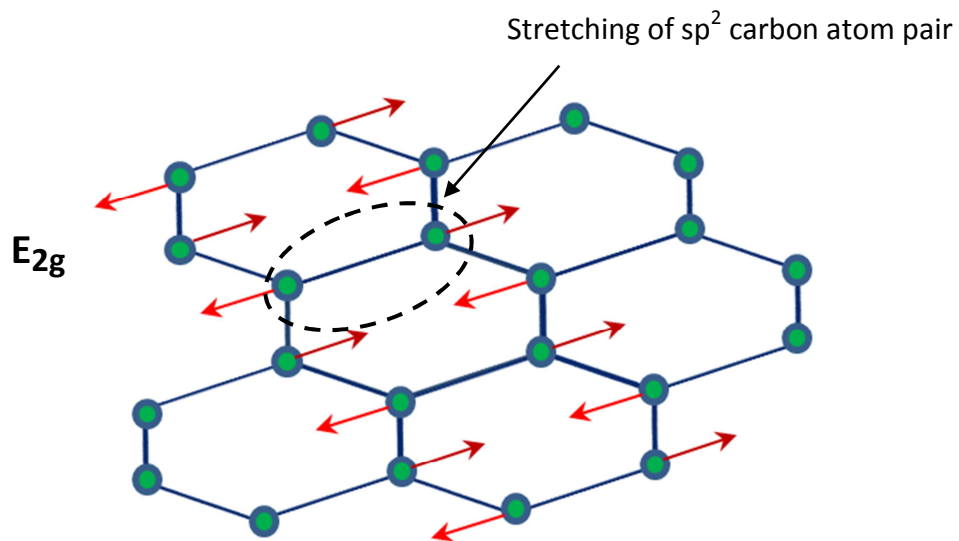


Figure 3.18: E_{2g} phonon eigenvectors (indicated by red arrows) at the sp^2 aromatic cluster region at the GO sheet showing the in-plane bond-stretching motion of sp^2 carbon atoms pairs.

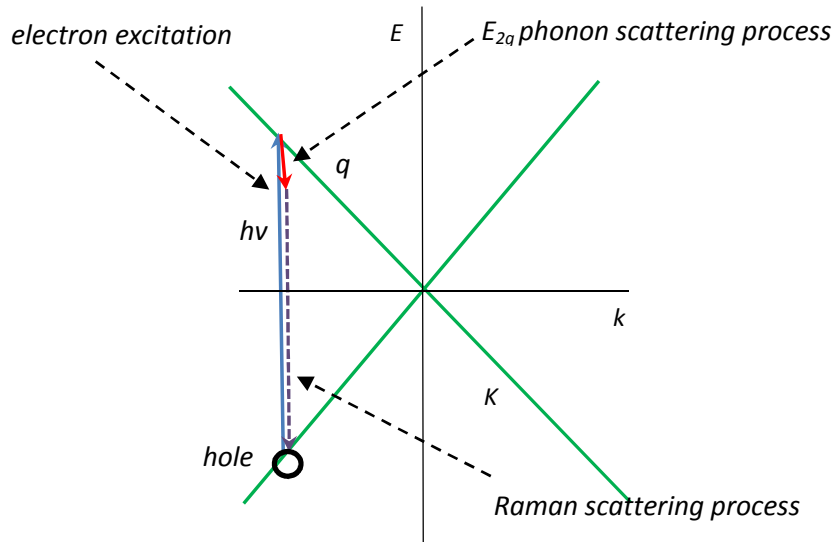


Figure 3.19: Electron band diagram showing the intravalley process for the Raman scattering and E_{2g} phonon scattering.

The in-plane E_{2g} phonon mode with its eigenvectors showing the bond-stretching motion of sp^2 carbon atom pairs (Ferrari & Robertson, 2000, Reich & Thomsen, 2004, Kostić et al., 2009) are presented in Figure 3.18 in the GO sheet. The intravalley process for Raman and E_{2g} phonon scattering that activate the G peak can be explained based on the electron diagram as well as shown in Figure 3.19.

In contrast, E_{2g} mode of CNT splits into two distinct phonons which are G^+ and G^- , where the G^+ peak is usually more intense and its position depends on the tube diameter (Dresselhaus et al., 2005). The G peak splitting is due to electron confinement and curvature of the graphene plane, where pure curvature splits the graphene E_{2g} mode in a component parallel to the tube axis and one perpendicular. However, the G^- peak is not obvious as shown in the spectrum where its location should be at lower Raman shift near the G^+ peak position at 1598 cm^{-1} . The peak of the GO on the other hand is at 1582 cm^{-1} , which is at lower Raman shifts as compared to the CNT. This signature of

downshifts is not an accurate measurement of whether GO has more defect structure than CNT, because those two different SAs have different thickness, which will alter the G position.

For high defect material such as in GO, the D and G intensity ratio (I_D/I_G) is favourable to be used for more accurate estimation on defect level, where the ratio dynamics behave differently at low and high defect density regimes (Ferrari & Robertson, 2000). In addition, the thickness of the material as well will affect the ratio value, where thicker material will increase both the D and G peaks. However, if the thickness is further increased, the intensities can be reduced due to the lack of laser penetration depth (Yang et al., 2013). Despite the increment or decrement of the (D and G peak) intensities in relative to the thickness of the material, the I_D/I_G ratio value will not be altered by a significant. Therefore, the ratio value can still provide the estimation on the degree of defect and the effective sp^2 aromatic cluster size in the GO sample.

For GO, the basal plane is contained with epoxide and hydroxyl groups, while carboxyl and carbonyl groups are bonded at the edges as discussed earlier in this chapter. Figure 3.20 shows a fraction of a GO sheet with parameter L_{A1} and L_{A2} represent the isolated aromatic cluster correlation length and blue circle represent defect due to the oxygen functional groups. The method for estimating the total retained crystalline size for GO material has to be modified from a model presented by Ferrari and Robertson (2000). Since, the aromatic ring cluster size varies in the GO sample; the effective aromatic ring cluster size is defined as followed,

$$L_{Aeff} = \sum_j^N \left[\frac{(\sum_i^n L_{Ai})_j}{Y_j} \right] \quad (3.3)$$

where Y_j is the area fraction of an isolated aromatic cluster in a GO sheet which is calculated by dividing the total area of the isolated aromatic cluster in a sheet per the total area of GO sheet in the whole sample. On the other hand, L_{Ai} is the isolated aromatic cluster correlation length.

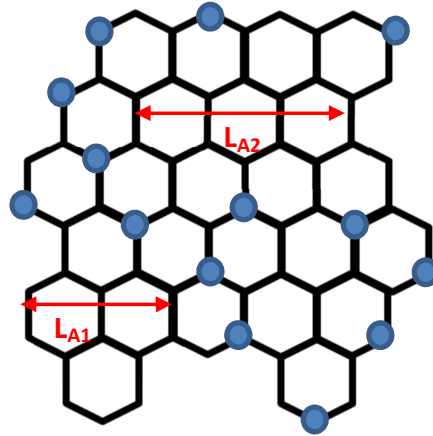


Figure 3.20: Top view of a graphene oxide plane showing the isolated aromatic cluster correlation length, L_A (blue circle indicates defect).

From the GO Raman spectrum, the I_D/I_G intensity ratio value obtained is 0.86, which is in close proximity reported by Sobon et al. (2012), conforming the presence of graphene oxide on the ferrule. As mentioned previously, the I_D/I_G ratio dynamics behave differently at two different defect density regimes. For high defect density material with its corresponding defect geometry boundaries ($L_A < 2$ nm) (Ferrari & Robertson, 2000); the ratio value decreases as the density of defect increases. This is due to the attenuation of D peak intensity owing to the reduction in the number of aromatic ring and the aromatic cluster size. On the other hand, the G peak intensity will be reduced at much lower degree or simply unchanged. This is because the E_{2g} vibrational mode that activates the G peak depends only on the stretching of sp^2 carbon

pairs. Thus, in amorphous carbons such as in GO, the increase of D peak indicates ordering, which behave in an opposite manner as compared to the spectrum for CNT, graphite and graphene. For GO, the relationship between the I_D/I_G ratio and the effective aromatic correlation length can be modified from the ones presented by Ferrari and Robertson (2000) as followed,

$$\frac{I_D}{I_G} \propto L_{Aeff}^2 \quad (3.4)$$

Relationship (3.4) dictates that as the disordered density increases (decreasing the L_{Aeff}), the ratio I_D/I_G will decrease proportionally to the squared of effective aromatic cluster correlation length. In addition, the geometry boundary must be obeyed: $L_A < 2$ nm in order to satisfy the relationship (3.4). For the material to have low defect density ($L_D \geq 10$ nm) such as found in the CNT and graphene, the I_D/I_G relationship can be modelled as followed, is modelled based on point-like defect with the average distance between defect, L_D (Cançado et al., 2011). The relationship between the I_D/I_G ratio and the disordered degree for low defect density material is as followed,

$$\frac{I_D}{I_G} \propto \frac{1}{L_D^2} \quad (3.5)$$

where relationship (3.5) dictates that as disordered density increases (decreasing the L_D), the I_D/I_G ratio will increase inversely proportional to the sum of squared of average distance between defects.

From the Raman spectrum analysis, we can conclude that there is much less in the number of sp^2 aromatic rings in the GO material as compared to CNT and graphene. This will result in low capacity for optical absorption due to the lack of delocalised π -electrons located in the cluster of aromatic rings to absorb photon energies. This analysis can be further supported by the complex refractive index value of $n \sim 1.63 + j0.16$ for a single layer GO reported by Jung et al. (2008). In comparison, a single layer graphene has an average complex refractive index of $n \sim 3 + j1.45$ (Wang et al., 2008, Kravets et al., 2010). From the imaginary components of the refractive index values, it is clear that GO has lower absorption coefficient in comparison. Despite this, GO has the lower refraction coefficient which is strongly influenced by the intercalated water in the GO layer (Jung et al., 2008). The intercalated water layers produce low material density with the nanosheets are dispersed and thus decreases the effective refractive index. With a reference to a refractive index of a silica glass fiber of 1.44; GO can exhibit the lower scattering loss with the refractive index increases as the number layer of the nanosheet increases. However, this information is not sufficient in order to determine the actual SA nonsaturable absorption and thus the modulation depth, since this parameter encompasses many other variables such as the surface roughness where this parameter is generally neglected when the refractive index of a material is calculated from ellipsometer measurements (Fenstermaker & McCrackin, 1969).

3.6 Summary

The GO in this work has been produced from pure graphite flakes using simplified Hummer's method which is simpler and cost-effective method to produce as compared to the methods demonstrated by Marcano et al. (2010) and Brodie (1859). Extensive material characterisations are performed at the GO liquid and solid-states based on the UV-vis and Raman spectra analysis. From UV-vis spectrum, an absorbance intensity of 2.29 at 228 nm and a small shoulder peak at 300 nm wavelength are obtained. This

result is similar to the ones reported by Shang et al. (2012) which confirms the success in the production of pure graphene oxide colloid. Moreover, the higher peak to shoulder absorbance intensity ratio with a value of 3.26 as compared to the work demonstrated by Marcano et al. (2010) with intensity values of 3.14, 1.95 and 2.28 and from Mei et al. (2010) with the value of 2.17; suggests that the GO sample in this work has higher number of sp^2 carbon aromatic rings.

Then a solid-state GO in a form of a film has been fabricated on a 90 mm petridish through drop-casting method and the coupling method of the film-piece to the fiber ferule facet has been demonstrated. Moreover, important principles related to the Raman spectrum analysis for high defect GO material have been studied that will be useful to evaluate on the other type of GOSA in later chapter and perform further analysis. The Raman spectrum shows the G and D peaks of the GO film are located at 1354 cm^{-1} and 1582 cm^{-1} where the intensity ratio (I_D/I_G) of 0.86 is obtained conforming the presence of GO with having high degree of defects in its crystalline structure as compared to CNT. This is due the presence of the oxygen functional groups bonded in the GO sheet. Furthermore, the modified relationships between the intensity ratio (I_D/I_G) and the effective aromatic cluster correlation length which describes the disordered degree of the GO sheet and its retained crystal domain have been established.

From the Raman analysis, it is confirmed that the GO has much less number of aromatic rings as compared to graphene and CNT in which degrades the capacity for optical absorption. However, the lower refractive index of GO due to the intercalated water layers compensate this weakness that will also affect the modulation depth of a SA which rely both on the saturable absorption and non saturable absorption loss properties. Nevertheless, the number of aromatic rings can be increased by yielding larger sheet size of GO. This can probably be accomplished by controlling $KMnO_4$:acid

(H₂SO₄:H₃PO₄) weight ratios, as demonstrated by Huang et al. (2011); with higher ratio gives higher oxidation level and thus promote larger GO sheet size and more aromatic rings. However, the degree of improvement is unsure until proper measurement is performed.

CHAPTER 4: Q-SWITCHED FIBER LASER BASED ON GRAPHENE OXIDE FILM USING A 21 CM LONG BISMUTH ERBIUM-DOPED FIBER AS THE GAIN MEDIUM

4.1 Introduction

In the previous chapter we have successfully fabricated and characterised graphene oxide (GO) film, where in this chapter an experimental work for Q-switched laser generation using the GO film as saturable absorber (SA) will be demonstrated. Recently, Cao et al. (2013) has demonstrated a Q-switched fiber laser system using graphene as SA, conventional erbium doped fiber (5 m long), and tunable filter that provides Q-switched threshold of 35 mW, maximum repetition rate of 9.7 kHz and 1.2 mW of average output power. Moreover, at the pump power of 55 mW, he had obtained a pulse width of 4.6 μ s.

In this work, a 21 cm long Bismuth-based Erbium-doped fiber (Bi-EDF) is used as a gain medium along with the GO film. The very short fiber length of the highly doped with Erbium ions will be used to shorten the resonator length in order to promote single longitudinal mode operation and to shorten the Q-switched pulse width. Cao et al. (2013) work will be used as a reference to validate the experimental data in this chapter. Furthermore, the experimental results will be compared and discussed with the theories presented in chapter 2 in order to explain the dynamic laser behaviour and to further characterise the laser pulses. For practical purposes, the stability of the generated pulsed laser will also be evaluated using radio frequency spectrum analyser and the formula derived by Von der Linde (1986) in order to determine the pulse energy fluctuation.

4.2 Experimental arrangement for the proposed Q-switched Bi-EDF laser

Towards generating the Q-switched laser using the GOSA film, a GOSA assembly is constructed as shown in Figure 4.1 to ensure the GOSA film is protected from contamination and to avoid major displacement. The assembly can be easily employed in the laser resonator through FC/PC patchcords (SMF-28) connection. Fiber ferule 1 that is attached with the GO film as previously prepared is sandwiched with a fiber ferule 2 through FC/PC adapter where the GO film covers entirely the optical path so that Q-switching can occur effectively in a laser resonator.

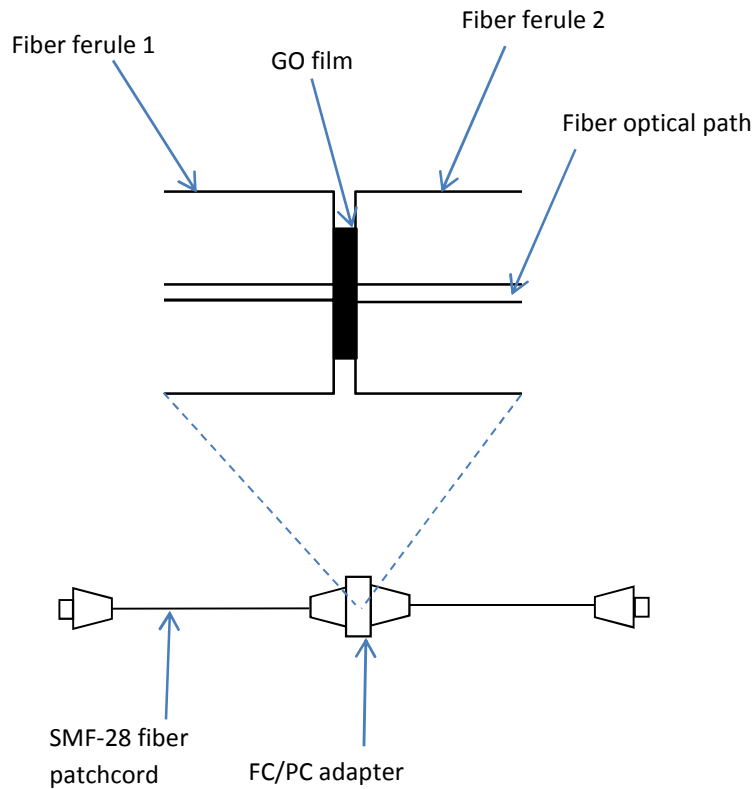


Figure 4.1: Schematic of the GOSA assembly (not to scale).

In order to generate Q-switched laser using the GOSA film, a ring laser configuration is setup as shown in Figure 4.2. A ring setup was chosen since it provides unidirectional light propagation which allows effective amplification and lower mode competition in the resonator as compared to linear configuration (Hamzah et al., 2010). The lesser mode competition found in the unidirectional ring configuration is due the absence of spatial hole burning effect. In a linear configuration, the effect is the result of

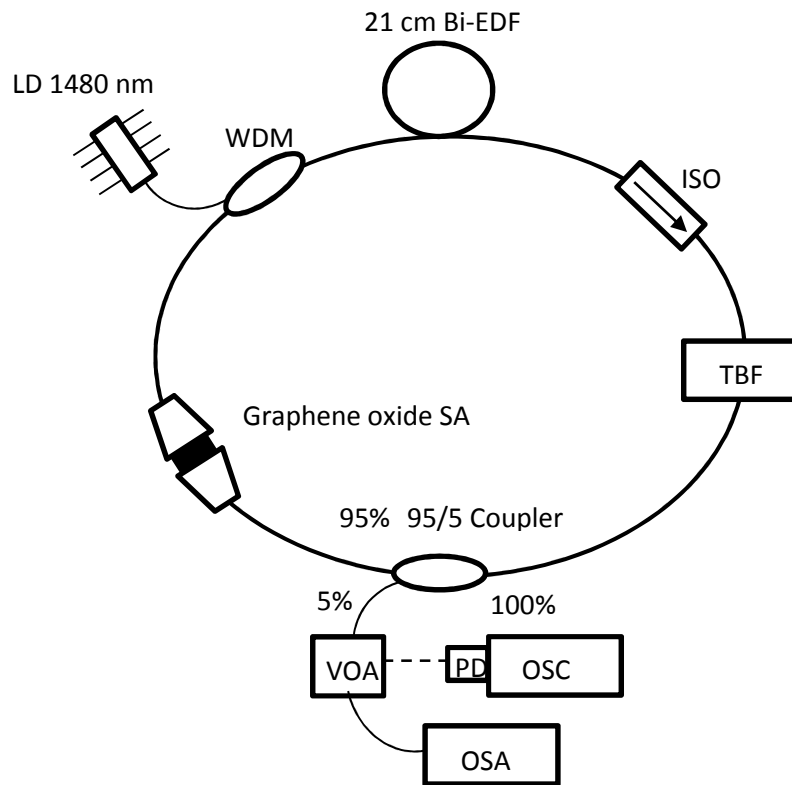


Figure 4.2: A ring Bi-EDFL configuration. WDM: wavelength division multiplexer; TBF: tunable bandpass filter; VOA: variable optical attenuator; PD: photodetector; OSC: oscilloscope; and OSA: optical spectrum analyser.

superposition of two counter-propagating waves such that they produce a standing wave in the gain medium which depletes the gain in all the nodes of the standing wave pattern. By utilizing a ring resonator design, standing waves are nonexistence instead the laser oscillations will exhibit travelling wave property to promote single-

longitudinal mode operation. Moreover, the ring laser power and frequency are bound to be more stable than the linear resonator. However, fiber ring lasers can still oscillate in multi modes due to having long resonator length from several to tens meters.

In this work, a 21 cm long Bismuth-erbium doped fiber (Bi-EDF) obtained from Asahi Glass Co. Ltd, Japan is used as the gain medium to generate amplified spontaneous emission (ASE) and to promote shorter resonator length. It has an erbium ion concentration of 6300 ppm as well as a core refractive index of about 2.03 and cladding refractive index of 2.02 at 1550 nm. The Bi-EDF is co-doped with lanthanum to suppress concentration quenching of erbium ions and to increase concentration of erbium ions to more than 3000 ppm. The high refractive index of Bismuth-based glass produces in relatively shorter $^4I_{13/2}$ level life time (Sugimoto, 2005). Moreover, the Bismuth fiber is fusion spliced with high numerical aperture SiO₂ based fiber to suppress the reflection effect due to the large refractive index mentioned. The peak absorption of the Bi-EDF is about 133 dB/m at a wavelength of 1480 nm where it is pumped by a 1480 nm laser diode through a 1480/1550 wavelength division multiplexer (WDM). The laser pump at 1480 nm wavelength will promote higher slope efficiency than by pumping at 980 nm but however, the gain efficiency will be much lower than 980 nm. This is due to that fact that the 1480nm pumping will benefit from a better quantum conversion efficiency and gain coefficient. However, it is noted that the 1480 nm pumping will have higher lasing threshold than 980 nm pump which is caused by the lower absorption rate found at 1480 nm band for the Bi-EDF.

In comparison to the traditional EDF, that requires a longer fiber length (typically at around 2-3 meters) to provide enough gain for laser generation. Moreover, the erbium dopant concentrations are limited in conventional silica based fibres due to the clustering effect, consequently inducing concentration quenching and degrade the

performance of the EDF (Deleuaque et al., 1993, Harun et al., 2003, Harun et al., 2005). In this manner, the Bi-EDFs will provide a viable alternative to silica fibres as they can host a high erbium dopant concentration, allowing for short, highly doped EDFs to be realized. In subsequent, this allows for short resonator length to be constructed in order to generate stable and clean pulses with the reduced in pulse width as compared to having longer resonator length. This is possible with the short length of gain medium because it reduces the resonator loss, dispersion and resonator round-trip time. Moreover, the Bi-EDFs also have the advantage of a wideband emission spectrum, easy refractive index control and high reliability. On top of this, it has a wide absorption band makes it easy to be pumped by commercially available powerful laser diodes, to realise an ultra-compact fiber lasers and amplifiers (Shahi et al., 2009, Ahmad et al., 2009, Salem et al., 2011, Ahmad et al., 2010, Ahmad et al., 2010).

In the setup, an isolator is used to force the light oscillation in a clockwise direction, and it is connected to a tunable bandpass filter (TBF), with the other end of the TBF is connected to a 95:5 fused coupler at a common port. The TBF is obtained from Newport where its specifications are presented in Table 4.1. A 0.8 nm bandwidth for bandpass further forces the laser to operate in single longitudinal mode. The filter features a maximum insertion loss of 3 dB (measured at 1535 nm), maximum back reflection of -50 dB and a 1535–1565 nm tuning range for laser tunability. The bandpass selection wavelength can be shifted at a 0.05 nm resolution across the wavelength range by adjusting a micrometer.

Table 4.1: Tunable band pass filter specifications.

Wavelength Tuning Range (nm)		1535 to 1565
Tuning Resolution, Typical (nm)		0.05
0.5 dB Bandwidth, Maximum (nm)		3.5
20 dB Bandwidth, Maximum (nm)		3
Insertion Loss, Maximum (dB)		3
Back-Reflection, Maximum (dB)		-50
Polarization Dependent Loss,	Typical 0.05 dB, typical @ 1565 nm; 0.3 dB @ 1535 nm	
Center λ Stability (nm/°C)		0.005
Thermal Limit (dB/°C)		0.005
Fiber		9/125 singlemode

The GOSA assembly is employed in between the WDM and 95:5 fused coupler through FC/PC connections as shown in Figure 4.2. The 5% output of the fused couplers is connected to a variable optical attenuator (VOA), where attenuation can be adjusted accordingly in which a photodetector, PD (Hewlett Packard Lightwave Detector DC-6 GHz) can be safely used to detect the laser light. The fast response PD has a bandwidth of 6 GHz and a wavelength spectral response of 1000-1600 nm. The PD is connected to an oscilloscope, OSC (Le Croy 500 MHz) via SMA to BNC adapter for electrical time domain measurement to observe and analyse Q-switched pulse pattern. Measurement tools such as an optical spectrum analyser, OSA (Yokogawa-AQ6370C) and so on are shown in Figure 4.3. The OSA is calibrated and used to measure the ASE and laser spectrum accurately while an optical power meter is used to measure average power of the Q-switched laser. Moreover, the laser pulse stability is analysed using radio frequency spectrum analyser, RFSA (Anritsu - MS2665C) which will be further discussed in the next section.



Figure 4.3: Q-switched fiber laser measurement tools. Starting from the top left hand corner in clockwise direction: Optical spectrum analyser (Yokogawa-AQ6370C), radio frequency analyser (Anritsu - MS2665C) and oscilloscope (Le Croy 500 MHz).

4.3 Experimental results and discussion

Figure 4.4 shows the amplified spontaneous emission (ASE) spectra of the Bi-EDF as pumped by a 1480 nm laser diode at different pump powers. From the figure, it can be seen that the Bi-EDF relatively produces a broader ASE spectrum as compared to that obtained from conventional silica-based EDFs. The ASE spectrum were measured at 0.05 nm resolution, where it stretches from about 1490 nm to 1610 nm, forming a spectral bandwidth of about 120 nm. At lower pump powers, the ASE spectra resemble a bell curve, rising slightly before plateauing and subsequently declining again. This is a result of the high erbium ion concentration, which reabsorbs the emissions of the ASE at shorter wavelength (1500-1530 nm) and leaving emission in the L-band region dominant. As the pump power is increased, the conventional peak at 1530 nm for EDFs begins to be seen corresponding to the increase in population inversion. It is noted that, due to the highly doped erbium ions in the fiber, the available pump power is limited to

fully pump the Bi-EDF for attaining higher gain. However, in the experiment, the generation of the Q-switched laser is demonstrated within the limit of the pump power.

The gain Q-switching pulse train is started to obtain at pump power of 65 mW. Figure 4.5 shows the tunability of the Q-switched laser spectrum measured at 0.05 nm resolution and pumped at 92 mW when the GOSA assembly is employed in the resonator. Laser tunability is obtained by adjusting the TBF to the desired wavelength. In can be seen from the wavelengths generated, the lasers have an average power of -

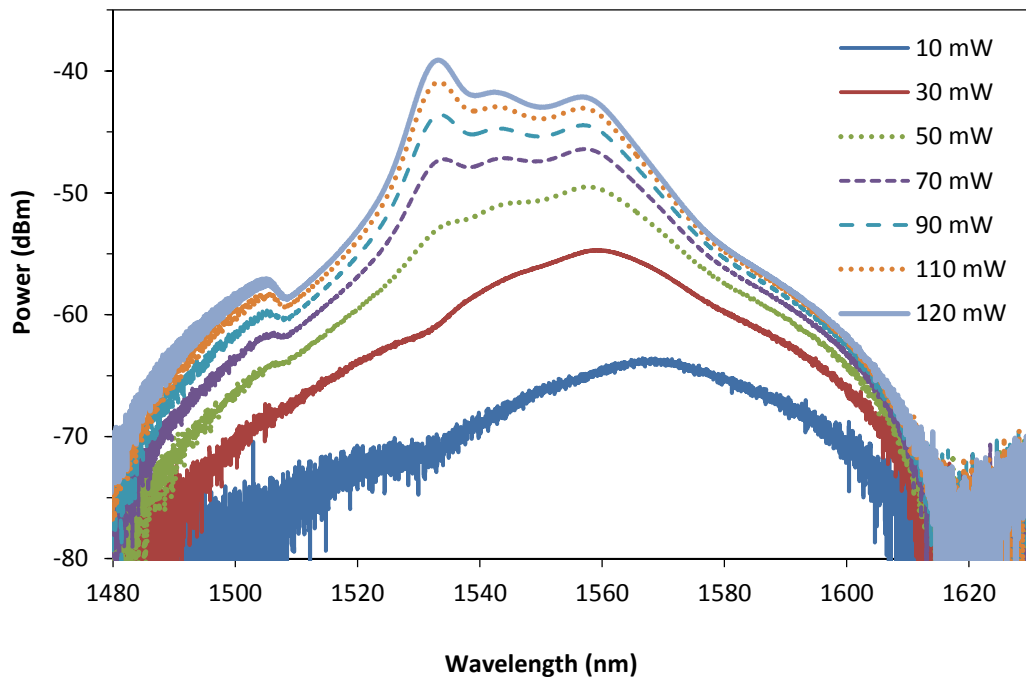


Figure 4.4: ASE spectra of the Bi-EDF at various 1480 nm pump powers.

16.8 dBm, with a tuning range of approximately 1550 nm to 1564 nm. The Full-Width at Half-Maximum (FWHM) is about 0.1 nm with an average signal-to-noise ratio (SNR) of about 56.6 dB. It is expected that higher laser powers can be achieved with higher pump powers, and the tuning range can also be extended. However, the range it limited

based on the gain profile of the Bi-EDF and the bandpass tuning range provided by the TBF. The gain bandwidth of the Bi-EDF can be approximately estimated based on the ASE generated from the gain medium. For example, from Figure 4.4, at around pump power of 92 mW, the ASE can relatively generate laser at a range of about 1530 to 1565 nm. However, it is noted that the actual gain profile cannot be inferred from the ASE spectrum and this is due to the fact that there exist some relatively high absorption band with its peak at around 1530 nm.

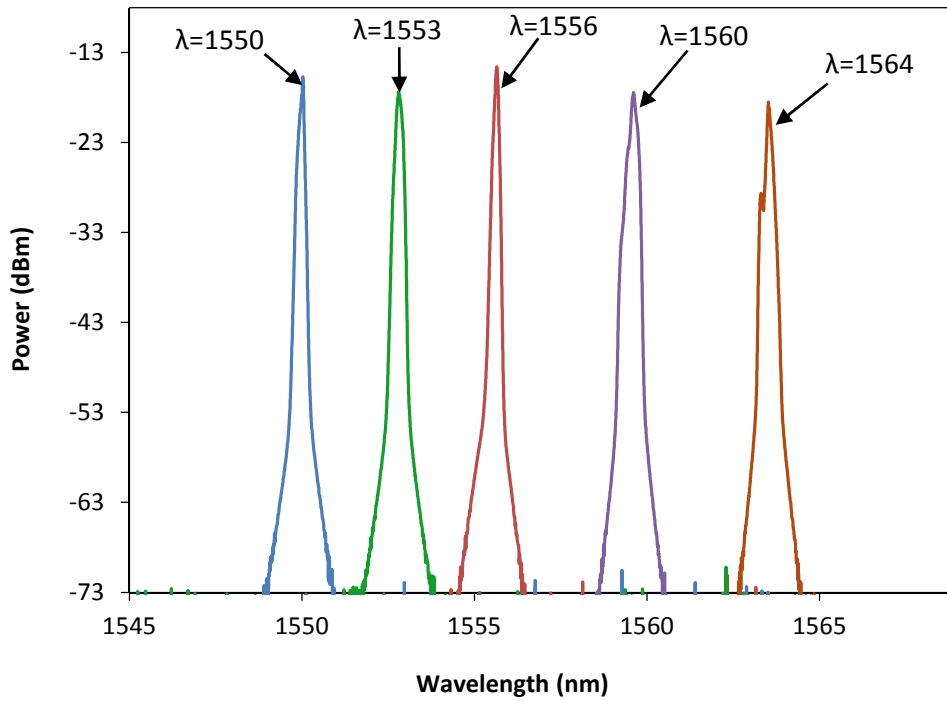


Figure 4.5: Q-switched laser spectra at different wavelengths tuned by a TBF at a fixed pump power of 92 mW. The base power is set at 73 dBm for clarity.

Fig. 4.6 and 4.7 show the generated Q-switched pulse trains and pulse profiles measured using the oscilloscope (OSC), under pump powers of 92 mW and 118 mW respectively at 1556 nm laser wavelength. The repetition rate of the train pulse is a measurement of how fast the formation of pulses in the laser resonator, while the pulse width or pulse duration is measured based on the full-width at half maximum (FWHM).

The figures are plotted at microsecond time scale to observe the pulses clearly, while the pulse intensity is normalized to arbitrary unit. From the figures, we can infer that the repetition rate increases while the pulse width decreases as the pump power is increased with the pulse narrows from 11.7 μs to 7.7 μs , while the repetition rate increases from 21.8 kHz to 27.2 kHz. At 92 mW of pump power, there are 13 pulses captured within 600 μs time span. In contrast, at 118 mW of pump power, there are 17 pulses captured in the same time span where at both conditions, the amplitude fluctuations are at minimal. The measured and calculated pulse intensity standard deviations (ΔI) for both pulse trains are $\pm 0.555\%$ and $\pm 0.539\%$ at the pump powers of 92 mW and 118 mW respectively, which indicates that at higher pump power, there is less amplitude fluctuation. The ΔI decrement of 0.013% per the increment of 26 mW is obtained, which also shows that the amplitude fluctuation does not differ that much at the two different pump powers mentioned. It is noted that the same sample size is considered to calculate the statistical values respectively where the values demonstrates that laser generation is stable at both of the pump powers which is mainly contributed by the ring configuration scheme and the TBF.

Furthermore, the change of the pulse pattern in respect to the increased of pump power can be explained based on the equations presented in chapter 2, sections 2.3. The rate equation (2.3.1) presented in the respective section describes that higher population inversion density of the gain medium is produced at higher pump power. This in turn increases the growth rate of photon density, resulting quicker time in the formation of

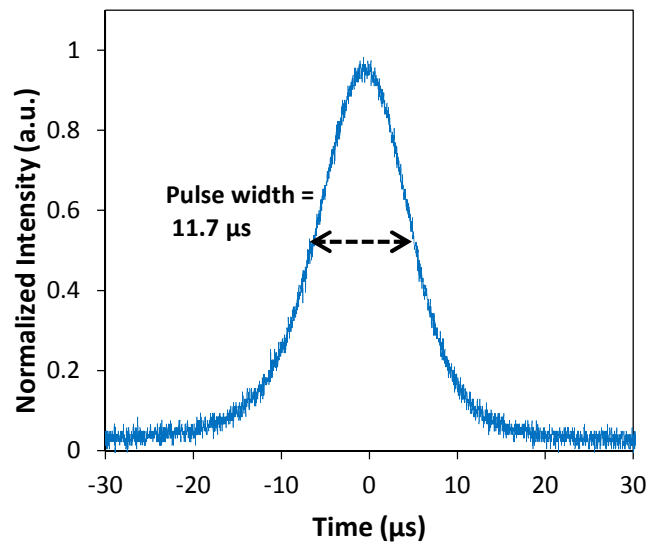
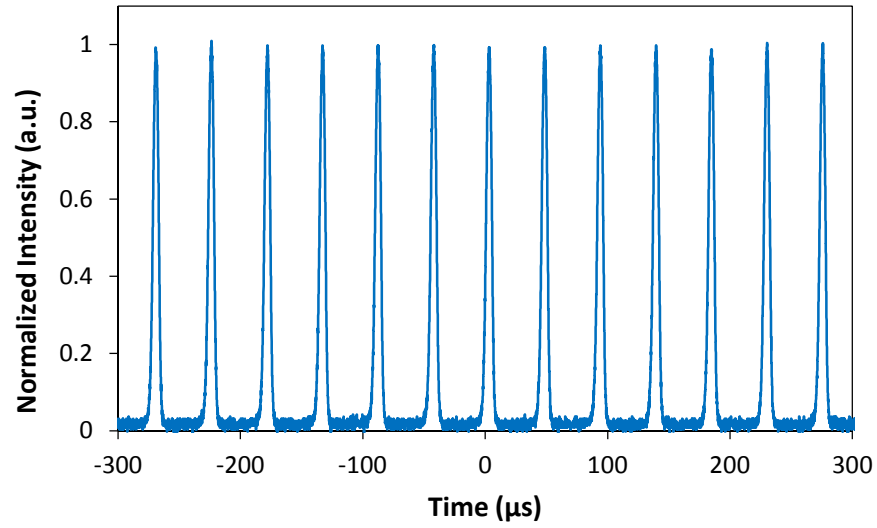


Figure 4.6: Pulse train and a single pulse profile of the Q-switched Bi-EDFL under pump power of 92 mW at 1556 nm laser wavelength. The repetition rate of 21.8 kHz and pulse width of 11.7 μ s are obtained.

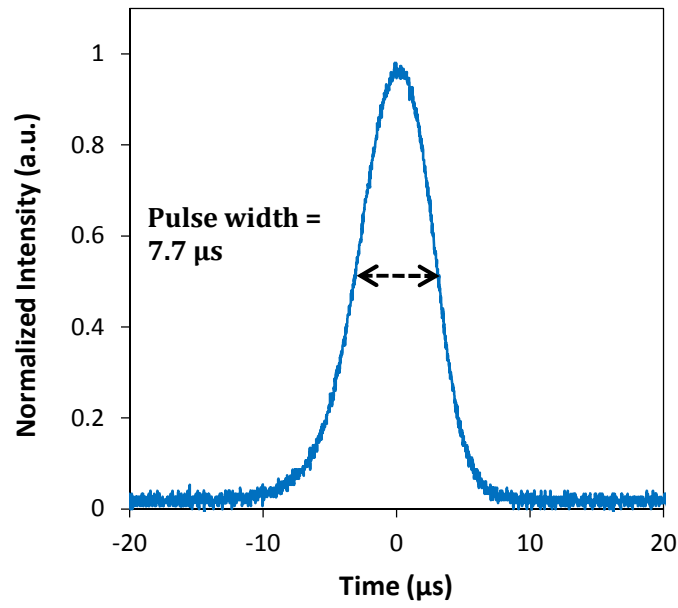
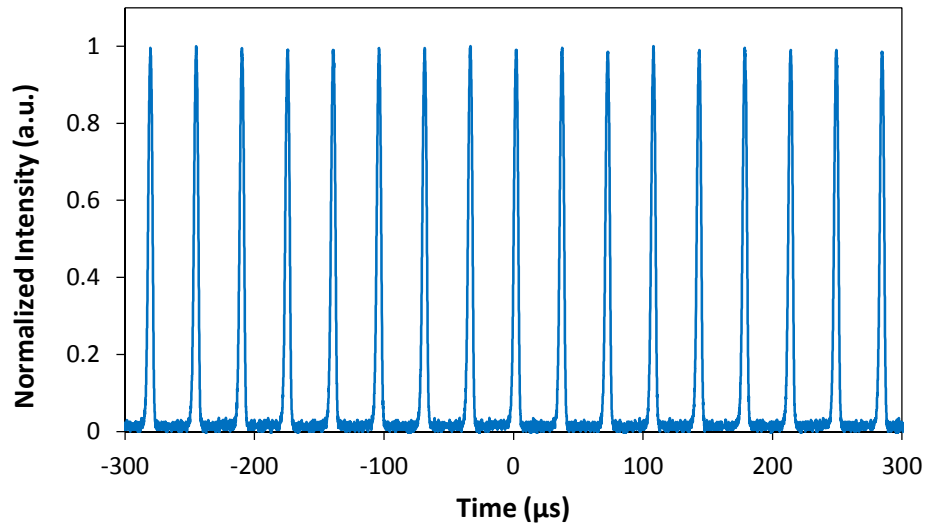


Figure 4.7: Pulse train and a single pulse profile of the Q-switched Bi-EDFL under pump power of 118 mW at 1556 nm laser wavelength. The repetition rate of 27.2 kHz, and pulse width of 7.7 μ s are obtained.

pulses giving higher repetition rate. Moreover, the narrower pulse width obtained at a higher pump power is due to less time for photon density growth and less time for the depletion of population inversion, which satisfies the rate equations (2.3.1) and (2.3.2). The shape of a single pulse is also an important parameter; with details of the pulse profile is useful for applications such as in telecommunications where it is required in order to design a proper receiver for effective detection of the Q-switched pulse train. Typically, the skewness of a pulse characterises the pulse shape where it depends highly on the ratio value between the population inversion density when the pulse build-up begins, N_{gi} and the population inversion density when the pulse peak is reached, N_p (Qin-Yong et al., 2011). As the ratio (N_{gi}/N_p) value increases, the pulse shape skewness becomes greater as described by Qin-Yong et al. (2011). The obtained single pulse profiles (Figure 4.6 and 4.7) suggest that the (N_{gi}/N_p) ratio values are low at both pump powers which produce a nearly a Gaussian-like shape with its symmetrical property. Moreover, at higher pump power, which produces higher pulse repetition rate, the N_{gi} value with its equation (2.5.3) presented in chapter 2, section 2.5, will be increased. As a result, the ratio value (N_{gi}/N_p) increases and pulse skewness will become greater. This is evident as shown in figure 4.6 and 4.7, which shows that at higher pump power (Figure 4.7); the pulse skewness is slightly greater.

Fig. 4.8 shows the Q-switched pulse dynamics in terms of pulse repetition rate and pulse width at a wider range of pump power. The threshold point for q-switching is observed at about 65 mW, where it changes from continuous wave (CW) operation into Q-switched pulses by carefully adjusting the pump power and observing the pulse pattern on the OSC. The high laser threshold obtained is due to the large Er^{3+} ion cluster size found in the highly doped Bi-EDF where this property reduces the $^4I_{13/2}$ level life time. This promotes carrier recombination and thus reduces the quantum efficiency

transitions for lasing. The small pump power window for CW operation prior to Q-switching happens due to the insufficient gain for pulse build-up and having the Q- in

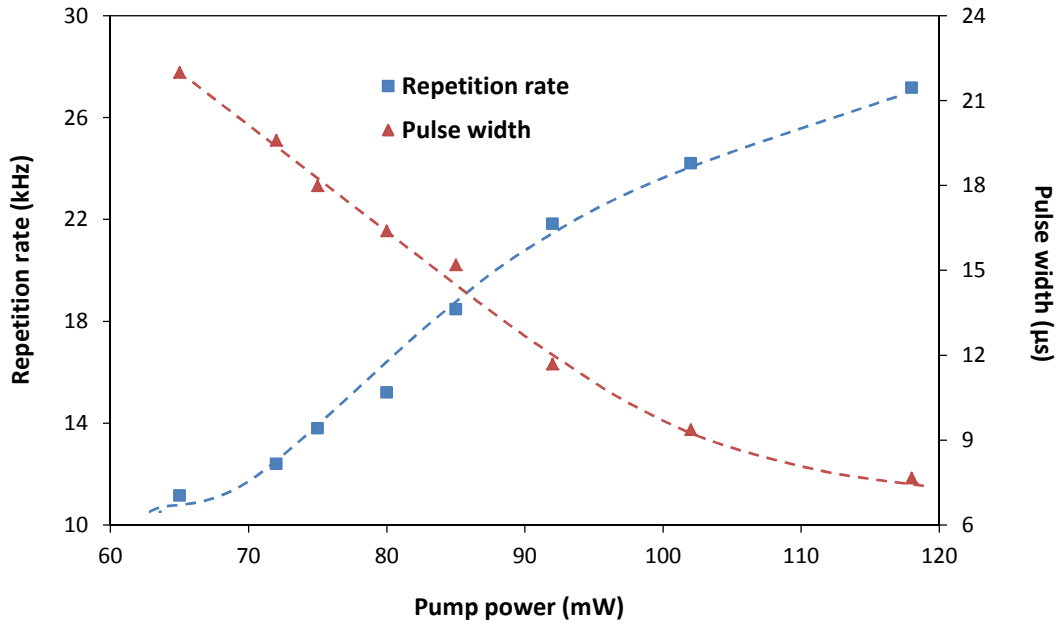


Figure 4.8: Pulse width and repetition rate characteristics of the Q-switched Bi-EDF laser at the wavelength of 1566 nm.

switched threshold factor unsatisfied, where the expression has been presented in Chapter 2, section 2.4. At this condition, the GOSA saturable absorption loss is less dominated in the resonator and as a result the GOSA saturates more slowly than the Bi-EDF gain medium.

However, at the Q-switched threshold, the gain is high enough and the GOSA starts to saturate faster than the Bi-EDF where the resonator sees a dramatic reduction in the intra-resonator loss to form repetitive Q-switched laser pulses with a repetition rate of about 11.2 kHz. Another factor that can contribute to the high Q-switched threshold is due to the low absorption coefficient of the GOSA, where the small size of sp^2 aromatic domain is the reason for this issue as discussed in chapter 3. This statement can be

supported by the saturation intensity equation (2.6.3) which has been presented in chapter 2, section 2.6; where the absorption cross section can be proportional related to the sp^2 aromatic cluster size. In addition, the saturation time for GOSA film is also affected by the nonsaturable loss caused by the film surface roughness. Although, the refractive index of GO material is somehow lower than graphene, as discussed in chapter 3, the value is not taken into account the surface roughness which can significantly raises the refractive index and contribute to scattering loss. It is noted that, the surface roughness is found to be unavoidable by the current fabrication method and different approach such as using spin-casting technique can be used to yield smoother surface area and thinner GO film. A thinner and less wrinkle GOSA can reduce the refractive index and thus can reduce the scattering and laser beam divergence effects.

The repetition rate is observed to be increased in a hiccup manner at the low pump power, and subsequently increased in a fairly linear manner to a value of 27.2 kHz when 118 mW of pump power is reached. It is believed that further increase in the pump power will further increased in the repetition rate (Hakulinen & Okhotnikov, 2007) and its increment is limited depending on the GOSA damage threshold. The repetition rate characteristic is highly depends on the saturable absorption property of the GOSA as described in the photon density rate equation (2.3.1). It dictates that the SA absorption ground cross section, excited state cross section, thickness and the amount of the population density in the GOSA have a decrement effect on the increase rate of photon density. By having larger values of the mentioned parameters, the repetition rate of the Q-switched laser will be reduced. On the other hand, the pulse width is observed to be decreased linearly and subsequently in an exponential manner as the pump power is increased, from a high value of about 22.0 μs at a pump power of 65 mW, and dropping to about 7.7 μs at a pump power of 118 mW. At the pump power of about 105 mW, the decaying curve shows a significant decreased in slope, indicating a signature of

saturation in the pulse width dynamics (Hakulinen & Okhotnikov, 2007). This is due to the GOSA has nearly reached its maximum pulse modulation capability; dictated by the saturation absorption and nonsaturable loss properties or simply the modulation depth of the SA. In order to achieve shorter pulse width, the resonator length has to be reduced and the modulation depth of the GOSA needs to be increased.

However, the lack of delocalized π -electron and the rough surface of the GO film; the modulation depth can significantly be reduced by the low absorption coefficient and the high nonsaturable loss. In addition, although we had used a short length of Bi-EDF in this experiment, the total length of the resonator was still not optimized, therefore the minimum pulse width obtained (7.7 μ s) was still considerably to be long in relative to the pump power. Nevertheless, the minimum pulse width was not achieved in the experiment due to the limited pump power available, which can be obtained when the pulse width curve has reached the saturation level. By taking the advantage of the Bi-EDF and further optimize the problems mentioned, a better performance of Q-switched fiber laser could be obtained.

The average output power and pulse energy of the Q-switched laser at different pump power is shown in Figure 4.9. When the pump power is increased from 65 to 118 mW, the average output power increases in almost linear manner, from about 0.03 to 0.11 mW. The linearity pattern proves that the Q-switched laser behaves in a stable manner as found in other CW and Q-switched laser systems. It is noted that, the average output power represents the energy of a single pulse times the repetition rate. The linear curve has a slope efficiency of approximately 0.2%, where the low optical efficiency obtained is mainly due the low quantum efficiency of the highly doped Bi-EDF, the nonsaturable loss and also might be due to the excited state absorption (ESA) of the GOSA film.

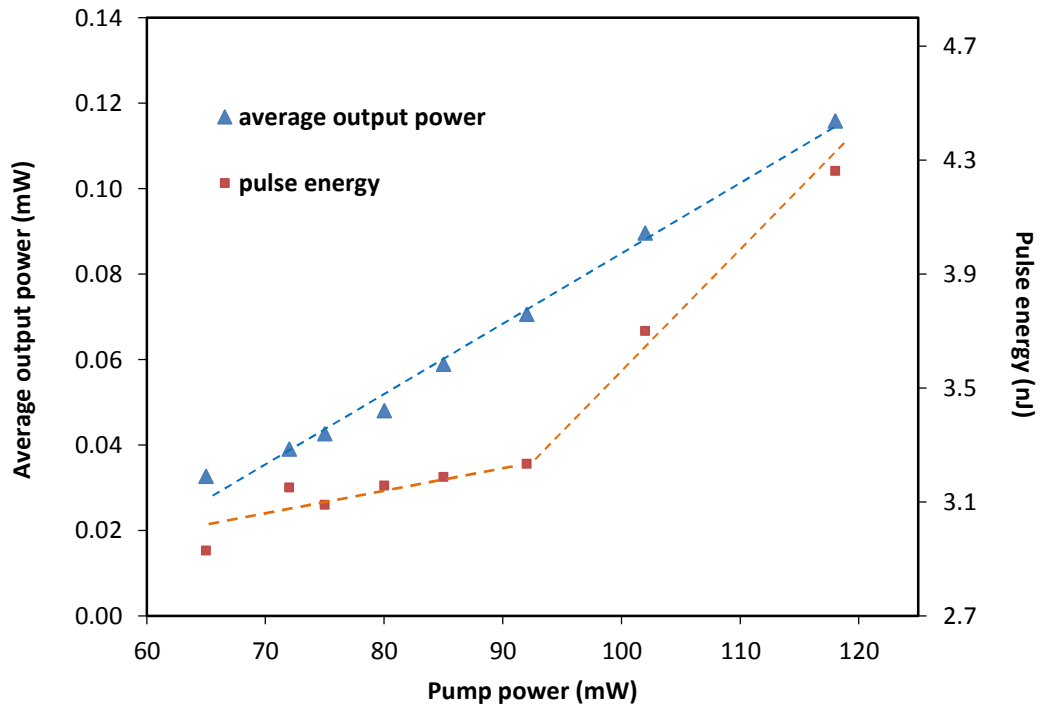


Figure 4.9: Average output power and pulse energy of the Q-switched Bi-EDFL as a function of incident pump power.

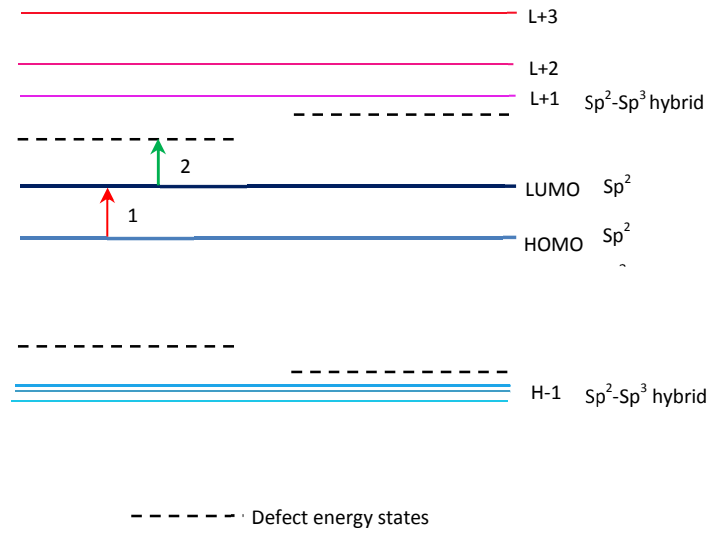


Figure 4.10: Quasi-molecular orbital energy levels and electronic transitions for the saturable absorption process in graphene oxide material.

The non-linear saturable absorption process of the GOSA film at the C-band wavelength can be predicted from the quasi-molecular orbital energy levels modelled by Shang et al. (2012) and Shang et al. (2014), as shown in Figure 4.10. During the saturable absorption, the electronic transitions most likely to occur are from the HOMO to LUMO states (transition 1) by one photon absorption process at the isolated sp^2 aromatic sites. It is noted that, the two-photon absorption is less likely to happen in a Q-switched operation as compared to mode-locked laser operation which having higher peak power. When the GOSA film saturates at high optical intensity, the population density at the LUMO will be large, thus there is a probability that the ESA (transition 2) could occur. The probability is higher if the GOSA film has larger LUMO energy state cross section than the HOMO state cross section in respect to the C-band wavelength. As a result from this effect, the pulse energy transmission and the optical efficiency of the laser resonator are decremented.

On the other hand, the pulse energy pattern at different pump powers is calculated based on dividing the average output power with the repetition rate as shown in Figure 4.9. The pattern shows that the pulse energy increases at a slower rate at low pump powers, but rises sharply above 92 mW of pump power until the value of 118 mW is achieved. At 92 mW, a 3.2 nJ of pulse energy is obtained and increases to almost 4.3 nJ at the pump power of 118 mW. The sharp increase of the pulse energy curve after the pump power of 92 mW is due to the declining slope of the repetition rate as shown in Figure 4.8, with high pulse energies can be built at low repetition rates. Higher laser output powers and larger pulse energies can be achieved by having a higher powered pump laser, lower nonsaturable loss and by optimising the laser resonator design, such as changing the coupling ratio and minimising the resonator loss (Zayhowski & Kelley, 1991).

Fig 4.11 shows the peak power at different pump powers, where it represents the optical power of a single pulse. The peak power is calculated by dividing the pulse energy over the pulse width which was computed from the previous data. At the Q-switched threshold, the peak power of 0.13 mW is obtained, where it gradually increases to a value of 0.21 mW at the pump power of 85 mW having a linear slope efficiency of 0.4%. As the pump power rises above 85 mW, the curve increase sharply in a linear manner with slope efficiency of 0.7% until it reaches the maximum value of 0.56 mW at the 118 mW pump power. The peak power curve shows an almost similar pattern as the pulse energy curve, however the sharp increase is observed at 85 mW instead at 92 mW since the peak power rely on both of the repetition rate and pulse width dynamics.

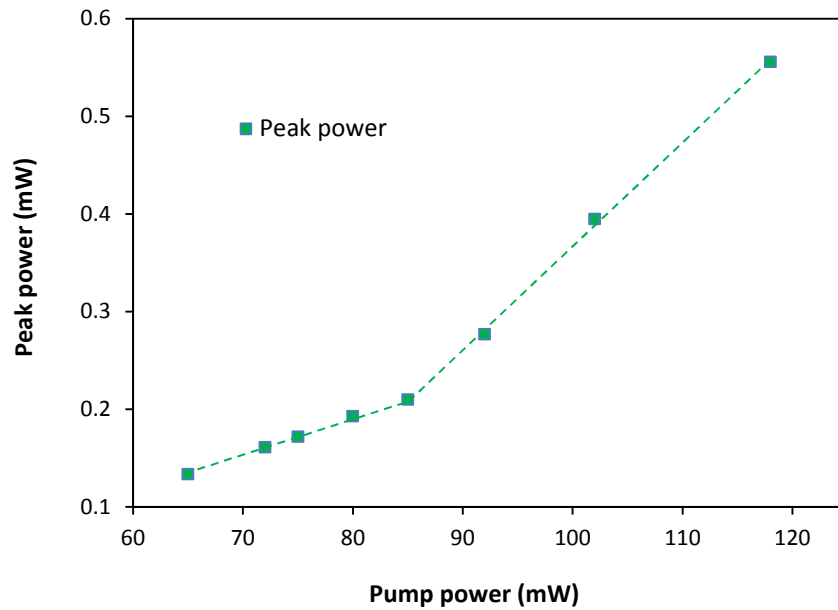


Figure 4.11: Peak power of the Q-switched Bi-EDFL as a function of pump power.

Pulse stability is another important issue that must be considered before it can be used in practical applications. It is noted that, all practical Q-switched laser will exhibit some random changes of the pulse properties rather than being a perfect periodic replica of each other. This is due to that each pulse builds up independently from ASE and due to the ASE and gain fluctuations, the pulse timing, energy and duration will experience some fluctuations. At a certain time, when a pulse exhibits the highest pulse energy will also have the shortest pulse width, which dictates that the pulse amplitude and width fluctuations parameters are somehow mutually correlated. This event is occurred when an above-average stored energy in the gain medium before the pulse formation causes

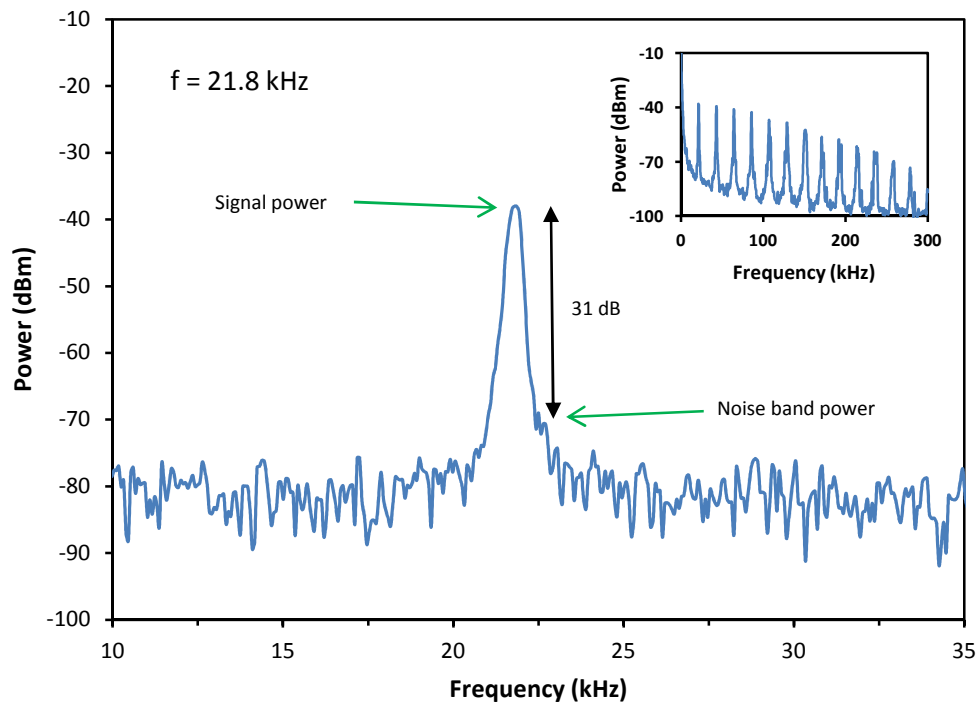


Figure 4.12: RF spectrum of a Q-switched pulse laser, at 1556 nm, as obtained from the RFSA at the pump power of 92 mW. The fundamental frequency of the pulse is 21.8 kHz. Inset shows the RF harmonics of the Q-switched pulse laser. The RFSA was set at a span of 25 kHz, with a Resolution Bandwidth and Video Bandwidth of 300 Hz.

larger pulse energy, and with the high gain also allows of shorter time for pulse build-up. After the event, the following pulse will have lower pulse energy and longer pulse duration due to less gain available.

RFSA technique provides an accurate and easy measurement method to extract information on the pulse amplitude and width fluctuations and timing jitter where they occurred simultaneously in the laser resonator. Fig. 4.12 shows a RF spectrum obtained by replacing the OSC with the RFSA through SMA to SMA connection with the same PD. The RFSA was set at a span of 25 kHz, with resolution and video bandwidth of 300 Hz. The spectrum analysis is performed at the first harmonic (fundamental pulse repetition rate= 21.8 kHz) at the pump power of 92mW and laser wavelength of 1556 nm. It is noted that, each harmonic consists the sum of a constant amplitude noise spectrum, which is due to the pulse energy fluctuations and a component from pulse width fluctuations and timing jitter (Moghaddam et al., 2011).

In order to determine the pulse energy fluctuation, analysis can be done at the first harmonic as described by Von der Linde (1986),

$$\frac{\Delta E}{E} = \left[\left(\frac{P_c}{P_a} \right) \cdot \left(\frac{\Delta f_a}{\Delta f_{res}} \right) \right]^{\frac{1}{2}} \quad (4.3.1)$$

where P_c and P_a are the maximum power of the noise band (at the pedestal from the peak) and signal at the first harmonic respectively as shown in Figure 4.12 but measured in Watt rather than dB. While, Δf_a and Δf_{res} is the FWHM of the noise band and spectral resolution of the RFSA respectively. It is noted that, all the power values represent integrals of the power densities over the spectral frequency resolution Δf_{res} of RFSA. Moreover, the ratio of P_c/P_a from equation (4.3.5) represents a sum of two different components: 1) narrow noise band due to fast timing jitter and 2) constant noise band with power level of P_c due to amplitude fluctuations.

From the RF spectrum, the value components of $|10 \log (P_c/P_a)|$ is about 31 dB and $(\Delta f_a/\Delta f_{res})$ is about 4.8. From these values and equation (4.3.1), the calculated energy fluctuation obtained is about 0.0617 or 6.17 %, confirming amplitude fluctuations stability of the Q-switched laser. As mentioned previously, the pulse amplitude has some correlation with the pulse width, thus we can also conclude that the pulse width fluctuations is also stable. The inset shows RF harmonics from the 1st up to 13th at the same laser condition. The harmonics with the fundamental mode at 21.8 kHz and subsequent modes occurring at iterations of 21.8 kHz further prove the successful formation of a clean pulse train in time domain perspective, where the higher harmonics indicates that the pulse has a fast rise and fall time. It is noted that, the timing jitter analysis is not performed due its well known for having high timing jitter property found in passively Q-switched laser system as compared to actively Q-switched and mode-locked laser systems.

4.4 Summary

A film form of GO provides the flexibility and ease of integration with fiber laser resonator. The Q-switched fiber laser has been successfully generated using a very short length of Bi-EDF (21 cm) as a gain medium and GOSA film as the saturable absorber. The Q-switched laser also demonstrated its tunability using TBF having an average laser power of -16.8 dBm at 92 mW of pump power. At 65 mW of pump power, the Q-switched threshold is observed and the average output power is found to be increased from 0.03 mW to 0.11 mW as the pump power is raised from 65 to 118 mW. At the pump power of 118 mW, the Q-switched laser pulse energy is approximately 4.3 nJ, with a pulse width and repetition rate of 7.7 μ s and 27.2 kHz respectively. At the maximum pump power, a single pulse peak power of 0.56 mW is obtained. RFSA shows a stable Q-switched laser at the pump power of 92 mW having a peak-to-noise pedestal ratio of about 31 dB at the fundamental frequency (21.8 kHz) with the

calculated energy fluctuation of about 6.17 %. Moreover, all the experimental data has been explained and supported by the rate equations, Q-switched threshold expression, and saturable absorber principles which have been presented in chapter 2. In addition, the Q-switched pulse shapes have also been characterised. The problems of the Q-switched laser such as the pulse width, average output power and slope efficiency have been addressed and the necessary solutions have been proposed for further optimization.

CHAPTER 5: DEVELOPMENT OF GRAPHENE OXIDE SATURABLE ABSORBER VIA OPTICAL DEPOSITION FOR 2 μm Q-SWITCHED FIBER LASER APPLICATION

5.1 Introduction

Small nanoparticle size such as carbon nanotube (CNT) and graphene suspended in fluid can be optically deposited effectively onto optical fiber to fabricate saturable absorbers (SAs) (Kashiwagi et al., 2009, Martinez et al., 2010). The method has been proven to be cost-efficient and effective alternatives for SA-fabrication as compared to more complex methods such as spraying, direct synthesis, and polymer composition (Set et al., 2004, Yamashita et al., 2004, Sakakibara et al., 2005, Nakazawa et al., 2006).

Specifically, the optical deposition provides high efficiency of carbon crystal utilization that can be concentrated on the optical fiber ferrule and without the requirement of physical handling to place the material on the ferrule facet. These advantages can make the optical deposition method as a better alternative as compared to the graphene oxide (GO) film fabrication method as demonstrated in chapter 3. The film has problems with its surface wrinkles and the required of physical handling during the preparation of the film piece that can cause material bending and increase its nonsaturable loss.

On the other hand, for effective and efficient optical deposition several parameters have to be considered such as the concentration level of the colloidal suspension, the colloidal dispersion and the optical power (Martinez et al., 2010). Material dispersion by Dimethylformamide (DMF) solvent, ultrasonification and centrifugation processes to obtain single or several layers of CNT and graphene have been demonstrated by Kashiwagi et al. (2009), Kashiwagi and Yamashita (2009) and Martinez et al. (2010).

In this chapter, by taking the advantage of the hydrophilic property of GO, the optical deposition steps can be reduced which simplifies the process; provide a cost-effective and non-toxic approach (Seabra et al., 2014) for SA fabrication. The optical deposition method that works based on the principles of thermophoresis and heat convection effects will be presented to evaluate the effectiveness and efficiency of the deposition method. Then, the deposited GO will be analysed using Raman spectrometer and a comparison study on the degree of defect will be made with the GO film. The theoretical principle related to Raman spectrum analysis which has been discussed in chapter 3 will be utilized in this chapter to make that comparison study. Finally, the GOSA by optical deposition will be incorporated in a thulium doped fiber laser (TDFL) via similar method as demonstrated in Chapter 4 to generate Q-switching pulse train operating at 2 μm wavelength region.

Previously, several SAs have already been demonstrated to operate at the 2 μm wavelength region, including, crystals such as Cr^{2+} : ZnSe (Tang et al., 2008), semiconductor saturable absorber mirror (SESAM) (Koskinen et al., 2009), single-wall carbon nanotubes (SWNTs) and graphene (Lu et al., 2013). SESAM are considered as expensive and complex-fabrication device for 2 μm q-switching. Moreover, for SWCNTs, the nanotube diameter or chirality needs to be tailored accordingly for obtaining saturable absorption in the desired wavelength.

The GOSA on the other hand has a complex electronic band structure as mentioned in chapter 3, where its bandgap varies depending on the ratio of carbon bonds to oxidation functional groups and their different arrangements (Yan et al., 2009). Thus, an experimental work is required to test the fabricated GOSA in generating Q-switched laser at the 2 μm region where it is desirable for variety of eye-safe applications such as laser range-finders, coherent Doppler wind light detection and ranging (LIDAR) and differential absorption LIDAR systems (Tang et al., 2012, Lu et al., 2013, Wang et al.,

2012, Jiang et al. 2013). The Q-switched fiber laser at 2 micron using graphene SA demonstrated by Lu et al. (2013), produced a minimum pulse width of 1.08 μs and maximum repetition rate of 128 kHz. His data will be used as a reference to validate the experimental data in this chapter.

5.2 Electric double layer of Graphene Oxide in water

In this section, a discussion on the GO electric double layer (EDL) will be presented to demonstrate how this can affect the dispersion of graphite oxide powder in water and the optical deposition efficiency for fabrication of SA. Figure 5.1 shows a GO sheet model to demonstrate the arrangement of the oxygen functional groups attached to the sheet which will lead to the discussion. Generally, the oxygen functional groups are mainly populated at the top and bottom of the GO basal plane by the epoxy and hydroxyl groups; while on the other hand; smaller amounts of carboxyl and carbonyl groups are populated at the edges.

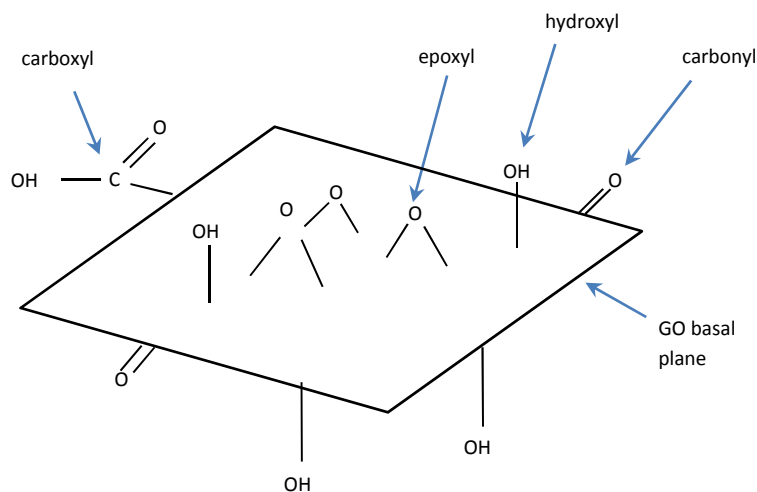


Figure 5.1: Simplified model of a graphene oxide basal plane with oxygen functional groups.

The functional groups of GO are uniformly but randomly bonded with the sp^3 carbon atoms in the basal plane through σ bond which disrupt the crystalline structure (He et al., 1998). When graphite oxide is dispersed in water to form many GO sheets, the water molecules undergoes ionic dissociation with the functional groups and create hydrogen bonds between the molecules. In addition, the water molecules also undergo ionic adsorption with the sp^2 aromatic domain; in which both processes mentioned produce surface charged on the GO basal plane and at its edges. While the sp^2 aromatic domain, carbonyl and epoxy groups have weak positive charges; the carboxyl and hydroxyl groups are negatively charged which makes GO to have an effective negative surface charge (Szabó et al., 2006).

Figure 5.2 shows the formation of EDL close to GO surface when the GO is dispersed in water medium; where its surface charged attracts counter ions against thermal diffusion. The surface charge is offset by an equal and opposite net charge of ions in the water.

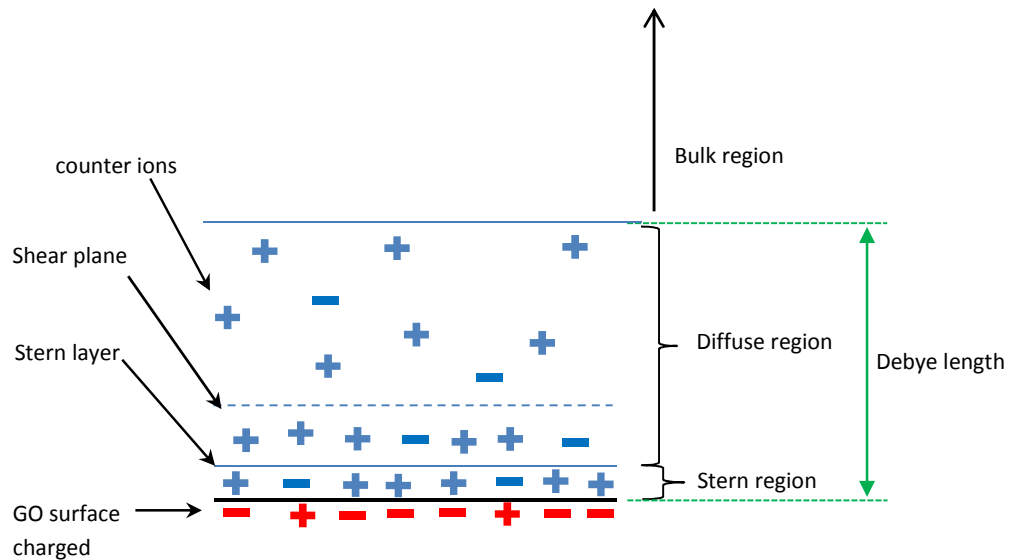


Figure 5.2: Electric double layer of GO in water.

These counter ions are consists of dissociated and adsorbed ions from the water and the GO surface and the adsorbed ions from the neighbour water molecules. The EDL with its effective thickness quantified as Debye length, λ_D is consists of Stern and diffuse regions (Hansen & Lowen, 2000). It is noted that, the Debye length is inverse proportional related to the colloid ionic strength and with the increased of the strength leads to the decrease in the thickness of the EDL (Jiang et al., 2009). In the Stern region, the counter ions are fixed and tightly bounded to the GO surface within the Stern layer; while, the diffuse region is where the counter ions are distributed in rapid thermal motion (Schießl et al., 2012). A boundary that separates between the dispersion of the counter ions and the fixed layer of counter ions that are strongly attached to the GO surface is called the shear plane.

In most cases, graphite oxide can easily dissolve in water and obtain a stable GO colloidal dispersion. This is due the electrostatic repulsion (ER) that occurred from the interaction between the EDLs (Bai et al., 2010). The interaction involves their diffuse double layers to be overlapped and the ions rearranged which gives rise to the ER. This ER and the oppose force of the van der Waals are co-exists between all the GO particles in the water. When the ER is dominant, the colloidal particles remain dispersed and mobile in the water; where the magnitude of the ER force is influenced by both the ionic strength of the colloid and the surface potential which is mainly contributed by the negative charged of carboxyl and hydroxyl groups. On the other hand, at large particle separations, there is no EDL interaction due to the surface charge on the GO particles is screened by the neutralising counter ions that envelops them.

5.3 Fabrication of Graphene Oxide Saturable Absorber via Optical Deposition

In this work, in order to form the GO-based SA, the graphite oxide nanopowder is mixed with 20 ml of distilled water inside a 50 ml beaker producing a particle to water volume ratio of $1:5.24 \times 10^{10}$. The low concentration of GO particles is used to obtain low colloid ionic strength, which can provide thicker EDL, stronger ER and thus reduces particle agglomeration in the aqueous suspension. This increases the efficiency of the optical deposition due to lesser inter-particle interaction. Fig. 5.3 shows the graphite oxide nanopowder, which was obtained from Research Ltd. It has been

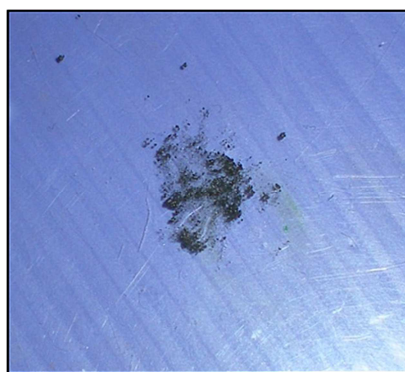


Figure 5.3: An image of graphite oxide nanopowder.

Table 5.1: Graphite oxide nanopowder specifications.

Particle diameter	90nm, +/- 15nm
Graphene oxide thickness	about 1 nm
Single Layer Ratio	>99%
Purity	>99%

prepared to have small lateral flake size with an average particle size of ~90nm and the specifications of the powder is shown in table 5.1. The dried unexfoliated graphite oxide powder form can be typically yield by lyophilising graphene oxide colloidal suspension

to remove the large content of water molecules. However, little information is known of how specifically the graphite oxide colloid is produced.

A FC/PC single mode fiber (SMF-28) patch cord obtained from Huber Suhner is used as a GO layer depositor. The optical deposition process is commenced by

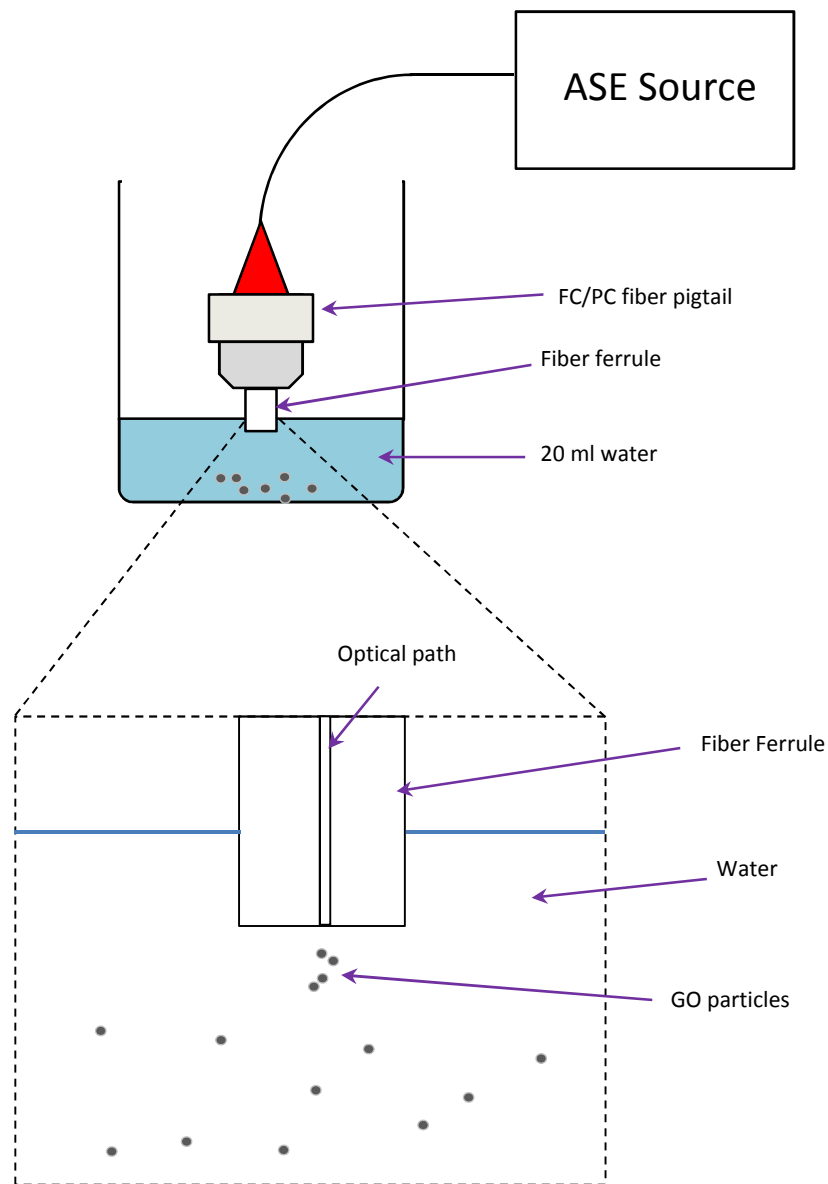


Figure 5.4: Optical deposition process for depositing GO layers on a fiber ferrule face.

immersing one end of a FC/PC fiber patch cord inside the prepared GO colloid solution as shown in Fig. 5.4. An amplified spontaneous emission (ASE) source operating at the C-band wavelength with an average output power of 15 dBm is emitted to commence the optical deposition. The transmission ASE power at the fiber ferule to water interface can be calculated using following equation,

$$T = \frac{4n_t n_i}{(n_t + n_i)^2} \quad (5.1)$$

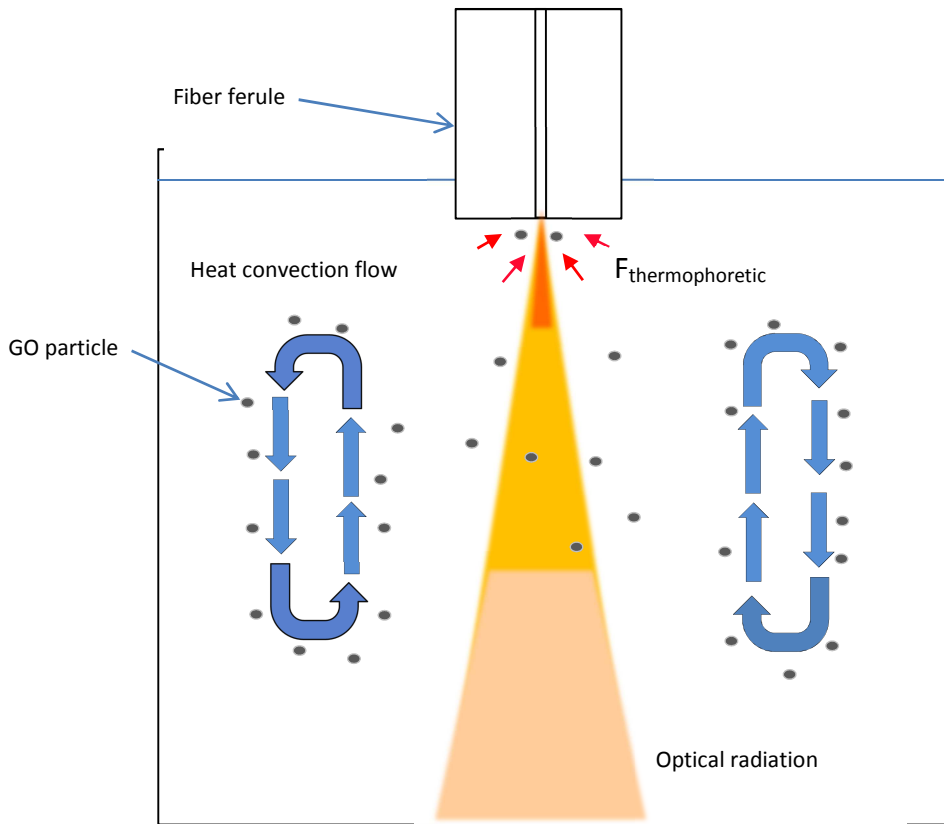


Figure 5.5: Optical deposition mechanism which includes the heat convection and thermophoresis effects.

where n_i is the refractive index of the silica glass, n_t is the refractive index of the water. The refractive index for silica glass is 1.44, while the refractive index of water is 1.33, giving the ASE light transmission of about 99.8%. The smaller refractive index of water

as compared to refractive index of the DMF ($n=1.43$), enable the optical radiation to penetrate in the water with lesser power loss at the fiber terminal and water interface.

The ASE power was radiated for about half an hour where optical intensity and temperature gradients are produced in the colloidal suspension caused by the light absorption from the GO and water particles. As a result of the intensity and thermal gradients, the GO layers are drifted close to the fiber ferule facet by mechanical and thermal force fields and adhere on the facet via van der Waals attraction force. Figure 5.5 shows the optical deposition process with the the related force fields generated by the thermophoresis and heat convection effects (Nicholson et al., 2007). It is noted that, for optical trapping, the optical gradient force is considered small and cannot overcome the scattering force due to divergence of light radiation from the SMF; thus, the process will not be discussed in this research work.

On the other hand, the temperature gradient that occurred in the water medium induces thermophoresis effect to occur (Piazza, 2008, Tao et al., 2005). In general, nanoparticle drift velocity caused by the thermophoretic force, can be described as in equation (5.2) (Würger, 2009).

$$v_t = -D_T \nabla T \quad (5.2)$$

$$D_T = S_T D \quad (5.3)$$

where D_T is the thermophoretic mobility and ∇T represent the temperature gradient. Equation (5.6) expressed the thermophoretic mobility as a function of Sorret coefficient, S_T and diffusion coefficient, D ; and it is specifically depends on the condition of the colloidal suspension. Basically, the thermophoretic mobility is caused by the forces from the particle on the surrounding fluid with the dissipative stress due to the temperature gradient. For neutral charged colloid such as found in graphene or CNT in

DMF solution; the thermophoretic mobility is mainly contribute by the van der Waals force that occurred at the interface between the particle and the fluid (Würger, 2009, Fu & Gao, 2012). In contrast, for a charged GO colloid, the thermophoretic mobility is contributed by the EDL and the van der Waals force. Furthermore, GO has low conductivity which leads to having low permittivity parameters. As a result, the GO material is difficult to be polarised as compared to graphene and CNT (Zhang et al., 2011) with having higher dielectric permittivity values. The counter ions in the GO EDL which do not have the sufficient time to follow the alternations in the direction of the light electric field also ceases to polarise. Therefore, the electric field from the optical radiation has no direct effect in changing the EDL thickness and the surface potential of GO. By considering the conditions above and assuming the colloid system is weakly charged, with Debye length < particle size; equations (5.4-5.7) presented by Würger (2008) can be used specifically to approximate and describe the thermophoretic mobility of GO particle in the water,

$$D_T = \kappa \frac{k_B}{12\pi\eta l_B} \hat{C}_v \quad (5.4)$$

$$\kappa = \frac{3\kappa_s}{(2\kappa_s + \kappa_p)} \quad (5.5)$$

$$\hat{C}_v = \hat{\xi}^2 + 8(\alpha + \tau - 3) \ln \cosh\left(\frac{\hat{\xi}}{4}\right) - 3\hat{\xi} \delta\alpha \quad (5.6)$$

$$\hat{\xi} = 2arsinh(2\pi\sigma_0 l_B \lambda_D) \quad (5.7)$$

κ : thermal conductivity ratio of solvent and particle

κ_s : thermal conductivity of solvent

κ_p : thermal conductivity of particle

k_B : Boltzman constant

η : viscosity of solvent

l_B : Bjerrum length

ξ : reduced zeta potential

τ : variations of dielectric constant with temperature

α : Soret coefficient

$\delta\alpha$: Seebeck coefficient

σ_0 : particle charge density

λ_D : Debye length

It is noted that, the D_T sign (positive or negative) determines whether the particle move from hot to cold region or otherwise. The sign is determined by the thermal response of the colloidal suspension, which is quantified by the Soret coefficient, α or the product of Seebeck coefficient with reduced surface potential, $\delta\alpha \zeta$ (Würger, 2008). When the coefficient D_T is positive, a temperature gradient drives the suspended particles towards colder region namely the fiber ferule facet due to having higher thermal conductivity than water. The fiber ferule is made up of zirconia ceramic and silica glass materials with their thermal conductivities are 2.5-3 W/mK and 1.3-1.5 W/mK respectively; while the water thermal conductivity is about 598.4×10^{-3} W/mK which explains the direction of the particle motion. An inverse effect ($D_T < 0$) occurs for a sufficiently negative Soret coefficient α or if the product $\delta\alpha \zeta$ takes a positive value. It is noted that, the thermophoretic mobility of charged colloid in aqueous solution is positive and

has smaller magnitude by a high degree as compared to uncharged systems in the non-polar organic solvent (Würger, 2009). In addition, the van der Waals force is small and rather insignificant which would provide greater impact on the thermophoretic mobility as demonstrated for the uncharged system. It is noted that, the sign of D_T for the GO colloid is difficult to determine from the Soret coefficient, since the related data is unknown in literature. Therefore, an experimental work is required to obtain the necessary data to compute accurately the coefficient and ultimately to obtain the D_T value.

The second mechanism for the optical deposition is based on the heat convection flow caused by the local heating of the colloid by the light radiation. According to Buongiorno (2006), nanoparticles can homogenously be in motion with the fluid due to the fluid density changes caused by external heating. The less dense water molecules (at hotter region) will move vertically at higher region of the water level due to Buoyancy force, while the denser (at colder region) water molecules will move vertically to lower region of the water level (Mills, 1999, Bird et al., 2007, Gebhart et al., 1988). As the fluid rises, it will start to lose its heat due to the heat transfer effect occurred at the top water level. In consequence, a cyclic fluid flow pattern is produced as shown in Figure 5.5. The fluid motion can be approximated and described in terms of fluid velocity as followed,

$$v \approx \sqrt{\left(\frac{\Delta\rho}{\rho} Lg\right)} \quad (5.8)$$

$$\Delta\rho = -\Delta T \left(\frac{\delta\rho}{\delta T}\right) \quad (5.9)$$

where $\Delta\rho$ is the density difference between low dense fluid and high dense fluid, ρ is fluid density, g is the magnitude of acceleration, and L is the vertical distance. Equation

(5.9) dictates that the fluid density difference is proportionally related to temperature rate of decrement of fluid density times the temperature difference between at the low and high fluid density regions. In order to enhance the fluid motion, the nanofluid needs to be heated up effectively so that its density can be reduced for vertical fluid motion to take place. This can be accomplished, by having sufficient optical power and with the use of small GO particle volume fraction. The low particle concentration can significantly reduce the nanofluid viscosity and thus enhances the nanofluid motion owing to the reduced of interparticle effect and particle/fluid interaction (Gerber, 1984). Moreover, the low particle concentration also allows for the nanofluid to gain higher temperature due to the lower heat transfer rate of the nanoparticles.

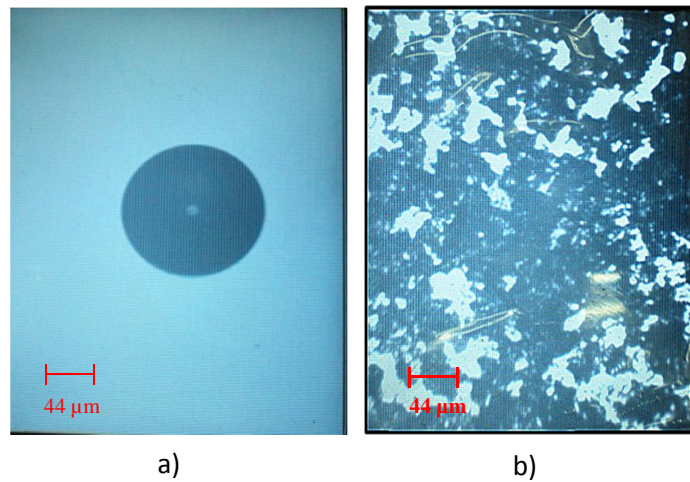


Figure 5.6: The optical fiber scope image of the GO-SA on a fiber ferrule face before (left) and after (right) optical deposition process. The dark areas are the GO layers, while the bright areas are the parts of the fiber ferrule not covered by the GO particles (Field of view = $400\ \mu\text{m} \times 300\ \mu\text{m}$, Resolution $<1\ \mu\text{m}$).

After the optical deposition is complete, the fiber ferrule is removed from the beaker and then left to dry for another half an hour before making an inspection using optical fiber scope. The scope provides a magnification of x400 and has a field of view of $400\ \mu\text{m} \times 300\ \mu\text{m}$ with a resolution of $<1\ \mu\text{m}$. It is capable to determine whether the GO

layers have been deposited successfully on the core at the fiber ferule face. Figure 5.6 a) shows the image of the fiber ferule face without GO layers at the cladding and the core regions. The white outer background is the fiber ferule component made of zirconia ceramic, the circular dark area is the cladding region (125 μm), while a non-dark spot at the center is the core region (9 μm) of the fiber. In contrast, figure 5.6 b) shows a similar scope of view but with the ferule face covered with GO layers that are intercalated with the remaining water molecules via hydrogen bonds. It is important that the GO layers must cover the core region (optical path) for Q-switching to occur effectively when the SA is employed in the cavity.

In this research work, the optimization for the optical deposition is not covered which includes the layer-thickness control by reducing the period of optical deposition and using the reflectrometry technique that has been demonstrated by Kashiwagi et al. (2009). However, we have successfully deposited GO particles on the fiber ferule without the need of toxic chemical solvent, ultrasonification and centrifugation as required by graphene and CNT using the DMF solvent. This is due to the hydrophilic property of GO as discussed, which allows bulk layers to disperse in water effectively. Nevertheless, an experimental work is still needed to determine the D_T sign which can degrade or contribute the optical deposition efficiency. Therefore, deeper analysis is required in order to optimize the optical deposition process for the negatively charged GO colloid. Nevertheless, the proposed optical deposition method provides simpler, cost-effective, and non-toxic approach for SA-fabrication which is attractive and valuable in the photonics, biotechnology and material engineering fields.

5.4 Characterization of GOSA and comparison study

The deposited GO layers are analysed by Raman spectroscopy technique using the Renishaw Raman Spectrometer to confirm the presence of GO material deposited on the ferule facet. The obtained spectrum is shown in Fig. 5.7. with two main peaks (D and G

peaks) with Raman shifts of 1358 cm^{-1} and 1587 cm^{-1} are obtained respectively. In addition, the I_D/I_G value is measured to be 0.92, confirming the presence of GO on the fiber ferrule (Sobon et al., 2012, Stankovich et al., 2007). As we discuss in chapter 3, section 3.5, the I_D/I_G ratio is fairly an accurate measurement of disordered in the GO sheet regardless of the material thickness.

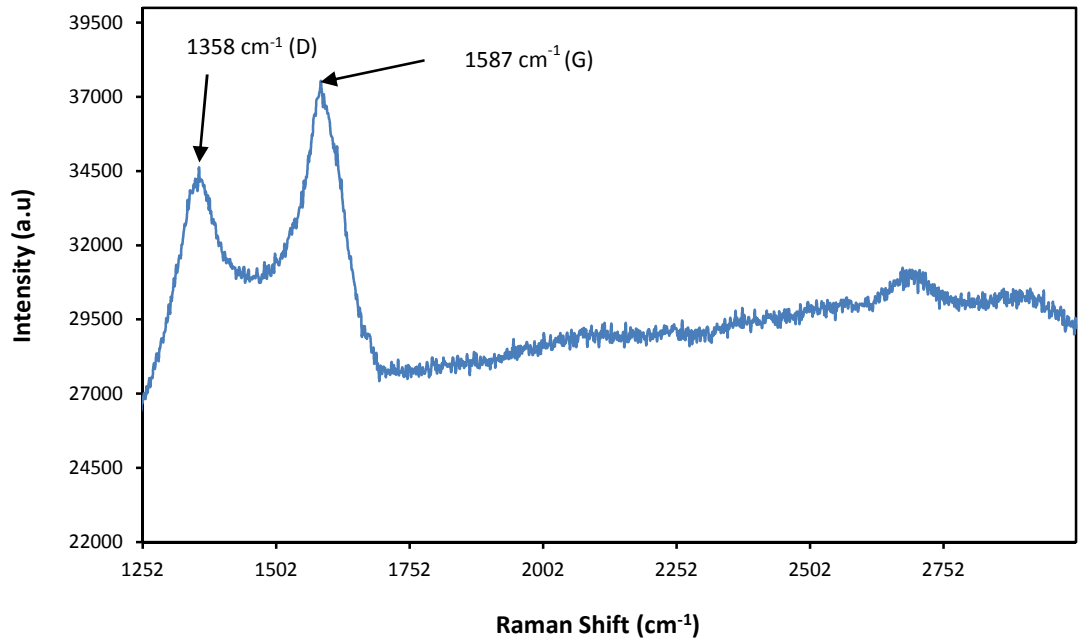


Figure 5.7: Raman spectrum of the optically deposited Graphene Oxide on the fiber ferrule facet.

This allow us to make a comparison estimation on the degree of defect between the GOSA by optically deposited and GOSA film produced in chapter 3, which is important in order to predict the saturable absorption in the material. However, we didn't stress on other methods such as the analysis on the G and D peaks positions due to their shortcoming in terms of accuracy. As the followings we will summarise and extend the characteristic for G and D peaks parameters and their dynamics to highlight their

weaknesses and in doing so, we are able to analyse the relative characteristic of the GO structure for high defect carbon material.

- 1) As defect is presence in the carbon lattice, this will increase the bond-angle disorder in the sp^2 carbon atoms or in the same manner increasing the sp^3 content. In addition, the increased in the disruption of the double bonds which in turn will weaken the bond and soften the E_{2g} vibrational mode, giving the G peak position shift to lower frequency.
- 2) As the material thickness layer increases, the G position also shift to lower frequency until which there is little change in the G position for thicker layers (Gupta et al., 2006).
- 3) On the other hand, as defect level increases, the G peak intensity will be reduced insignificantly or simply remained unchanged compared to the D peak. This is due to that the intensity depends only on the amount of stretching of sp^2 carbon pairs but not the aromatic cluster stretching as found for the D peak.

Therefore it is difficult to judge the amount of change in the G peak parameter in relative to the degree of defect. On the other hand, the D peak characteristic is as followed:

- 1) Decrease in number of ordered aromatic rings will shift the D peak to lower frequency and reduces its intensity.
- 2) Smaller aromatic cluster size produce higher modes, which will shift the D peak frequency upwards.
- 3) As the thickness layer increases, the D peak intensity will be increased and eventually decreased for thicker layers (Yang et al., 2013) due to the lack of laser penetration depth. The increased of D intensity is owing to the increased

in the number of aromatic rings and which also has an effect on the D peak position; where the D peak frequency depends on the number of the rings and the size of the aromatic cluster.

For this case, as the defect level increases, the first two factors above become more apparent. However, the degree of frequency shift for each case is unknown. In addition with the thickness variable, the D peak is far more complicated to predict due to its non-linear response to the parameters mentioned. For that matter, the intensity ratio value (I_D/I_G) value is the best option to make the comparison estimation on the degree of defect between the GOSA by optically deposited and GOSA film. It is noted that, the spectral measurement are performed under the same laser excitation wavelength (532 nm) and laser power of 5 mW in order to accurately perform the analysis mentioned. From the spectra, the intensity ratio (I_D/I_G) value of GOSA by optical deposition is $0.92 > 0.86$ (GOSA film) suggests that the GOSA film has smaller effective aromatic cluster size. The relationship between the I_D/I_G ratio value and the effective aromatic domain size has been expressed in equation (3.4), presented in chapter 3. From this analysis, we can conclude that the GOSA by optical deposition has higher capacity for saturable absorption due to having larger aromatic domain size.

5.5 Q-switched pulse train generation operating in 2 μm region using the developed GOSA

5.5.1 Experimental arrangement

After the Raman spectrum measurement, the fiber patchcord with the deposited GO layers is connected to another fiber patch cord using an FC/PC adaptor to complete the assembly of the SA. This method is similar as described in section 4.2 of chapter 4. The SA is then incorporated into a thulium doped fiber laser (TDFL) cavity for Q-switching

application. Fig. 5.8 shows the experimental setup of the proposed Q-switched TDFL, which consists of a 2 m long single-mode Tm^{3+} -doped silica fiber (TDF) from Nufern,

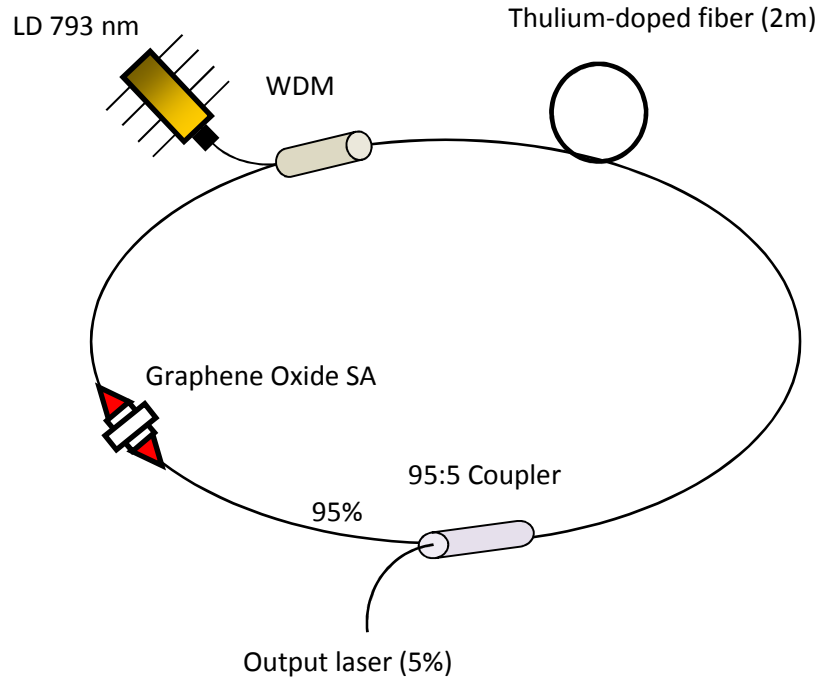


Figure 5.8: Setup of the proposed Q-switched TDFL with GO-based SA.

Table 5.2: Thulium-doped single mode fiber specifications.

Operating Wavelength	1900 – 2100 nm
Core NA	0.15
Mode Field Diameter (predicted)	10.5 μm @ 2000 nm (nominal)
Cutoff	1750 \pm 100 nm
Core Absorption	9.00 \pm 2.00 dB/m at 1180 nm 27.00 dB/m at 793 nm

USA. The TDF has core absorption of 27.0 dB/m at 793 nm, a cutoff wavelength of 1750 nm, core diameter of 9 μm and cladding diameter of 125 μm . The specification of the fiber is summarized in table 5.2. The TDF is core-pumped by a single mode Lumics 793M200 laser diode (LD) operating at 793 nm with a maximum output power of 164 mW. The LD pumps the TDF through an 800/2000 nm fused wavelength division multiplexer (WDM), with the LD connected to the 800 nm port. The common port of the WDM is connected to one end of the TDF, while the other end of the TDF is connected to an AC Photonics Inc. 95:5 tap coupler. It must be noted that the tap coupler is designed for use in the 1550 nm region, and this may result in slight losses to the system, although not to the extent that the performance of the system will be severely affected. The 95% port of the tap coupler is connected to the GO-based SA assembly, with the other end of the assembly is connected to the 2000 nm port of the WDM. The 5% port of the tap coupler is used to extract a small portion of the oscillating signal for measurement.

Laser and amplified spontaneous emission (ASE) at the 2 μm region is measured using Yokogawa AQ6375 optical spectrum analyser (OSA) that can detect light wavelength up to 2400 μm for spectrum analysis. Moreover, EOT Inc. ET-5010F Indium-Gallium-Arsenide (InGaAs) photodetector (PD) with a bandwidth of >12.5 GHz that can detect wavelength range from 1475 nm to 2100 nm is used to convert the light energy into electrical signal. The PD is mounted on the LeCroy oscilloscope (OSC) with a bandwidth of 500 MHz to measure and display the pulse pattern. Furthermore, Melles Griot 13PEM001 broadband power meter (PM) is used to measure the optical power of the laser light at 2 μm region. In addition, an Anritsu MS2683A radio frequency spectrum analyser (RFSA) is used to measure laser pulse stability.

5.5.2 Performance of the Q-switched laser

The TDF provides a broad emission spectrum at 1900 nm region via the $F_4^3 - H_6^3$ transition. Fig. 5.9 shows the ASE spectrum of the TDF, which was obtained when the fiber is pumped by 128.8 mW of 793 nm pump. It can be seen that the spectrum is stretched from 1760.0 nm to approximately 2118.0 nm, giving a spectral bandwidth of about 358 nm with a peak power of 52 dBm at approximately 1890 nm. The ASE oscillates in a ring cavity to generate laser which the output is tapped out from 5% port coupler and measured using the OSA with a span setting of 515 nm and a resolution of 0.2 nm. Fig. 5.10 shows the laser spectrum with and without the GOSA assembly incorporated in the laser resonator at the pump power of 128.8 mW. It is noted that the OSA was set at a resolution 0.2 nm and a span of 150 nm to make that measurement.

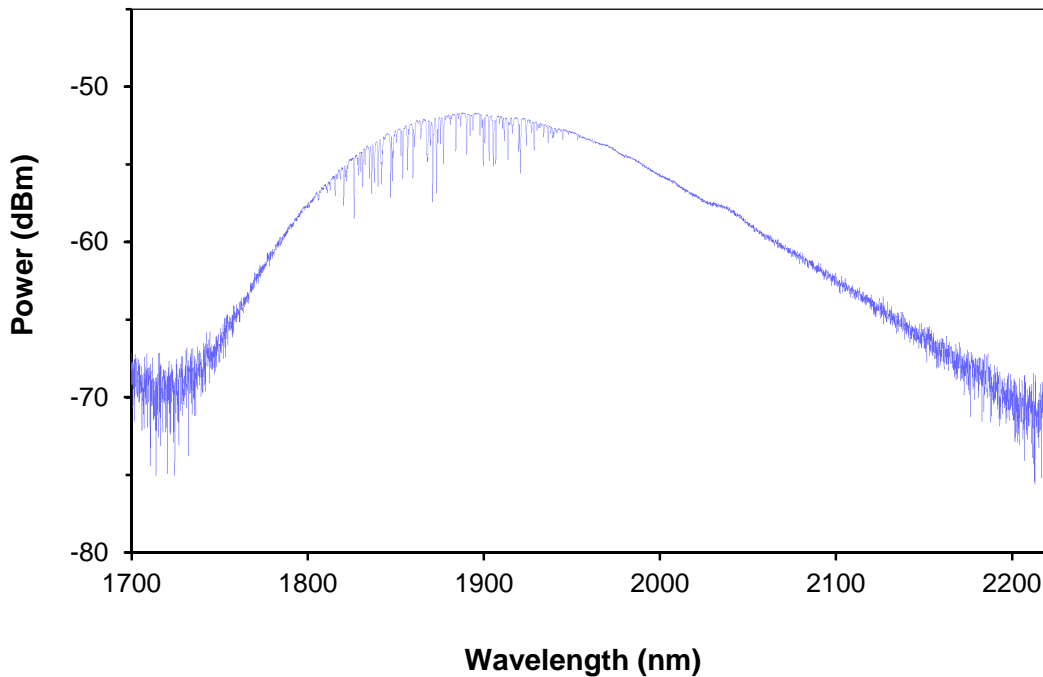


Figure 5.9: Thulium-doped fiber ASE spectrum pumped at 128.8 mW.

For the case without the GOSA assembly, a single continuous wave (CW) laser at a wavelength of 1945.0 nm is observed, with a peak power of about 2.6 dBm. The lasing wavelength is well defined, with a signal-to-noise ratio (SNR) of approximately 54 dB and a full width at half maximum (FWHM) bandwidth of 0.2 nm. Inserting the GOSA however changes the output of the TDFL, widening the bandwidth to approximately 1.0 nm due to the laser now operating in the Q-switching regime. It can be observed that the center wavelength of the Q-switched laser blue-shifts to 1941.7 nm relative to the CW laser wavelength. The shift is induced as a result of the loss incurred when the GOSA is integrated into the laser cavity, thereby forcing the system to compensate for these by

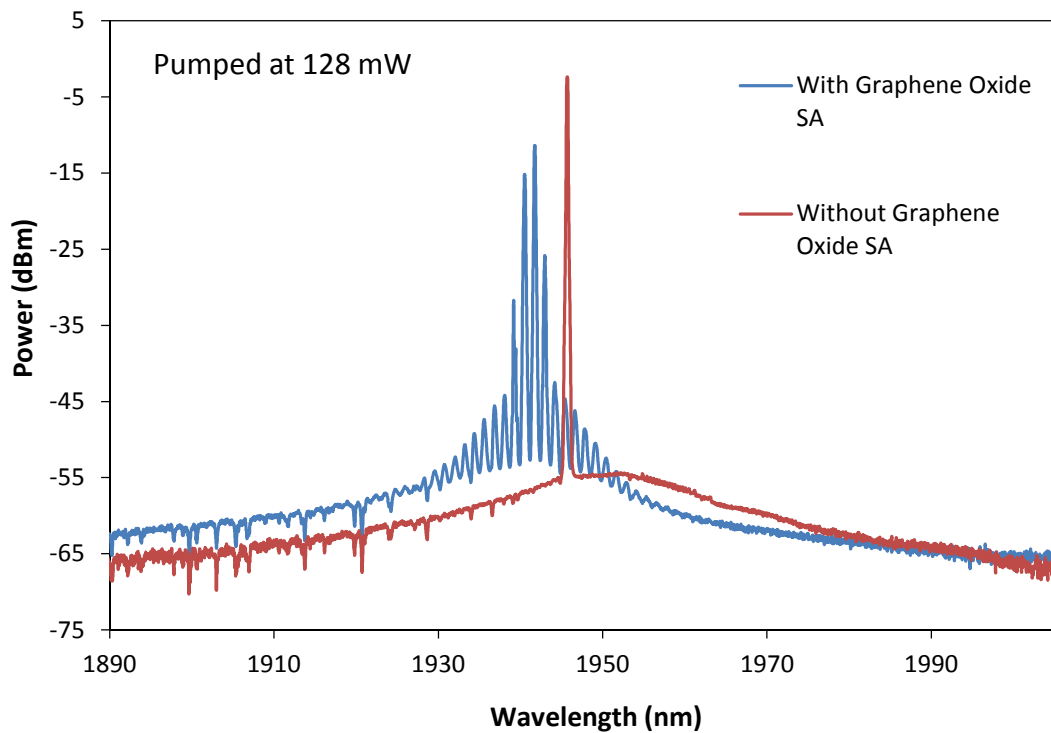


Figure 5.10: Thulium-doped fiber laser spectra with and without the GO based SA and a curve fit that envelopes the Q-switched laser spectrum for FWHM measurement. The inset shows the ASE spectrum of the TDF.

moving towards the region of higher net gain (Harun et al., 2012). The loss incurred also lowers the peak power of the system, with the lasing wavelength now having a lower peak power of only -12.0 dBm.

The GOSA also interferes with the buildup of the main lasing mode, where insufficient time for pre-lase signal to make strong mode selection and as a result give rise to multi-longitudinal mode oscillations (Cao et al., 2012, Dong & Ueda, 2005, Abraham et al., 1985). This is evident as shown in the figure with the irregular power spikes in the spectrum are formed. It is noted that, the Q-switched pulse builds up from the ASE noise as mentioned in chapter 2, with each pulse comprising a mixture of longitudinal modes that differs randomly from pulse to pulse. In consequence, the multimode oscillations are not fixed at their oscillation wavelengths, which make it rather unstable and unrealizable for multi-wavelength laser application. In comparison to the Q-switched laser spectrum in chapter 4 (figure 4.5), the multimode oscillations are not apparent due to the loss introduced by the tunable band pass filter (TBF), where other longitudinal modes are suppressed to allow for strong mode selection for single mode lasing. In addition, the laser setup utilize unidirectional light propagation scheme and has a relatively shorter resonator length, thus suppressing the spatial hole burning effect and multimode oscillations.

In order to analyse the Q-switched pulses generated by the TDFL, the OSA is removed from the setup, and replaced with the PD connected to OSC. Fig. 5.11 and 5.12 show the normalized single pulse and pulse train obtained from the TDFL under pump powers of 148 and 164 mW, respectively. The traces show that the pulse is better defined at the higher pump power, with the walls of the trace having better continuity and fewer jagged peaks. The pulse intensity standard deviation (ΔI) of $\pm 1.46\%$ and $\pm 1.25\%$ are obtained at the pump powers of 148 mW and 164 mW respectively. The

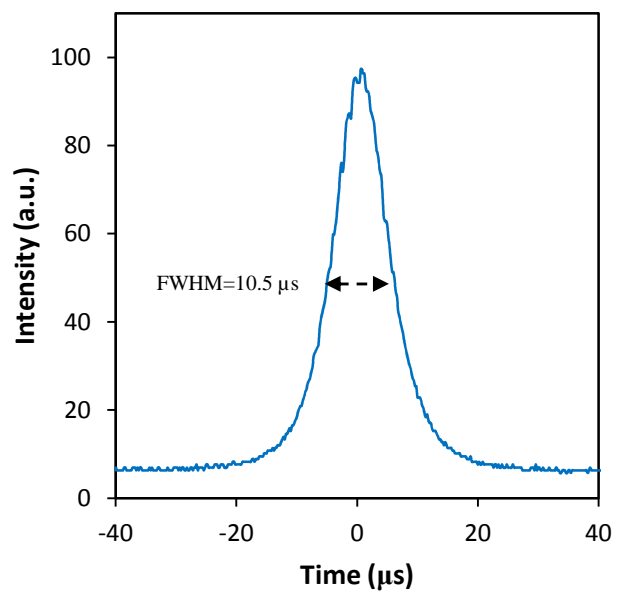
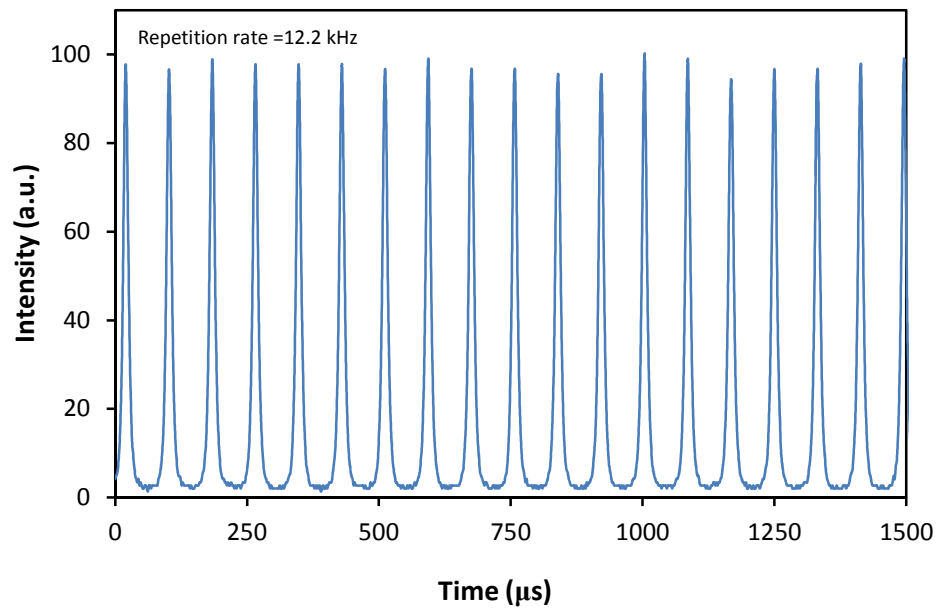


Figure 5.11: Single pulse and a pulse train of a Q-switched laser at a pump power of 148mW.

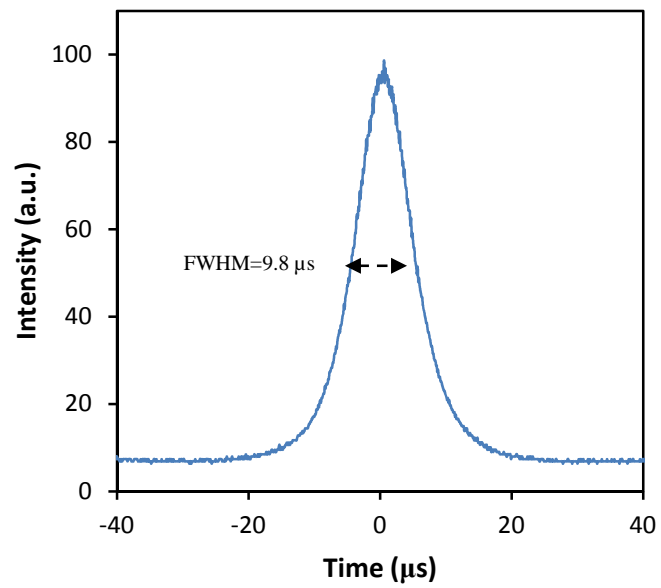
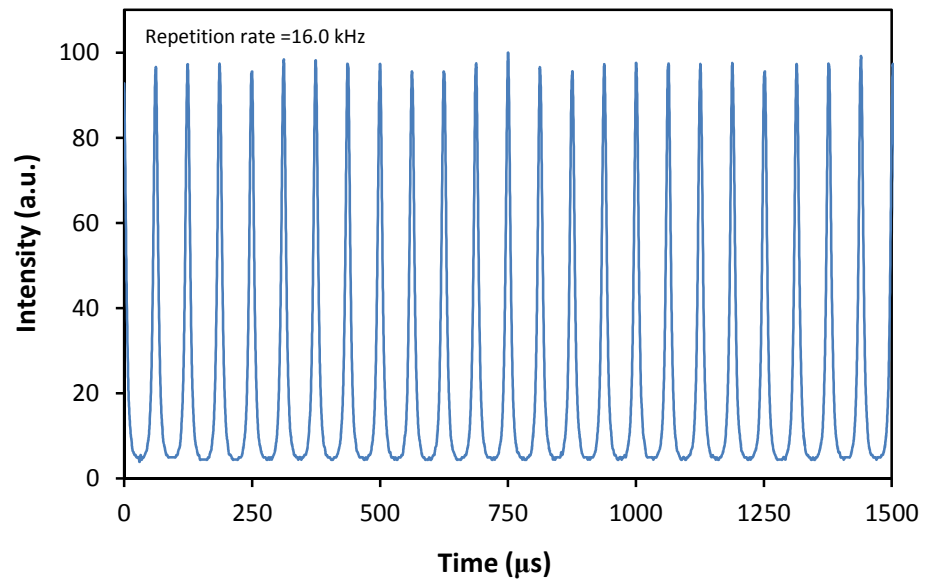


Figure 5.12: Single pulse and a pulse train of a Q-switched laser at a pump power of 164 mW.

same sample size is considered to calculate the statistical value with a ΔI decrement of 0.21% per the increment of 16 mW of pump power is obtained. These results show similar pattern as in the pulse trains found in chapter 4 (figure 4.6 and figure 4.7), and this is due to the laser has attained greater stability at higher gain.

The CW and Q-switched laser threshold of the proposed laser are about 100 mW and 125 mW, respectively. The higher laser threshold obtained as compared to the Bi-EDF fiber laser in chapter 4 is due to the low quantum efficiency of the Thulium fiber 3F_4 level. Fig. 5.13 shows the repetition rates and pulse widths of the output pulses as a function of pump power. The repetition rates of the pulse trains increases as the pump power is raised, from a repetition rate of 12.2 kHz at a pump power of 148 mW to a repetition rate of 16.0 kHz at a pump power of 164 mW. Moreover, the single pulse profile at a higher pump powers is better defined, as compared to the profile obtained at

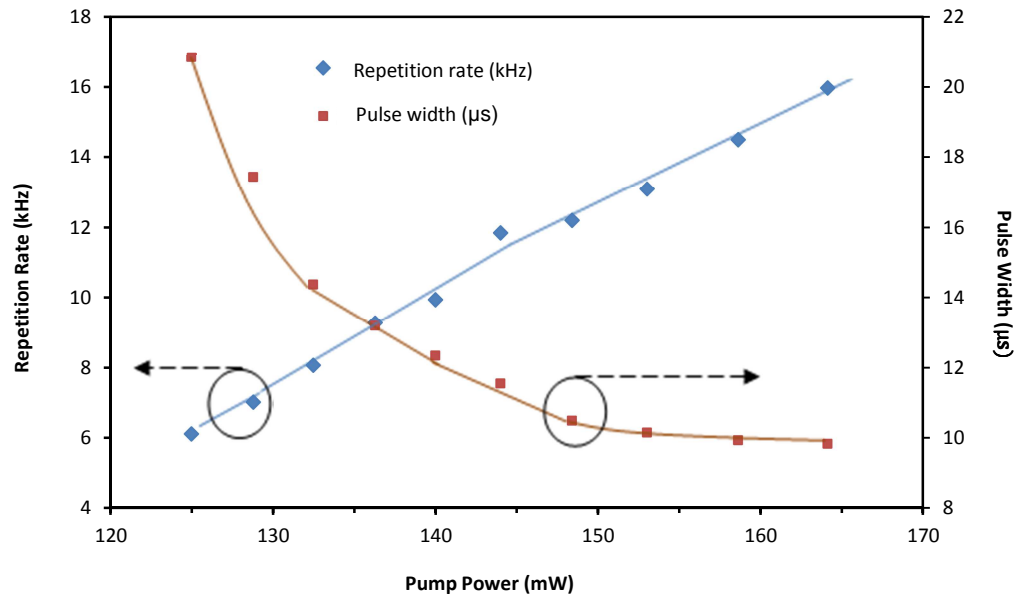


Figure 5.13: Repetition rate and pulse width curves as function of pump power.

lower pump powers with having some random high frequency noises riding on the pulse due to mode beating. The more apparent of jagged peaks of the pulses as compared to the ones in the chapter 4, are due to the dual light propagation directions in the resonator which caused instability in the laser generation owing to the mode competition effect.

Compared to Bi-EDF fiber laser, the response of the repetition rate is more linear with an initial slope of 0.3 kHz/mW until a 144 mW of pump power is reached; subsequently, the slope reduces slightly to 0.2 kHz/mW until the maximum pump power of 164 mW is reached. The more predictable linear curve indicates that the GOSA saturable absorption and nonsaturable loss remain unchanged in respect to the change of pump power as compared to the curve found in chapter 4 (Figure 4.8). The repetition rate will continue to increase linearly per the increase of the pump power until the GOSA has reached damage threshold. At this point, the GOSA saturable absorption property will change and alter the curve pattern and eventually damage the SA completely if the pump power is further increased. The Q-switched pulse width however, decreases as the pump power increases, from an initially steep slope of 0.86 s/mW, before becoming shallower at 0.24 s/mW above a pump power of 132.5 mW. When a pump power is increased above 148.4 mW, only a minor change in the pulse width is observed, with the slope at this region computed to be around 0.045 s/mW. The slower change in the pulse width at higher pump powers suggests that the GOSA is reaching saturation, and at the maximum pump power of 163 mW, a saturation pulse width of 9.8 μ s is obtained.

Fig. 5.14 shows the average output powers and pulse energies characteristics at different pump power. The average output power is measured by a PM which is placed at the 5% output port of the TDFL's cavity. As mentioned previously, the setup exhibit dual-light propagation scheme, this allows higher output power than the single light propagation scheme. It can be seen from Fig. 5.15 that the output pulses are typical in

behaviour to that of Q-switched pulses, with the average output power reaching a value of 0.3mW at a 164 mW maximum of pump power. Similar to the repetition rate, the

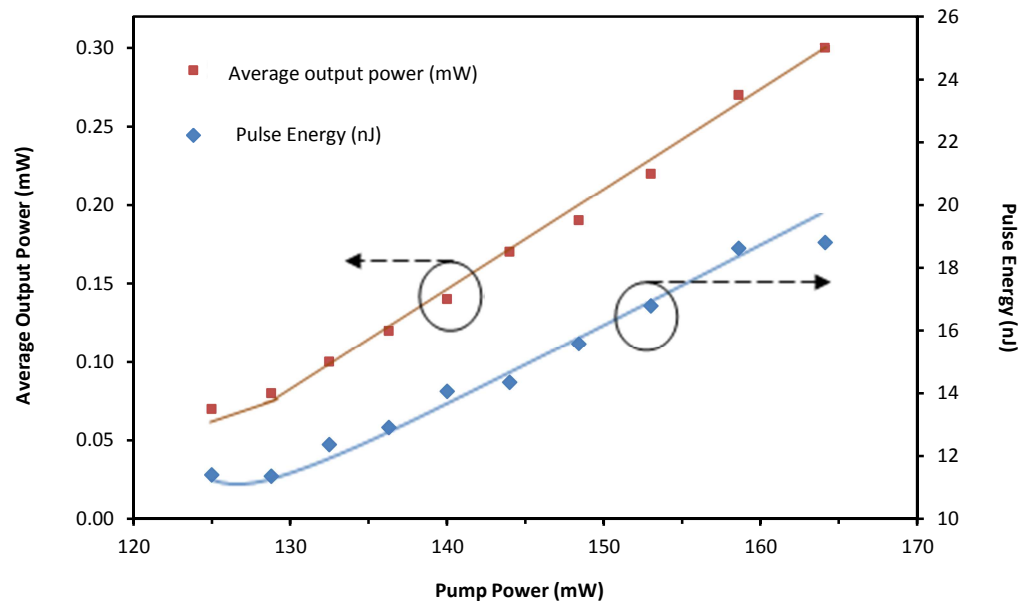


Figure 5.14: Average output power and pulse energy curves as function of pump power.

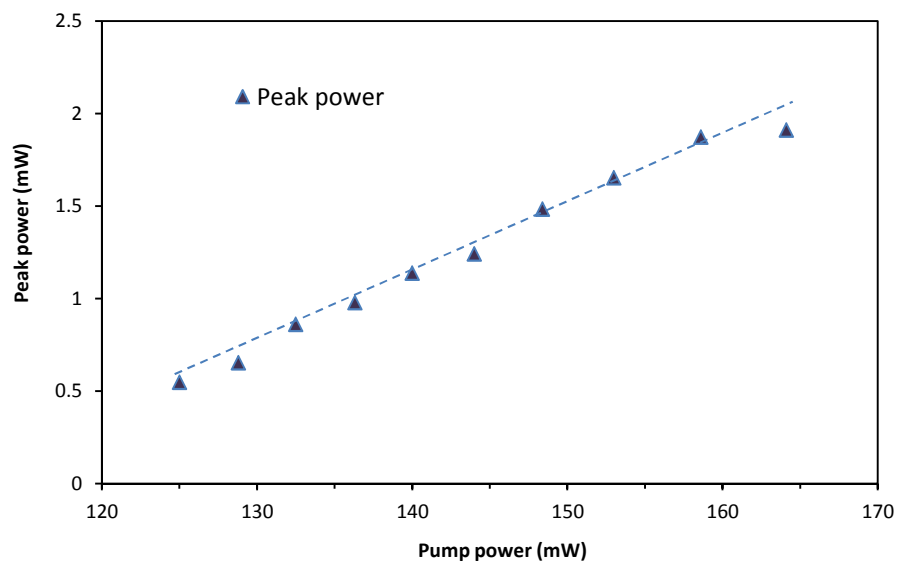


Figure 5.15: Peak power as function of pump power.

increment of the average output power is almost in linear manner with a slope efficiency of 0.63%, and only minor variations from the fitted line. Furthermore, the pulse energy also rises linearly with slight variations in the data points as compared to the average output power curve. There is an increase in pulse energy from 11.4 nJ at a pump power of around 125 mW, to 18.8 nJ at the maximum pump power of 164 mW, having an average slope of about 0.21 nJ/mW. On the other hand, Fig 5.15 shows the peak power of a single pulse at different pump powers having a consistent slope efficiency of 3.5%. At the Q-switched threshold, the peak power of 0.55 mW is obtained and the average output power increases linearly up to 1.91 mW at 125 mW of pump power.

The stability of the Q-switched pulse train is analysed by connecting RFSA together with the PD at the 5% output port of the TDFL. The obtained RFSA spectrum, at a resolution of 300 Hz along a 22 kHz span is shown in Fig. 5.16. It shows that the fundamental harmonic of the Q-switched laser pumped at 148 mW, occurring at a repetition rate of 12.2 kHz. The fundamental harmonic has a signal power of approximately 43.0 dBm, giving it a signal-to-noise ratio of about 28.0 dB. The peak-to-noise ratio is higher than the threshold value of 20.0 dB, thus indicating that the output pulses are stable (Tan et al., 2013). More specifically, if we take the equation (4.3.1) presented in section 4.3 of chapter 4, we can calculate the energy fluctuation accurately. From the spectrum, the component values of $|10 \log (P_c/P_a)|$ and $(\Delta f_a/\Delta f_{res})$ is about 28 dB and 4.7 respectively. Therefore, the calculated energy fluctuation $(\Delta E/E)$ is about 8.6% which is relatively higher than the value obtained from chapter 4 with a value of 6.17%. This suggests that the pulses are less stable which are also apparent based on the pulse pattern and pulse intensity standard deviations at both low and high pump powers. Therefore in overall, the generation of Q-switched pulse in this experiment has higher amplitude and pulse width fluctuations as compared to the pulses generated in chapter 4. This can be concluded that the dual light propagation directions

degrade the laser oscillation stability due to the mode competition occurred in the laser resonator. On the other hand, there is no indication of high frequency harmonics suppression, as indicated by the inset of Fig. 5.16 which shows the RF fundamental harmonic and up to the 12th harmonic. This indicates that the pulses have a short rise and fall time, and clean train of pulses have been generated.

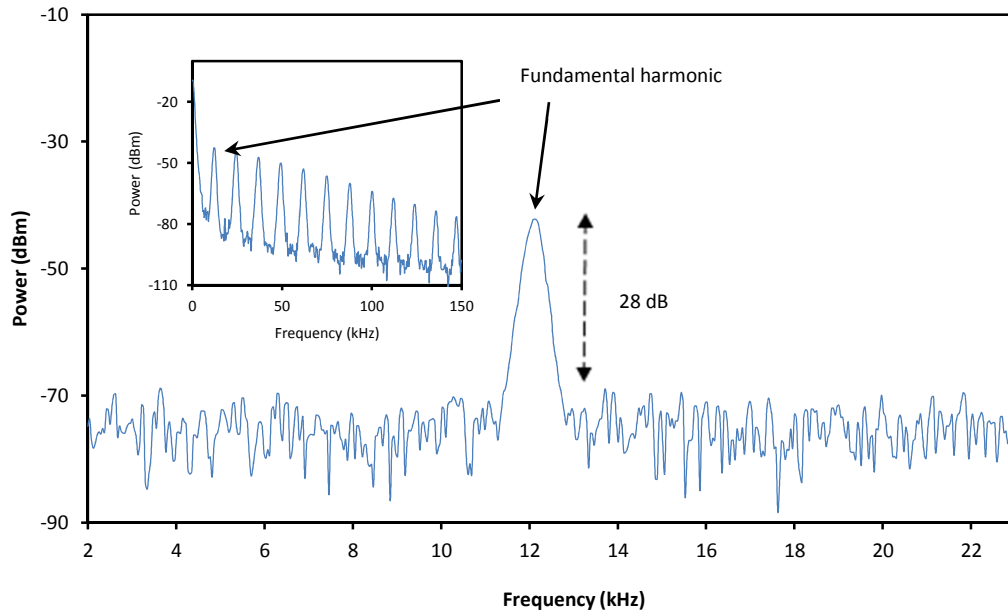


Figure 5.16: Radio frequency measurement of Q-switched laser at a repetition rate of 12.2 kHz using RFSA, with inset showing the RF harmonics of the laser pulses.

5.6 Summary

Graphene oxide has successfully deposited on a fiber ferule face via optical deposition method without the use of toxic chemical solvent and ultrasonification for particle dispersion as required by the graphene and CNT materials with DMF solution. This is accomplished by having graphite oxide nanopowder dispersed in a beaker contained water, and a fiber pigtail submerged in the beaker with ASE power is radiated in the water for heat convection and thermophoresis effects to take place. Optimization of the process was not conducted in the scope of work where the deposited layers can be

controlled as demonstrated by Kashiwagi et al. (2009). This can be accomplished by controlling the amount of optical power, duration of optical radiation, and using reflectrometry technique. Moreover, the thermophoretic mobility, D_T sign is still need to be determined through experimental work which can either contribute or degrade the optical deposition efficiency. After the optical deposition process, the optical fiber scope was used to observe the deposited GO layers on the ferule facet in order to ensure the success of the deposition on the fiber core which is critical for Q-switched laser generation.

Furthermore, Raman spectrometer was used to confirm the presence of GO material on the fiber ferule facet. The comparison study on the degree of defect between the GOSA by optical deposition and GOSA film under the same measurement condition was also conducted. The analysis shows that the I_D/I_G ratio value of GOSA optically deposited is $0.92 > 0.86$ (GOSA film) suggests that the GOSA film has higher disordered structure or density of defect. This proves that the GOSA by optical deposition has higher capacity for saturable absorption than the GOSA film. The GOSA by optical deposition also has been tested in a $2\text{ }\mu\text{m}$ thulium-doped fiber laser to generate Q-switched laser. The Q-switched fiber laser is capable of providing a pulsed laser output at the $2.0\text{ }\mu\text{m}$ region in a compact and easy to operate form factor; which is useful for the eye-safe applications such as in range-finding, sensing and many more.

CHAPTER 6: GRAPHENE OXIDE PAPER FOR THE GENERATION OF DUAL-WAVELENGTH Q-SWITCHED FIBER LASER

6.1 Introduction

Multi-wavelength fiber lasers have raised many research interests in recent years due to their demand for industrial applications. Recently, dual-wavelength fiber laser (DWFL) has shown many of its applications such as in differential-absorption-LIDAR (DIAL) (Sharma et al., 2004) measurement and generation of soliton pulse trains, microwave radiation (Dennis et al., 2007, Pradhan et al., 2006) and terahertz generation (Jeon et al., 2010). The generations of microwave and terahertz radiation are made possible by the optical beating process from the dual-wavelength fiber laser with having narrow wavelength spacing. Moreover, by Q-switching the laser system, one can enable the microwave and terahertz signals to operate in pulsed mode with having high pulse energy signals for a short time features. This will be useful in the microwave and terahertz fields that typically requires that specifications.

Recently, a graphene oxide paper (GO) paper, which has similar chemical characteristic of the previously developed GO (in Chapter 3 and 5), was also introduced for various possible applications. It exhibits high fracture strength and tensile modulus due to its well-aligned sheets and intercalated water structures (Medhekar et al., 2010). In fact, GO paper is superior to many other paperlike materials due to its stiffness and strength owing to the hydrogen bond network in the material (Gao et al., 2011). Also, due to its fabrication method, all the GO nanosheets in the paper are confirmed to be exfoliated; yielding dispersive single layer of GO sheets being aligned in the well-ordered structure.

Up to date, many works on all-fiber dual-wavelength fiber lasers have also been reported due to their potential applications in optical instrument testing, optical signal processing, fiber sensing systems and microwave photonics. For instance, a dual wavelength Q-switched fibre lasers was recently demonstrated by Luo et al. (2010) using graphene saturable absorber as a Q-switcher. In this chapter, a dual-wavelength Q-switched Erbium-doped fiber laser (EDFL) with a very narrow wavelength spacing of 33 pm is demonstrated by using a commercial GO paper as saturable absorber. It utilizes a tunable bandpass filter (TBF), a short length of photonics crystal fiber (PCF) and a PC in the ring cavity to produce the narrow spacing dual-wavelength laser. The characteristic of the GO paper is discussed and compared with the previous GO film in the following section.

6.2 Reviews on the Fabrication Method and Structure of GO Paper

Crystallite carbon based paper-like material was first demonstrated by the carbon nanotubes (CNT) material fabricated via flow-directed filtration process (Ng et al., 2005). The advance material structure has been served in many applications such as in fuel cell (Waje et al., 2005), structural composite (Coleman et al., 2003), electrochemical energy storage (Pushparaj et al., 2007), sensors and actuators (Yagoh et al., 2006, Baughman et al., 1999) and many more. Similar to CNT, graphene oxide layers can also be assembled in the same fabrication method. However, with the GO hydrophilic property, this allows GO paper based material to be produced at a larger scale than the CNT. Moreover, the planar feature of a GO sheet makes it easier to assemble into paper-like materials as compared to CNT. The fabrication method based on the flow directed filtration allows graphene oxide aqueous suspension induces self-assembly of individual sheets into a stacked, layered structure with near-parallel sheet arrangement, yielding a self-supporting, mechanically strong paper upon drying (Stankovich et al., 2010).

The structure of GO paper is unique with each GO sheets are interlocked/tiled together in a near-parallel manner with the presence of water molecules act as interlayer adhesive through hydrogen bonding. Figure 6.1 compares the GO paper structure with the film one at a cross-section point of view. As shown in Figure 6.1 (a), the GO layers in paper are orderly arranged with layer to layer distance of about 0.83 nm embedded in water molecule (Dikin et al., 2007). On the other hand, the nanosheets in GO film are disordered and randomly oriented as shown in Figure 6(b). Hence, the GO paper exhibits a better stiffness (in-plane) compared to the film.

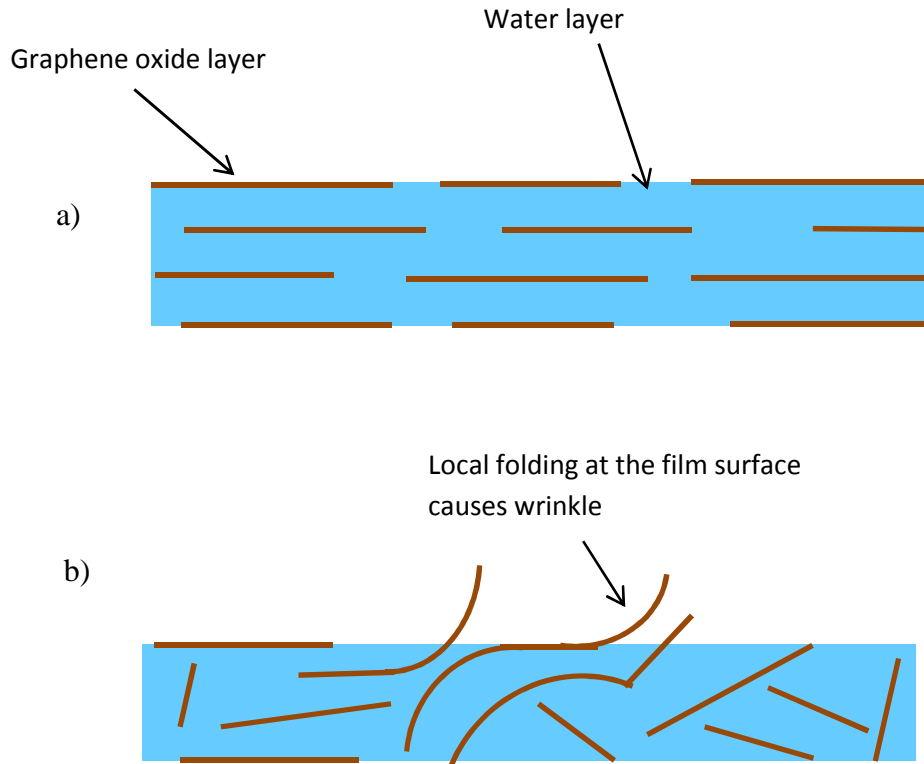


Figure 6.1: Graphene oxide (GO) saturable absorber structures: a) GO paper, and b) GO film.

Moreover, there is probability that the nanosheets can agglomerate after the drying process for the GO film. This is mainly due the interaction forces occurred between the nanosheets by the van der Waals attraction from the π -conjugated domains and the hydrogen bonding from the oxygen functional groups. In addition, the nanosheets can

be locally folded upon drying due to the electrostatic repulsion force and thus forming the film surface wrinkle which can increase the material refractive index significantly. The attraction and repulsion forces mentioned are highly depends on the nanosheets interacting distance, the surface charge density and the fabrication process. The GO paper, with its ordered structure provides smoother and evenly surface features as compared to the GOSA film. The smoother surface property of GO paper will significantly reduce light scattering effect in the optical fiber. As a result, the modulation depth of the SA can be enhanced for obtaining shorter Q-switched pulse width and the lower refractive index will also promote higher laser output power.

6.3 Characterisation of Graphene Oxide Paper

GO SA used in this experiment is based on Graphene Oxide paper purchased from Graphene Supermarket at a comparable low price due to its simpler manufacturing process with mass production. It has a thickness of 10 μm , radius of 2.0 cm, and a tensile modulus > 20 GPa. A small piece of the GO material was cut at a size that could cover the fiber optical path entirely. In a similar manner as demonstrated in Chapter 3, the GO paper piece is placed on the fiber ferrule facet with the index matching gel acted as an adhere element. Fig. 6.2 shows the microscopic image of a fiber ferrule consisting of a piece of the GO paper with a surrounding index matching gel. As shown in the figure, the GO paper sits at the center of the inner section covering the fiber core and thus blocking the laser path.

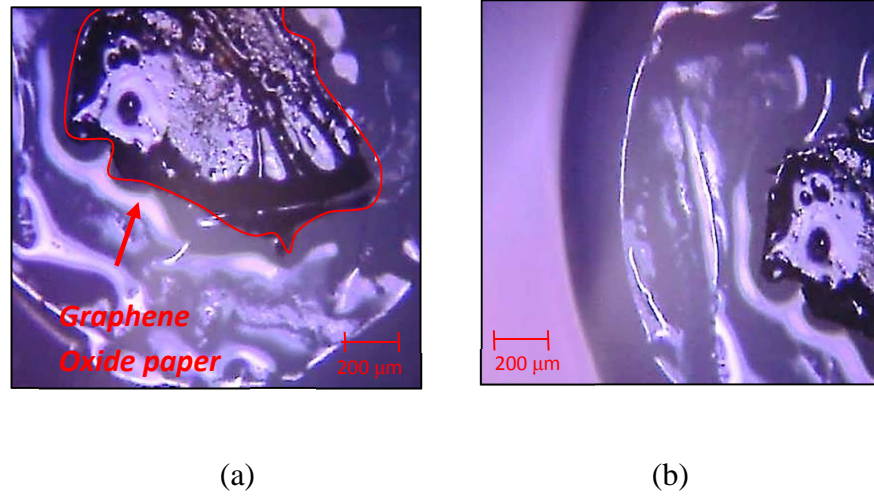


Figure 6.2: Microscopic image of a) Graphene Oxide (GO) paper surrounded by index matching gel b) Fiber ferule face showing the inner (dark area) and outer (bright area) sections of the ferule. The GO paper sits at the center of the inner section covering the fiber core.

Raman spectrum of GO paper was measured using Renishaw Raman Spectroscopy. In the measurement, a 50 mW laser at wavelength 532 nm was radiated on the GO paper for duration of 10 s to generate a Raman spectrum as shown in Fig. 6.3. The peaks of D and G bands of GO normally located around 1352 cm^{-1} and 1585 cm^{-1} , but it is found to be at approximately 1353.00 cm^{-1} and 1585.35 cm^{-1} respectively in Fig. 2. The relative intensity ratio of both D and G peaks (I_D/I_G) has a value of 0.8971. On the other hand, the small peak at 2329 cm^{-1} is the N_2 peak which indicates the presence of ambient Nitrogen gas. In Fig. 6.3, the 2D band which normally used to distinguish the thickness and doping level of the graphene sheets was not observed. This might due to the contribution of unintentional doping including O_2 (Zhao et al., 2012). After the Raman spectrum measurement is taken, the fiber connector is connected with another connector via FC/PC adapter to sandwich the GO paper to avoid major displacement and form the required SA.

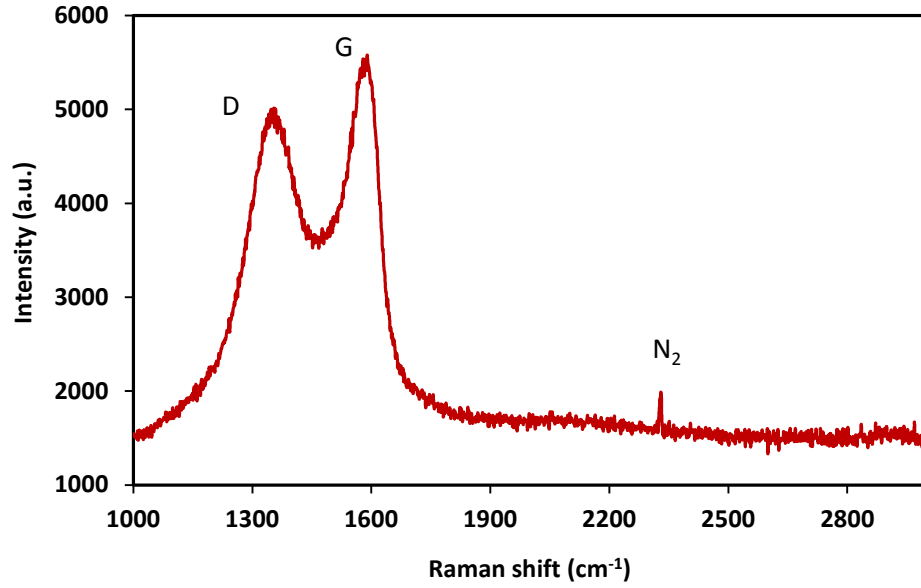


Figure 6.3: Raman spectrum of Graphene Oxide paper measured using Renishaw Raman Spectroscopy.

6.4 Experimental arrangement of Q-switched DWFL with Graphene Oxide Paper

Fig. 6.4 shows the experiment arrangement of a Q-switched dual-wavelength fiber ring laser with a total laser resonator length of approximately 6 m long. A 3 m long EDF as gain medium is used to provide an amplified spontaneous emission (ASE) at C-band by pumping it with a 980 nm laser diode through a wavelength division multiplexer (WDM). The two isolators are used to ensure unidirectional light propagation and the stability of the generated laser. A photonics crystal fiber (PCF) in 10 cm long, polarisation controller (PC) and a tunable band pass filter (TBF) are used to produce a stable and narrow spaced dual-wavelength laser via Mach-Zehnder interferometer effect (Chen et al., 2009), band pass filtering and polarization hole burning (PHB) effect (Moon et al., 2005, Feng et al., 2008, Tu et al., 2008). The PCF is mechanical coupled with SMF-28 fiber via the bare fiber holders giving an insertion loss of about 6 dB and it also exhibit zero-dispersion wavelength at about 1550 nm. In

the inset of Fig. 6.4, shows the microscopic picture of the PCF's cross section, having air holes with diameter of $5.06\ \mu\text{m}$ and the distance between the centers of each hole is $5.52\ \mu\text{m}$. It has a solid core structure with a diameter of $4.37\ \mu\text{m}$ and a fiber diameter of $124\ \mu\text{m}$. The hollow holes at the cladding and the solid core structure gives rise to its birefringence property due to having high effective refractive indices difference between the two regions.

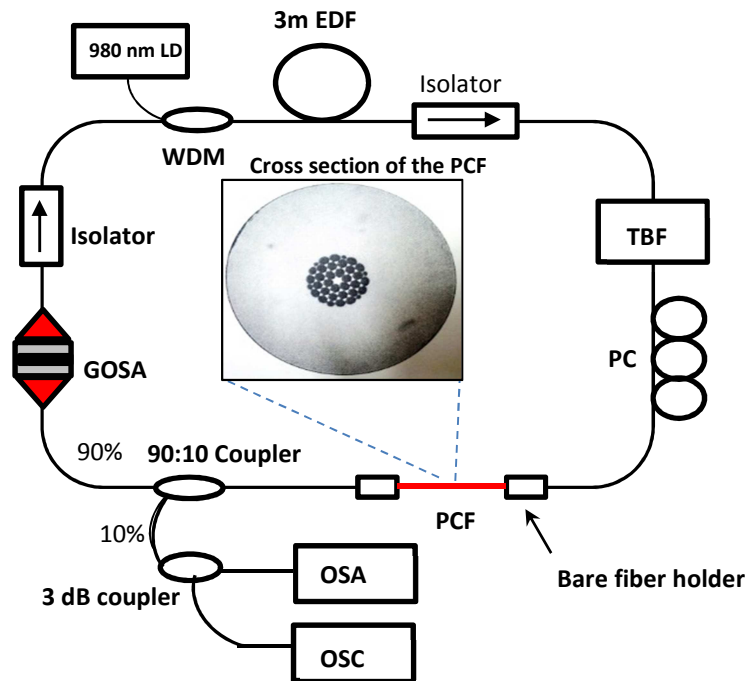


Figure 6.4: Experimental arrangement of the dual-wavelength Q-switched fibre laser.

The multi-wavelength laser is produced by having the PCF incorporated in the resonator which produces the fringe spacing effect or the Mach–Zehnder interferometer effect. Since, light propagating in the PCF at the cladding has smaller effective refractive index as compared to the light propagating at the core; the light fundamental and cladding modes propagate at different phase velocities. The phase difference is

produced as the modes propagate along the PCF and depends on the wavelength of the guided light and the length of the PCF. Since the phase velocities and the phase difference are wavelength dependent, the optical power transmitted by the PCF will be maximum at certain wavelengths and minimum at others which give rise to the fringe spacing effect (Chen et al., 2009). The laser transmission peaks with the spacing between consecutive peaks of a two mode PCF is given by $\Delta\lambda = \lambda^2/\Delta n_e L$, where Δn_e is the effective refractive indices difference between the core and cladding modes in the PCF or simply the birefringence coefficient and L is the PCF length.

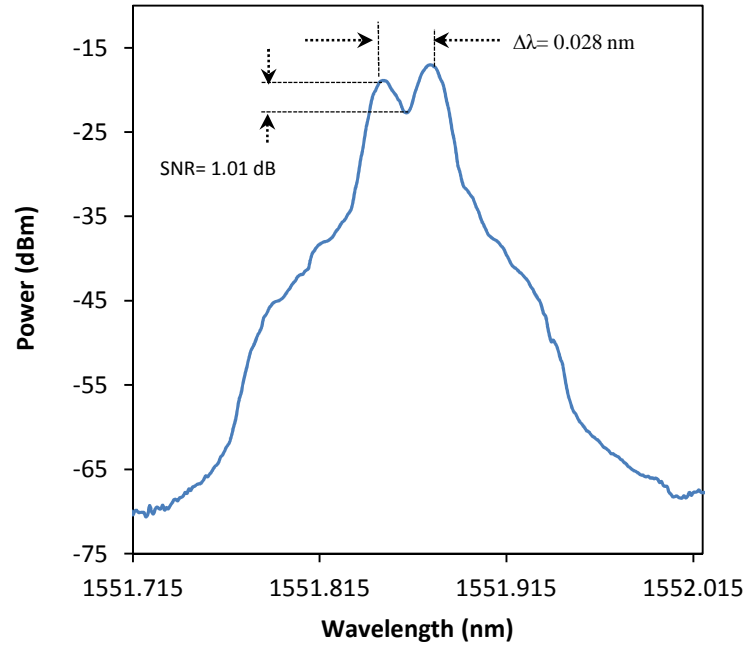
The PC is used to change the polarization states and allows the adjustment of the birefringence modes in order to control the number of laser wavelength peaks and balance the gain and loss in the laser resonator. In the absence of the PCF and PC in a ring laser, different light wavelengths propagating in the cavity have nearly similar polarization states. In contrast, the presence of the PCF and PC in the cavity produce diverse polarization states of different wavelengths due to wavelength-dependent polarization rotations which give rise to PHB effect when the light enters the EDFA. The PHB effect is responsible to give rise to spectral hole burning effect which in turn reduces the EDF homogeneous line width and suppress mode competition. As a result, stable multiwavelength laser at room temperature can be obtained.

For the generation of the dual-wavelength laser, a tunable Band-pass filter (TBF) with a bandpass bandwidth of 0.8 nm and tuning resolution of 0.05 nm is employed into the laser cavity to filter the unwanted laser emissions. By carefully fine tune the TBF and PC, a narrow spacing dual-wavelength laser is obtained. Without the TBF, the multi-wavelength laser will tend to lase at wavelengths with a larger spacing. A GOSA assembly is then placed inside the laser cavity as a component to generate the Q-switched dual-wavelength laser. It is noted that, the GO paper does not exhibit

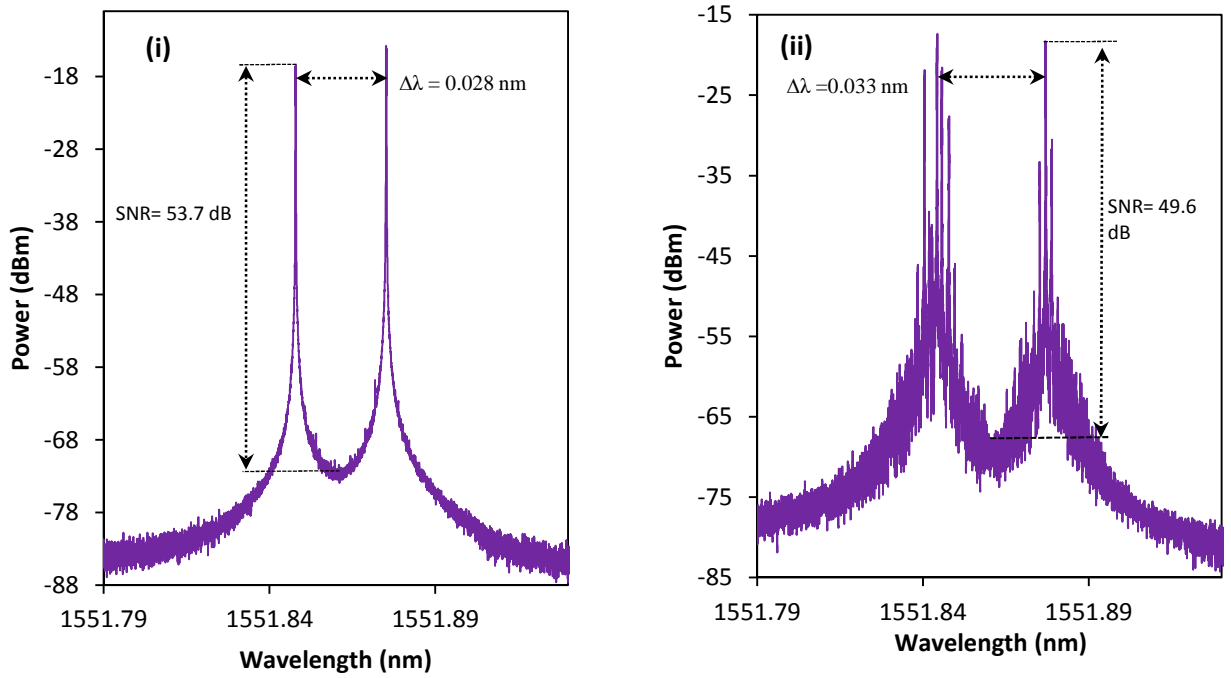
birefringence property; therefore it does not affect the polarisation states of the propagating light and therefore does not affect the multi-wavelength laser generation. A 90:10 coupler is used to tap out 10% of the laser light from the ring cavity. In order to make accurate measurements, a 3dB coupler is used to split the laser power into two, where one channel is connected to the optical spectrum analyser (OSA) to monitor the dual-wavelength laser spectrum while the other channel to measure either average output power, pulse pattern, and RF spectrum.

6.5 Performance of the Q-switched DWFL

At first, the generation of the continuous wave (CW) dual-wavelength fiber laser (DWFL) was obtained by pumping a 66 mW of 980 nm laser from the laser diode into the ring cavity without the GOSA. The optical spectrum of the narrow spacing DWFL was monitored using both from the low resolution OSA (Yokogawa-AQ6370C) and high resolution OSA (APEX AP2051A – at 0.16 pm resolution and 0.164 nm span). The PC is fine tune until dual-wavelength laser is generated and measured from the OSAs as shown in Figs. 6.5 a) and b), where the spacing between the two wavelengths of 28 pm is obtained for both from the two different OSA measurements. The peak powers for the dual-wavelength CW laser, at low resolution OSA are measured to be -19 dBm and -17.6 dBm which gives the power difference of 1.4 dB. At a similar condition, but measured using high resolution OSA, the peak powers for the dual-wavelength laser are -17.8 dBm and -14.3 dBm which gives a power difference of 3.5 dB. This difference in set of powers between two sets of measurements are due to the difference in the sensitivity between the two OSAs in measuring power level. On the other hand, the difference in peak powers of the dual-wavelength is due the gain competition owing to the homogeneous gain broadening in the erbium doped fiber. There is also a significant in difference in the signal to noise ratio (SNR) values between the two measurements.



a) Low resolution OSA



b) high resolution OSA

Figure 6.5: Optical spectra of dual-wavelength laser; a) measured using low resolution OSA at CW operation, b) measured using high resolution OSA at (i) CW and (ii) Q-switched.

The low resolution OSA gives SNR of 1.01dB, while the high resolution OSA gives 53.7 dB of SNR with 0.6 pm of 3 dB linewidth.

The major difference is owing to the high resolution OSA has higher sensitivity to detect more light signals at different wavelengths. After the CW dual-wavelength laser measurements, the fiber patchcords contained the GOSA is incorporated into the ring laser resonator to trigger the Q-switching effect. Fig. 6.5 b (ii) shows the high resolution optical spectrum scan after the GOSA is placed in the cavity. Series of spikes are observed which are the multi-longitudinal mode oscillations caused by the GOSA interfering the pre-lase signal to make strong lasing mode selection. The Q-switched DWFL obtained, has an approximately wavelength spacing of 33 pm and a SNR of 49.6 dB, which differs slightly when operating in CW regime due to the multi-longitudinal mode oscillations. It is noted that, at a resonator length of 6 m, the band-pass bandwidth of 0.8 nm can allow more than 2000 longitudinal modes to transverse through the TBF. To monitor the optical power fluctuation of the Q-switched DWFL in time domain, the other port of the 10% output is connected to an InGaAs photodetector (Thorlabs

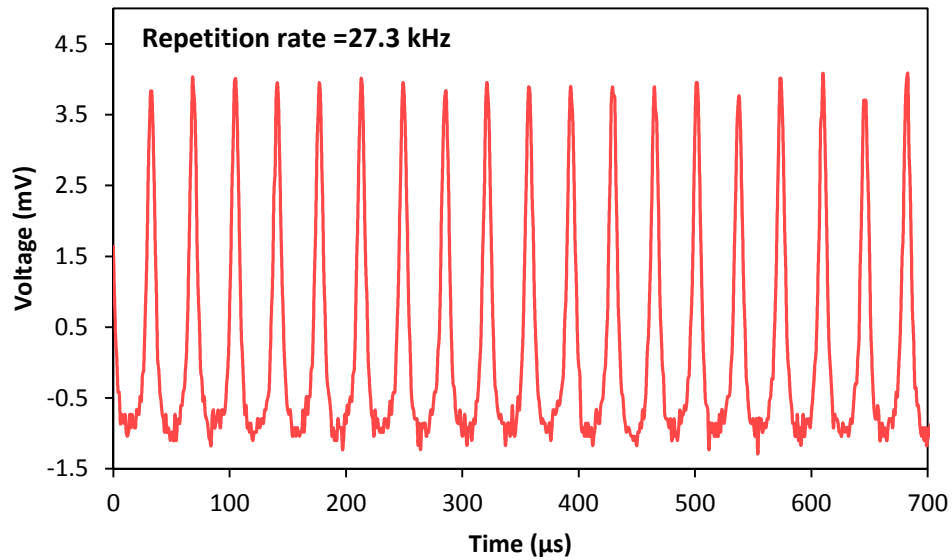


Figure 6.6: The Q-switched dual-wavelength fiber laser pulse train pumped at 66 mW.

MOBEL D40FC) that linked to a digital oscilloscope (OSC, LeCroy 500 MHz). A series of stable pulse train with pulse repetition rate of 27.3 kHz is observed as shown in Fig. 6.6 at the pump power of 66 mW.

In order to study the quality and stability of the Q-switched pulse generated, a few single pulses are captured in a higher resolution time domain setting using digital oscilloscope with time separation of roughly 10 s for each of them at the same pump power. They are then overlap together to observe the different between each pulse pattern as shown in Fig. 6.7. It is observed from the figure that the maximum amplitude fluctuation of the pulses is fall within 0.57 mV with maximum amplitude of 5.31 mV. The average pulse width is found to be 7.4 μ s at full width half maximum (FWHM) with an approximately maximum pulse width variation of 0.85 μ s. The stability of the Q-switched pulses is further analysed by measuring the power output fluctuation with

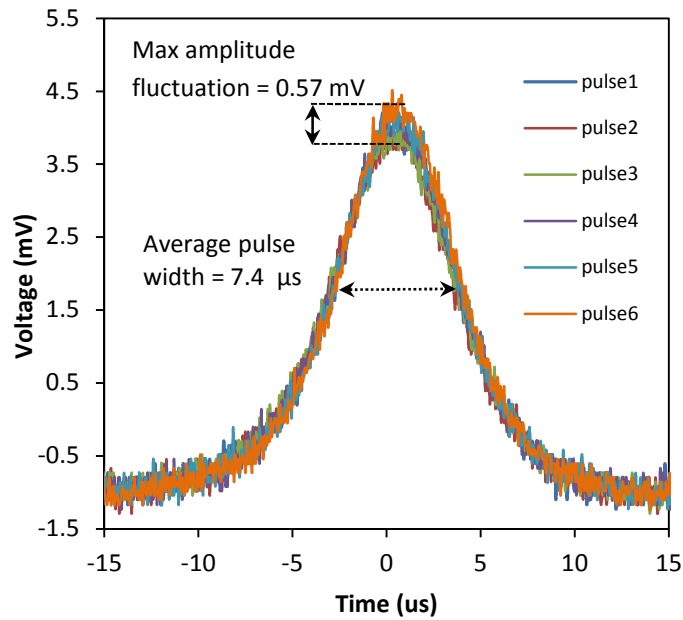


Figure 6.7: 6 different pulse traced of a single pulse profile pumped at 66 mW.

RF spectrum analyser (RFSA). Fig. 6.8 shows the first harmonic RF spectrum of the Q-switched DWFL at 20 kHz span, with resolution and video bandwidth of 300 Hz and 1 MHz respectively. The signal has a peak-to-noise ratio of about 37 dB which confirm pulse stability (Tan et al., 2013), agreeing with the time domain analysis as shown in Fig. 6.7. The value obtained for $|10 \log (P_c/P_a)|$ and $(\Delta f_a/\Delta f_{res})$ is about 37 dB and 4.3 respectively, thus the energy fluctuation calculated is about 0.0293 or 2.93% which confirms pulse train stability.

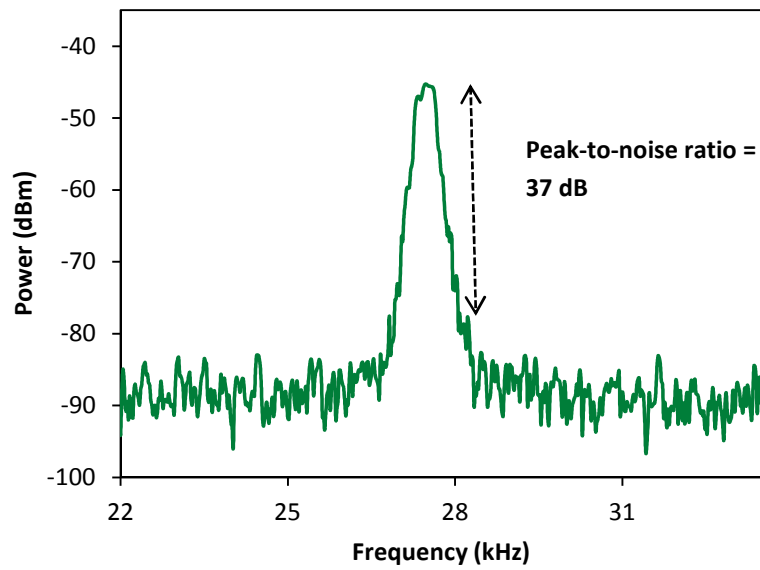


Figure 6.8: Radio frequency spectrum of the Q-switched dual-wavelength fiber laser at the fundamental harmonic.

With current fixed setup, minor tuning of the Q-switched DWFL can be performed by changing the 980 nm pump power. The changes of the 980 nm pump power offers slight tuning in the repetition rate and pulse width to fulfil different applications which need different pulse specifications. Fig. 6.9 shows repetition rate and pulse width curves with standard error bars are computed to indicate where the data mean are most likely to be at different pump powers. The threshold to trigger the Q-switching is level at about

54 mW. The repetition rate increases linearly from the threshold to a 31 kHz of repetition rate 69 mW of pump power which is at the limit condition for stable Q-switched operation. Since the dual-wavelength laser has a very narrow spacing and broad laser bandwidth, the two wavelengths will eventually bound to merge together as the pump power is increased above 69 mW. This contributed to unstable dual-wavelength laser generation which limits to further increase in the pump power for Q-switching operation. Moreover, the pulse width decreases with exponent manner from 13.2 μs , reaching to a saturation value of about 7.04 μs at 69 mW pump power. Fig. 6.10 shows the average output power dynamics at different pump powers. The average output power increases linearly as the pump power is increased. Under the pump power of 69 mW, the average output power of 0.086 mW and pulse energy of 2.8 nJ is obtained.

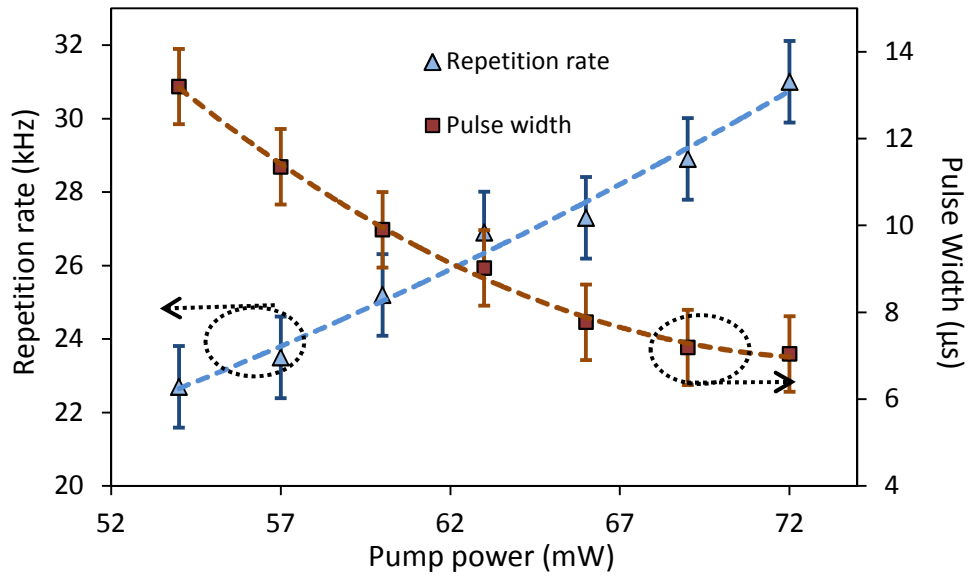


Figure 6.9: Pulse width and repetition rate characteristics at different pump powers.

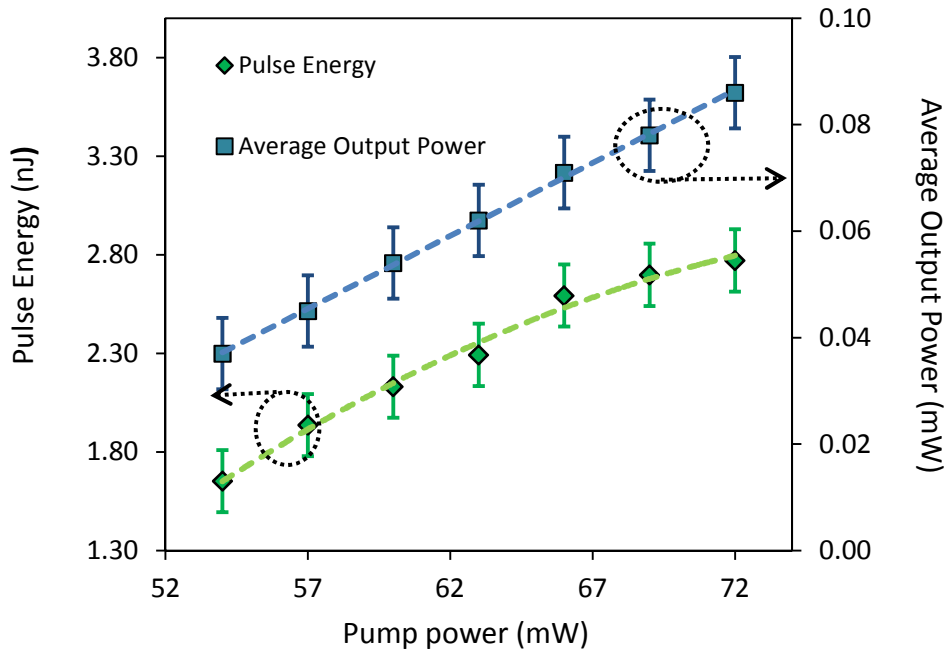


Figure 6.10: Average output power and pulse energy characteristics at different pump powers.

6.6 Summary

The GO paper fabrication method, structure and property have been reviewed and the necessary comparison has been made with the GOSA film. The analysis shows that due to the ordered structure of GO paper, it can exhibit smoother surface area and thus can reduce the scattering effect when incorporated in the laser resonator. The GO paper has been tested in producing narrow spaced Q-switched dual-wavelength fiber laser. The high resolution OSA is used to enable accurate spectrum measurement of the laser at CW and Q-switched regime. It has a Q-switched threshold of around 54 mW. At the pump power of 66 mW, the Q-switched DWFL has an approximately wavelength spacing of 33 pm and SNR of 49.6 dB. At this pump power, RF spectrum and time domain analysis confirms pulse stability with RF signal SNR of 37 dB and a maximum pulse width variation of 0.85 μ s. Above the pump power of 69 mW, the Q-switched DWFL becomes unstable and the pulse width widens as the pump power is increased. However, at 69 mW of pump power, the pulse has a pulse width, repetition rate, and

pulse energy of 7.04 μs , 31 kHz and 2.8 nJ respectively. These properties make our Q-switched DWFL suitable in the applications such as biomedical, microwave optics, metrology, and environmental sensor.

CHAPTER 7: CONCLUSION AND FUTURE OUTLOOK

6.1 Conclusion

The main purpose of this work is to demonstrate the generation of Q-switched fiber lasers at both 1.5 and 2 μm wavelength regions using graphene oxide (GO) material as saturable absorber (SA) device. This study also aimed to investigate how the optical and chemical properties of GO material are different as compared to graphene and carbon nanotube (CNT). Various fabrication methods in preparing the GOSA are also explored and evaluated. We also investigated how different fabrication methods affect the saturable and non-saturable absorption properties of the SA.

In chapter 2; the review and modification of differential rate equations and the pulse build-up equations have been established to specifically describe the Q-switched fiber laser operation in a ring configuration setup (unidirectional light propagation scheme). The theoretical analysis was based on quasi-three level active medium, which is continuously pumped by a typical laser diode. The analysis also includes both the upper and ground states absorption of the SA but excludes the carrier interaction. In addition, the pulse-build up equations, which were derived from the differential rate equations have also been reviewed and modified in Chapter 2 to describe the Q-switched threshold, the photon density rate increment and the gain population inversion dynamics. This chapter also reviewed the saturable absorption principles at the microscopic level and the non-linear saturable absorption behaviour. Those works have been established in order to predict, explain and analyse the Q-switching performance of the laser when GO is used as the SA. Furthermore, with the established theory, one can make prediction beyond from the obtained results in order to improve and optimize either the fabrication process or the laser resonator design.

The main contributions of this work are listed as follows:

In chapter 3, the fabrication and characterization of the GO film were presented. The fabrication and characterisation includes:

- 1) GO colloid with a concentration of 0.5 mg/mL has been prepared from pure graphite flakes via Huang's Method which provides simpler and cost-effective process as compared to other fabrication methods.
- 2) UV-vis spectrum measurement and analysis are performed for the characterisations of the GO colloid. The spectrum analysis, reveals a peak to shoulder absorbance intensity ratio value of 3.26 which suggests that the GO sample in this work has a high number of aromatic rings.
- 3) A GO film was fabricated from the GO colloid via drop-casting method. The GO colloid with volume of 10 ml was thinly distributed onto a 90 mm petri-dish before it was left to dry at room temperature for 1 day to form a film. Then the film was cut into a piece and placed on fiber ferule core with index matching gel act as adhesive element.
- 4) Raman spectrum measurement and analysis on GO and CNT on the fiber ferule have been presented. The comparison analysis shows that the GO has much higher degree of disordered based on the observation of the significant difference in the D peak intensity as shown in the Raman spectrum.
- 5) The relationship between the intensity ratio (I_D/I_G) and the effective aromatic cluster correlation length, L_{Aeff} has been modelled and analysed to investigate the saturable absorption capacity of the GO. From this analysis, we can conclude that the GO material has significantly lower number of aromatic rings as compared to CNT and graphene due to the high concentration of defect caused by the presence of the oxygen functional groups. This leads to GO having lower capacity for saturable absorption.

In chapter 4, a Q-switched fiber laser generation has been successfully demonstrated using a very short length of Bismuth-erbium doped fiber, Bi-EDF (21 cm) as a gain medium and with the GO film. The performance of the laser is listed below,

- 1) The tunability of Q-switched laser has been demonstrated using TBF where the laser maintained an average laser power of -16.8 dBm within the operating wavelength range at the pump power of 92 mW.
- 2) The Q-switched threshold is measured to be about 65 mW of pump power. At the maximum pump power, the output power of 0.11 mW is achieved with pulse energy and peak power of 4.3 nJ and 0.56 mW are obtained respectively. The narrowest pulse width of 7.7 μ s and maximum repetition rate of 27.2 kHz are obtained.
- 3) The pulse shape measured resemble a nearly Gaussian symmetrical shape where it has been observed that at higher pump power, the pulse skewness become slightly greater.
- 4) RFSA shows a stable Q-switched laser at the pump power of 92 mW having a peak-to-noise pedestal ratio of about 31 dB at the fundamental frequency (21.8 kHz), with the calculated energy fluctuation obtained is 6.17 %. This analysis also suggests that the pulse duration fluctuations are also stable due to the mutual correlation with the pulse intensity fluctuations.
- 5) The low optical efficiency, limitations of the pulse width and signature of pulse width saturation have been discussed in relation to the quantum efficiency of the Bi-EDF, saturable absorption and nonsaturable loss of the GOSA film respectively. The nonsaturable loss that depends on the film surface wrinkles and film thickness of the GO film has been addressed which also affected the optical efficiency of the laser.

In chapter 5, GO layers have been optically deposited onto fiber ferule facet to generate Q-switched fiber laser at the eye-safe 2 micron region. The efficiency of the deposition process should be improved by optimizing the optical deposition process such as increase in the optical power and the use of reflectrometry technique. Moreover, an experimental work is still needed to determine the thermophoretic mobility, D_T sign which can degrade or contribute the optical deposition efficiency. Below are the list of findings and the completed work done in this chapter.

- 1) GO layers have been successfully deposited onto a fiber ferule facet via a simpler, cost-effective and less toxic method based on an optical deposition technique. The hydrophilic property of the GO material allowing the ease and effective bulk layers dispersion in water to attain an average particle size of 90 nm.
- 2) The optical deposition mechanism that worked based on heat convection and thermophoresis have been explained and evaluated.
- 3) Optical fiber scope was used to ensure the successful of GO layers deposited onto the core of the fiber ferule.
- 4) A comparison analysis on Raman spectra has been performed to evaluate the degree of defect between the GOSA by optical deposition and GOSA film. The analysis on the I_D/I_G ratio value shows that GOSA optically deposited with the ratio value of $0.92 > 0.86$ (GOSA film) confirms that the GOSA film has higher density of defect. We can conclude that the GOSA film has higher density of defect and lesser number of aromatic rings leading to lower saturable absorption coefficient.
- 5) A 2 micron Q-switched fiber laser has been successfully generated using the GOSA, which was optically deposited on a fiber ferule facet and a 2 meters thulium-doped fiber as the gain medium.

- 6) A Q-switched laser threshold of 125 mW was obtained with a maximum pulse repetition rate of 16.0 kHz and minimum pulse width of 9.8 μ s at the maximum pump power of 164 mW. The maximum average output power of 0.3 mW, pulse energy of 18.8 nJ and pulse peak power of 1.91 mW were obtained.
- 7) The energy fluctuation of 8.6% obtained is relatively higher than the value obtained from chapter 4 (6.17%). In addition, the pulse pattern shows that it has higher pulse peak fluctuations with higher standard deviations. These results suggest that the laser is less stable due to mode beating and mode competition. This is can be solved by utilizing a single light propagation scheme as demonstrated in chapter 4 to promote single longitudinal mode (SLM) operation.

In Chapter 6, the fabrication method, layer structure and property of GO paper have been reviewed and the necessary comparison has been made with the GOSA film. Due to the ordered layer structure of GO paper, the paper exhibit smoother surface area as compared to the GO film as demonstrated in chapter 3. This can reduce the scattering effect and thus the nonsaturable loss when the GO paper is incorporated in the laser resonator. Then, the GO paper has been tested in the generation of a narrow spacing Q-switched DWF with below are the list of the test results.

- 1) Laser spectrum analysis is measured using both from the low and high resolution optical spectrum analyser (OSA); the results show there is a large in difference in terms of the SNR values and power levels. This is due to the high resolution OSA is more sensitive of detecting more light signal at different wavelengths.

- 2) A Q-switched threshold of around 54 mW was obtained and has an approximately wavelength spacing of 33 pm and SNR of 49.6 dB when pumped at 66 mW.
- 3) RF spectrum and time domain analysis confirms pulse stability with RF signal SNR of 37 dB and a maximum pulse width variation of 0.85 μ s at the pump power of 66 mW. The energy fluctuation of 2.93% was also obtained at this pump power.
- 4) Further analysis shows that at above 69 mW of pump power, the Q-switched DWFL becomes unstable and the pulse width widens as the pump power is increased. Therefore, at the maximum pump power of 69 mW for stable q-switching operation, the pulse has a repetition rate of 31 kHz, pulse width of 7.04 μ s and pulse energy of 2.8 nJ.

6.2 Future work

The future works should be focused on the following topics in order to improve the Q-switched laser performance and to develop a better saturable absorber device:

- 1) The oxidation level of GO needs to be further increased to increase the GO sheet size and the number of aromatic rings. This can be accomplished by controlling KMnO_4 :acid (H_2SO_4 : H_3PO_4) weight ratios where the higher ratio is expected to give a higher oxidation level. An additional experimental work is needed in order to prove the assumption.
- 2) The optimization of laser cavity should be carried out by reducing the total cavity length, and by optimizing the pumping scheme. This will improve the Q-switched laser output pulse width, increases the average output power and efficiency. Moreover, a thinner layer and evenly surface of the GO film needs to be fabricated in order to minimize beam divergence and scattering effects to reduce the nonsaturable loss and improve the laser performance.

- 3) The numbers of GO layers deposited on the fiber ferule through the optical deposition method needs to be reduced in order to reduce the nonsaturable loss. This can be accomplished by using the reflectrometry methods, controlling the right amount of optical power and reduce the duration of optical radiation. In addition, further analysis on the thermophoretic mobility for the negatively charged GO colloid is needed in order to determine the optical deposition efficiency.
- 4) The 2 micron Q-switched fiber laser stability can be improved by utilizing unidirectional propagation scheme to minimize longitudinal mode competition and to promote SLM operation.

REFERENCES

- Abraham, N. B., Lugiato, L. A., & Narducci, L. M. (1985). Overview of instabilities in laser systems. *JOSA B*, 2(1), 7-14.
- Ado, J., Dresselhaus, M. S., Ricchiro, S., & Dresselhaus, G. F. (2011). Raman Spectroscopy in Graphene Related Systems.
- Agrawal, G. (2010). *Applications of nonlinear fiber optics*. Academic press.
- Ahmad, H., Parvizi, R., Dimyati, K., Tamjis, M. R., & Harun, S. W. (2010). FWM-based multi-wavelength erbium-doped fiber laser using Bi-EDF. *Laser Physics*, 20(6), 1414-1417.
- Ahmad, H., Shahi, S., & Harun, S. W. (2010). Bismuth-based erbium-doped fiber as a gain medium for L-band amplification and Brillouin fiber laser. *Laser physics*, 20(3), 716-719.
- Ahmad, H., Zulkifli, A. Z., Thambiratnam, K., & Harun, S. W. (2013). Q-switched Zr-EDF laser using single-walled CNT/PEO polymer composite as a saturable absorber. *Optical Materials*, 35(3), 347-352.
- Ahmad, H., Zulkifli, M. Z., Thambiratnam, K., Latif, S. F., & Harun, S. W. (2009). High power and compact switchable bismuth based multiwavelength fiber laser. *Laser Physics Letters*, 6(5), 380-383.
- Akhavan, O. (2010). The effect of heat treatment on formation of graphene thin films from graphene oxide nanosheets. *Carbon*, 48(2), 509-519.
- Antunes, E. F., Lobo, A. O., Corat, E. J., Trava-Airoldi, V. J., Martin, A. A., & Veríssimo, C. (2006). Comparative study of first-and second-order Raman spectra of MWCNT at visible and infrared laser excitation. *Carbon*, 44(11), 2202-2211.
- Avouris, P. (2010). Graphene: electronic and photonic properties and devices. *Nano letters*, 10(11), 4285-4294.
- Bai, H., Li, C., Wang, X., & Shi, G. (2010). A pH-sensitive graphene oxide composite hydrogel. *Chemical Communications*, 46(14), 2376-2378.

- Balapanuru, J., Yang, J. X., Xiao, S., Bao, Q., Jahan, M., Polavarapu, L., ... & Loh, K. P. (2010). A Graphene Oxide–Organic Dye Ionic Complex with DNA-Sensing and Optical-Limiting Properties. *Angewandte Chemie*, 122(37), 6699-6703.
- Bao, Q., Zhang, H., Ni, Z., Wang, Y., Polavarapu, L., Shen, Z., ... & Loh, K. P. (2011). Monolayer graphene as a saturable absorber in a mode-locked laser. *Nano Research*, 4(3), 297-307.
- Baughman, R. H., Cui, C., Zakhidov, A. A., Iqbal, Z., Barisci, J. N., Spinks, G. M., ... & Kertesz, M. (1999). Carbon nanotube actuators. *Science*, 284(5418), 1340-1344.
- Berger, C., Song, Z., Li, X., Wu, X., Brown, N., Naud, C., ... & de Heer, W. A. (2006). Electronic confinement and coherence in patterned epitaxial graphene. *Science*, 312(5777), 1191-1196.
- Bird, R. B., Stewart, W. E., & Lightfoot, E. N. (2007). Transport Phenomena (revised second ed.) John Wiley & Sons. *New York*.
- Brodie, B. C. (1860). Sur le poids atomique du graphite. *Ann. Chim. Phys.*, 59(466), e472.
- Brodie, B. C. (1859). On the atomic weight of graphite. *Philosophical Transactions of the Royal Society of London*, 249-259.
- Buongiorno, J. (2006). Convective transport in nanofluids. *Journal of Heat Transfer*, 128(3), 240-250.
- Burshtein, Z., Blau, P., Kalisky, Y., Shimony, Y., & Kikta, M. R. (1998). Excited-state absorption studies of Cr^{4+} ions in several garnet host crystals. *Quantum Electronics, IEEE Journal of*, 34(2), 292-299.
- Bykkam, S., Rao, K. V., Chakra, C. H. S., & Thunugunta, T. (2013). Synthesis and characterization of graphene oxide and its antimicrobial activity against klebsiella and staphylococcus. *International Journal of Advanced Biotechnology Research*, 4, 142-146.
- Cançado, L. G., Jorio, A., Ferreira, E. M., Stavale, F., Achete, C. A., Capaz, R. B., ... & Ferrari, A. C. (2011). Quantifying defects in graphene via Raman spectroscopy at different excitation energies. *Nano letters*, 11(8), 3190-3196.

- Cao, W. J., Wang, H. Y., Luo, A. P., Luo, Z. C., & Xu, W. C. (2012). Graphene-based, 50 nm wide-band tunable passively Q-switched fiber laser. *Laser Physics Letters*, 9(1), 54.
- Chang, Y. M., Kim, H., Lee, J. H., & Song, Y. W. (2010). Multilayered graphene efficiently formed by mechanical exfoliation for nonlinear saturable absorbers in fiber mode-locked lasers. *Applied Physics Letters*, 97(21), 211102.
- Chen, W. G., Lou, S. Q., Feng, S. C., Wang, L. W., Li, H. L., Guo, T. Y., & Jian, S. S. (2009). Switchable multi-wavelength fiber ring laser based on a compact in-fiber Mach-Zehnder interferometer with photonic crystal fiber. *Laser physics*, 19(11), 2115-2119.
- Coleman, J. N., Blau, W. J., Dalton, A. B., Munoz, E., Collins, S., Kim, B. G., ... & Baughman, R. H. (2003). Improving the mechanical properties of single-walled carbon nanotube sheets by intercalation of polymeric adhesives. *Applied Physics Letters*, 82(11), 1682-1684.
- Compton, O. C., An, Z., Putz, K. W., Hong, B. J., Hauser, B. G., Brinson, L. C., & Nguyen, S. T. (2012). Additive-free hydrogelation of graphene oxide by ultrasonication. *Carbon*, 50(10), 3399-3406.
- Davis, C. C. (2014). *Lasers and electro-optics: fundamentals and engineering*. Cambridge University Press.
- Delevaque, E., Georges, T., Monerie, M., Lamouler, P., & Bayon, J. F. (1993). Modeling of pair-induced quenching in erbium-doped silicate fibers. *Photonics Technology Letters, IEEE*, 5(1), 73-75.
- Delgado-Pinar, M., Zalvidea, D., Diez, A., Perez-Millan, P., & Andres, M. (2006). Q-switching of an all-fiber laser by acousto-optic modulation of a fiber Bragg grating. *Optics Express*, 14(3), 1106-1112.
- Dennis, M. L., Sova, R. M., & Clark, T. R. (2007, March). Dual-wavelength Brillouin fiber laser for microwave frequency generation. In *Optical Fiber Communication Conference* (p. OWJ6). Optical Society of America.
- Dikin, D. A., Stankovich, S., Zimney, E. J., Piner, R. D., Dommett, G. H., Evmenenko, G., ... & Ruoff, R. S. (2007). Preparation and characterization of graphene oxide paper. *Nature*, 448(7152), 457-460.

- Dong, J., & Ueda, K. I. (2005). Longitudinal-mode competition induced instabilities of Cr^{4+} , Nd^{3+} : $\text{Y}_3\text{Al}_5\text{O}_{12}$ self-Q-switched two-mode laser. *Applied Physics Letters*, 87(15), 151102.
- Dong, J. (2003). Numerical modeling of CW-pumped repetitively passively Q-switched Yb: YAG lasers with Cr: YAG as saturable absorber. *Optics communications*, 226(1), 337-344.
- Dresselhaus, M. S., Dresselhaus, G., Saito, R., & Jorio, A. (2005). Raman spectroscopy of carbon nanotubes. *Physics reports*, 409(2), 47-99.
- Eda, G., & Chhowalla, M. (2010). Chemically derived graphene oxide: towards large-area thin-film electronics and optoelectronics. *Advanced Materials*, 22(22), 2392-2415.
- Eda, G., Fanchini, G., & Chhowalla, M. (2008). Large-area ultrathin films of reduced graphene oxide as a transparent and flexible electronic material. *Nature nanotechnology*, 3(5), 270-274.
- Eda, G., Lin, Y. Y., Mattevi, C., Yamaguchi, H., Chen, H. A., Chen, I. S., ... & Chhowalla, M. (2010). Blue photoluminescence from chemically derived graphene oxide. *Advanced Materials*, 22(4), 505.
- El-Sherif, A. F., & King, T. A. (2003). High-energy, high-brightness Q-switched Tm^{3+} -doped fiber laser using an electro-optic modulator. *Optics communications*, 218(4), 337-344.
- Feng, S., Xu, O., Lu, S., Mao, X., Ning, T., & Jian, S. (2008). Single-polarization, switchable dual-wavelength erbium-doped fiber laser with two polarization-maintaining fiber Bragg gratings. *Optics express*, 16(16), 11830-11835.
- Fenstermaker, C. A., & McCrackin, F. L. (1969). Errors arising from surface roughness in ellipsometric measurement of the refractive index of a surface. *Surface Science*, 16, 85-96.
- Ferrari, A. C., & Robertson, J. (2000). Interpretation of Raman spectra of disordered and amorphous carbon. *Physical review B*, 61(20), 14095.
- Fu, H. L., & Gao, L. (2012). Effect of interfacial nanolayer on thermophoresis in nanofluids. *International Journal of Thermal Sciences*, 61, 61-66.

- Gao, W., Singh, N., Song, L., Liu, Z., Reddy, A. L. M., Ci, L., ... & Ajayan, P. M. (2011). Direct laser writing of micro-supercapacitors on hydrated graphite oxide films. *Nature Nanotechnology*, 6(8), 496-500.
- Gao, Y., Liu, L. Q., Zu, S. Z., Peng, K., Zhou, D., Han, B. H., & Zhang, Z. (2011). The effect of interlayer adhesion on the mechanical behaviors of macroscopic graphene oxide papers. *ACS nano*, 5(3), 2134-2141.
- Gebhart, B., Jaluria, Y., Mahajan, R. L., & Sammakia, B. (1988). Buoyancy-induced flows and transport.
- Geist, F., Guyenot, M., Herbst, W., Pascher, H., Verkerk, R., & Prettl, W. (1997). Q-switched CO₂ laser with pulsed longitudinal discharge for nonlinear optical applications. *Review of scientific instruments*, 68, 3599-3600.
- Gerber, R. (1984). Magnetic filtration of ultra-fine particles. *Magnetics, IEEE Transactions on*, 20(5), 1159-1164.
- Gómez-Navarro, C., Weitz, R. T., Bittner, A. M., Scolari, M., Mews, A., Burghard, M., & Kern, K. (2007). Electronic transport properties of individual chemically reduced graphene oxide sheets. *Nano letters*, 7(11), 3499-3503.
- Gupta, A., Chen, G., Joshi, P., Tadigadapa, S., & Eklund, P. C. (2006). Raman scattering from high-frequency phonons in supported n-graphene layer films. *Nano letters*, 6(12), 2667-2673.
- Gupta, M. C., & Ballato, J. (Eds.). (2006). *The handbook of photonics*. CRC press.
- Hakulinen, T., & Okhotnikov, O. G. (2007). 8 ns fiber laser Q switched by the resonant saturable absorber mirror. *Optics letters*, 32(18), 2677-2679.
- Hamzah, A., Harun, S. W., Huri, N. A. D., Lokman, A., Arof, H., Paul, M. C., ... & Sahu, J. K. (2010). Multi-wavelength fiber laser with erbium doped zirconia fiber and semiconductor optical amplifier. *Optoelectronics and Advanced Materials-Rapid Communications*, 4(10), 1431-1434.
- Hansen, J. P., & Lowen, H. (2000). Effective interactions between electric double-layers. *arXiv preprint cond-mat/0002295*.

- Harun, S. W., Ismail, M. A., Ahmad, F., Ismail, M. F., Nor, R. M., Zulkepely, N. R., & Ahmad, H. (2012). A Q-switched erbium-doped fiber laser with a carbon nanotube based saturable absorber. *Chinese Physics Letters*, 29(11), 114202.
- Harun, S. W., Ismail, M. A., Ahmad, F., Ismail, M. F., Nor, R. M., Zulkepely, N. R., & Ahmad, H. (2012). A Q-switched erbium-doped fiber laser with a carbon nanotube based saturable absorber. *Chinese Physics Letters*, 29(11), 114202.
- Harun, S. W., Tamchek, N., Poopalan, P., & Ahmad, H. (2003). Double-pass L-band EDFA with enhanced noise figure characteristics. *Photonics Technology Letters, IEEE*, 15(8), 1055-1057.
- Haubner, K., Murawski, J., Olk, P., Eng, L. M., Ziegler, C., Adolphi, B., & Jaehne, E. (2010). The route to functional graphene oxide. *ChemPhysChem*, 11(10), 2131-2139.
- Huang, N. M., Lim, H. N., Chia, C. H., Yarmo, M. A., & Muhamad, M. R. (2011). Simple room-temperature preparation of high-yield large-area graphene oxide. *International journal of nanomedicine*, 6, 3443.
- He, H., Klinowski, J., Forster, M., & Lerf, A. (1998). A new structural model for graphite oxide. *Chemical Physics Letters*, 287(1), 53-56.
- Hummers Jr, W. S., & Offeman, R. E. (1958). Preparation of graphitic oxide. *Journal of the American Chemical Society*, 80(6), 1339-1339.
- Jeon, M. Y., Kim, N., Shin, J., Jeong, J. S., Han, S. P., Lee, C. W., ... & Park, K. H. (2010). Widely tunable dual-wavelength Er³⁺-doped fiber laser for tunable continuous-wave terahertz radiation. *Optics express*, 18(12), 12291-12297.
- Jiang, J., Oberdörster, G., & Biswas, P. (2009). Characterization of size, surface charge, and agglomeration state of nanoparticle dispersions for toxicological studies. *Journal of Nanoparticle Research*, 11(1), 77-89.
- Jiang, M., Ma, H. F., Ren, Z. Y., Chen, X. M., Long, J. Y., Qi, M., ... & Bai, J. T. (2013). A graphene Q-switched nanosecond Tm-doped fiber laser at 2 μ m. *Laser Physics Letters*, 10(5), 055103.
- Jung, I., Vaupel, M., Pelton, M., Piner, R., Dikin, D. A., Stankovich, S., ... & Ruoff, R. S. (2008). Characterization of thermally reduced graphene oxide by imaging ellipsometry. *The Journal of Physical Chemistry C*, 112(23), 8499-8506.

- Kashiwagi, K., Yamashita, S., & Set, S. Y. (2009). In-situ monitoring of optical deposition of carbon nanotubes onto fiber end. *Optics express*, 17(7), 5711-5715.
- Kashiwagi, K., & Yamashita, S. (2009). Deposition of carbon nanotubes around microfiber via evanescent light. *Optics express*, 17(20), 18364-18370.
- Kashiwagi, K., & Yamashita, S. (2010). *Optical Deposition of Carbon Nanotubes for Fiber-based Device Fabrication*. INTECH Open Access Publisher.
- Kilpela, A., Pennala, R., & Kostamovaara, J. (2001). Precise pulsed time-of-flight laser range finder for industrial distance measurements. *Review of Scientific Instruments*, 72(4), 2197-2202.
- Koechner, W. (2013). *Solid-state laser engineering* (Vol. 1). Springer.
- Kölbl, J., Fröschl, M., Seedsman, A., & Sperber, P. (2008, October). Near-infrared laser range finder using kHz repetition rate. In *SPIE Europe Security and Defence* (pp. 71150M-71150M). International Society for Optics and Photonics.
- Koskinen, R., Suomalainen, S., Paajaste, J., Kivistö, S., Guina, M., Okhotnikov, O., & Pessa, M. (2009, May). Highly nonlinear GaSb-based saturable absorber mirrors. In *SPIE Europe Optics+ Optoelectronics* (pp. 73540G-73540G). International Society for Optics and Photonics.
- Kostić, R., Mirić, M., Radić, T., Radović, M., Gajić, R., & Popović, Z. V. (2009). Optical characterization of graphene and highly oriented pyrolytic graphite. *Acta Physica Polonica A*, 116(4), 718-721.
- Kravets, V. G., Grigorenko, A. N., Nair, R. R., Blake, P., Anissimova, S., Novoselov, K. S., & Geim, A. K. (2010). Spectroscopic ellipsometry of graphene and an exciton-shifted van Hove peak in absorption. *Physical Review B*, 81(15), 155413.
- Kurkov, A. S. (2011). Q-switched all-fiber lasers with saturable absorbers. *Laser Physics Letters*, 8(5), 335.
- Lee, C., Wei, X., Kysar, J. W., & Hone, J. (2008). Measurement of the elastic properties and intrinsic strength of monolayer graphene. *science*, 321(5887), 385-388.

- Lerf, A., He, H., Forster, M., & Klinowski, J. (1998). Structure of graphite oxide revisited||. *The Journal of Physical Chemistry B*, 102(23), 4477-4482.
- Li, S. S., Tu, K. H., Lin, C. C., Chen, C. W., & Chhowalla, M. (2010). Solution-processable graphene oxide as an efficient hole transport layer in polymer solar cells. *ACS nano*, 4(6), 3169-3174.
- Loh, K. P., Bao, Q., Eda, G., & Chhowalla, M. (2010). Graphene oxide as a chemically tunable platform for optical applications. *Nature chemistry*, 2(12), 1015-1024.
- Lu, B., Chen, H., Jiang, M., Chen, X., Ren, Z., & Bai, J. (2013). Graphene-based passive Q-switching for a 2 μ m thulium-doped fiber laser. *Laser Physics*, 23(4), 045111.
- Luo, Z., Zhou, M., Weng, J., Huang, G., Xu, H., Ye, C., & Cai, Z. (2010). Graphene-based passively Q-switched dual-wavelength erbium-doped fiber laser. *Optics letters*, 35(21), 3709-3711.
- Marcano, D. C., Kosynkin, D. V., Berlin, J. M., Sinitskii, A., Sun, Z., Slesarev, A., ... & Tour, J. M. (2010). Improved synthesis of graphene oxide. *ACS nano*, 4(8), 4806-4814.
- Martinez, A., Fuse, K., Xu, B., & Yamashita, S. (2010). Optical deposition of graphene and carbon nanotubes in a fiber ferrule for passive mode-locked lasing. *Optics express*, 18(22), 23054-23061.
- McAllister, M. J., Li, J. L., Adamson, D. H., Schniepp, H. C., Abdala, A. A., Liu, J., ... & Aksay, I. A. (2007). Single sheet functionalized graphene by oxidation and thermal expansion of graphite. *Chemistry of Materials*, 19(18), 4396-4404.
- Medhekar, N. V., Ramasubramaniam, A., Ruoff, R. S., & Shenoy, V. B. (2010). Hydrogen bond networks in graphene oxide composite paper: structure and mechanical properties. *Acs Nano*, 4(4), 2300-2306.
- Mei, Q., Zhang, K., Guan, G., Liu, B., Wang, S., & Zhang, Z. (2010). Highly efficient photoluminescent graphene oxide with tunable surface properties. *Chem. Commun.*, 46(39), 7319-7321.
- Michelangeli, G. B., Giuliani, G., Palange, E., & Penco, E. (1986). Q switching and cavity dumping of a high-power cw Nd: YAG laser by means of a novel electro-optic configuration. *Optics letters*, 11(6), 360-362.

- Mills, A. F. (1999). *Basic heat and mass transfer*. Pearson College Div.
- Moghaddam, M. R. A., Harun, S. W., Akbari, R., & Ahmad, H. (2011). Stable mode-locked fiber laser using 49 cm long bismuth oxide based erbium doped fiber and slow saturable absorber. *Laser Physics*, 21(5), 913-918.
- Mohiuddin, T. M. G., Lombardo, A., Nair, R. R., Bonetti, A., Savini, G., Jalil, R., ... & Ferrari, A. C. (2009). Uniaxial strain in graphene by Raman spectroscopy: G peak splitting, Grüneisen parameters, and sample orientation. *Physical Review B*, 79(20), 205433.
- Moon, D., Paek, U. C., & Chung, Y. (2005). Polarization controlled multi-wavelength Er-doped fiber laser using fiber Bragg grating written in few-mode side-hole fiber with an elliptical core. *Optics express*, 13(14), 5574-5579.
- Nakazawa, M., Nakahara, S., Hirooka, T., Yoshida, M., Kaino, T., & Komatsu, K. (2006). Polymer saturable absorber materials in the 1.5 μm band using polymethyl-methacrylate and polystyrene with single-wall carbon nanotubes and their application to a femtosecond laser. *Optics letters*, 31(7), 915-917.
- Ng, S. H., Wang, J., Guo, Z. P., Chen, J., Wang, G. X., & Liu, H. K. (2005). Single wall carbon nanotube paper as anode for lithium-ion battery. *Electrochimica Acta*, 51(1), 23-28.
- Nicholson, J. W., Windeler, R. S., & DiGiovanni, D. J. (2007). Optically driven deposition of single-walled carbon-nanotube saturable absorbers on optical fiber end-faces. *Optics express*, 15(15), 9176-9183.
- Novoselov, K. S., Geim, A. K., Morozov, S. V., Jiang, D., Zhang, Y., Dubonos, S. A., ... & Firsov, A. A. (2004). Electric field effect in atomically thin carbon films. *science*, 306(5696), 666-669.
- Okhotnikov, O., Grudinin, A., & Pessa, M. (2004). Ultra-fast fibre laser systems based on SESAM technology: new horizons and applications. *New journal of physics*, 6(1), 177.
- Pacilé, D., Meyer, J. C., Rodríguez, A. F., Papagno, M., Gomez-Navarro, C., Sundaram, R. S., ... & Kaiser, U. (2011). Electronic properties and atomic structure of graphene oxide membranes. *Carbon*, 49(3), 966-972.

- Paredes, J. I., Villar-Rodil, S., Solis-Fernandez, P., Martinez-Alonso, A., & Tascon, J. M. D. (2009). Atomic force and scanning tunneling microscopy imaging of graphene nanosheets derived from graphite oxide. *Langmuir*, 25(10), 5957-5968.
- Piazza, R. (2008). Thermophoresis: moving particles with thermal gradients. *Soft Matter*, 4(9), 1740-1744.
- Pradhan, S., Town, G. E., & Grant, K. J. (2006). Microwave frequency generation using a dual-wavelength DBR fiber laser.
- Pushparaj, V. L., Shaijumon, M. M., Kumar, A., Murugesan, S., Ci, L., Vajtai, R., ... & Ajayan, P. M. (2007). Flexible energy storage devices based on nanocomposite paper. *Proceedings of the National Academy of Sciences*, 104(34), 13574-13577.
- Qin-Yong, Z., Yong, W., Ji-Chuan, X., & Da-Yong, Z. (2011). Modeling the pulse shape of Q-switched lasers to account for terminal-level relaxation. *Chinese Physics B*, 20(3), 034204.
- Reich, S., & Thomsen, C. (2004). Raman spectroscopy of graphite. *Philosophical Transactions of the Royal Society of London A: Mathematical, Physical and Engineering Sciences*, 362(1824), 2271-2288.
- Reina, A., Jia, X., Ho, J., Nezich, D., Son, H., Bulovic, V., ... & Kong, J. (2008). Large area, few-layer graphene films on arbitrary substrates by chemical vapor deposition. *Nano letters*, 9(1), 30-35.
- Sakakibara, Y., Rozhin, A. G., Kataura, H., Achiba, Y., & Tokumoto, M. (2005). Carbon nanotube-poly (vinylalcohol) nanocomposite film devices: Applications for femtosecond fiber laser mode lockers and optical amplifier noise suppressors. *Japanese journal of applied physics*, 44(4R), 1621.
- Saleh, B. E. A., Teich, M. C., & Saleh, B. E. (1991). *Fundamentals of photonics* (Vol. 22). New York: Wiley.
- Salem, A. R., Al-Mansoori, M. H., Hizam, H., Noor, S. M., & Mahdi, M. A. (2011). Broadly tunable multiwavelength fiber laser with bismuth-oxide EDF using large effective area fiber. *Laser Physics*, 21(2), 389-394.
- Savastru, D., Savastru, R., Miclos, S., & Lancranjan, I. (2013). Numerical Analysis of Passively Q-switched Er and Yb Doped Fiber Laser. *analysis*, 16, 18.

- Savastru, D., Miclos, S., & Lancranjan, I. (2012). Theoretical analysis of a passively q-switched erbium doped fiber laser. *Revista de Tehnologii Neconventionale*, 16(1), 47.
- Schießl, K., Babick, F., & Stintz, M. (2012). Calculation of double layer interaction between colloidal aggregates. *Advanced Powder Technology*, 23(2), 139-147.
- Seabra, A. B., Paula, A. J., de Lima, R., Alves, O. L., & Duran, N. (2014). Nanotoxicity of graphene and graphene oxide. *Chemical research in toxicology*, 27(2), 159-168.
- Set, S. Y., Yaguchi, H., Tanaka, Y., & Jablonski, M. (2004). Laser mode locking using a saturable absorber incorporating carbon nanotubes. *Lightwave Technology, Journal of*, 22(1), 51-56.
- Shahi, S., Harun, S. W., & Ahmad, H. (2009). Multi-wavelength Brillouin fiber laser using a holey fiber and a bismuth-oxide based erbium-doped fiber. *Laser Physics Letters*, 6(6), 454.
- Shang, J., Ma, L., Li, J., Ai, W., Yu, T., & Gurzadyan, G. G. (2012). The origin of fluorescence from graphene oxide. *Scientific reports*, 2.
- Shang, J., Ma, L., Li, J., Ai, W., Yu, T., & Gurzadyan, G. G. (2014). Femtosecond pump-probe spectroscopy of graphene oxide in water. *Journal of Physics D: Applied Physics*, 47(9), 094008.
- Sharma, U., Kim, C. S., Kang, J. U., & Fried, N. M. (2004, February). Highly stable tunable dual-wavelength Q-switched fiber laser for DIAL applications. In *Laser Applications to Chemical and Environmental Analysis* (p. MB3). Optical Society of America.
- Skorczakowski, M., Swiderski, J., Pichola, W., Nyga, P., Zajac, A., Maciejewska, M., ... & Bragagna, T. (2010). Mid-infrared Q-switched Er: YAG laser for medical applications. *Laser Physics Letters*, 7(7), 498.
- Sobon, G., Sotor, J., Jagiello, J., Kozinski, R., Zdrojek, M., Holdynski, M., ... & Abramski, K. M. (2012). Graphene oxide vs. reduced graphene oxide as saturable absorbers for Er-doped passively mode-locked fiber laser. *Optics express*, 20(17), 19463-19473.
- Spühler, G. J., Paschotta, R., Fluck, R., Braun, B., Moser, M., Zhang, G., ... & Keller, U. (1999). Experimentally confirmed design guidelines for passively Q-switched

microchip lasers using semiconductor saturable absorbers. *JOSA B*, 16(3), 376-388.

Stankovich, S., Dikin, D. A., Compton, O. C., Dommett, G. H., Ruoff, R. S., & Nguyen, S. T. (2010). Systematic post-assembly modification of graphene oxide paper with primary alkylamines. *Chemistry of Materials*, 22(14), 4153-4157.

Stankovich, S., Dikin, D. A., Dommett, G. H., Kohlhaas, K. M., Zimney, E. J., Stach, E. A., ... & Ruoff, R. S. (2006). Graphene-based composite materials. *Nature*, 442(7100), 282-286.

Stankovich, S., Dikin, D. A., Piner, R. D., Kohlhaas, K. A., Kleinhammes, A., Jia, Y., ... & Ruoff, R. S. (2007). Synthesis of graphene-based nanosheets via chemical reduction of exfoliated graphite oxide. *Carbon*, 45(7), 1558-1565.

Staudenmaier, L. (1898). Verfahren zur darstellung der graphitsäure. *Berichte der deutschen chemischen Gesellschaft*, 31(2), 1481-1487.

Stauber, T., Peres, N. M. R., & Geim, A. K. (2008). Optical conductivity of graphene in the visible region of the spectrum. *Physical Review B*, 78(8), 085432.

Stöppler, G., Kieleck, C., & Eichhorn, M. (2010, October). High-pulse energy Q-switched Tm^{3+} : YAG laser for nonlinear frequency conversion to the mid-IR. In *Security+ Defence* (pp. 783609-783609). International Society for Optics and Photonics.

Sugimoto, N. (2005, March). Recent progress in Bi-EDF technologies. In *Optical Fiber Communication Conference* (p. OWF6). Optical Society of America.

Sun, Z., Popa, D., Hasan, T., Torrisi, F., Wang, F., Kelleher, E. J., ... & Ferrari, A. C. (2010). A stable, wideband tunable, near transform-limited, graphene-mode-locked, ultrafast laser. *Nano Research*, 3(9), 653-660.

Svelto, O., & Hanna, D. C. (1998). Principles of lasers, 4-th ed.

Szabó, T., Tombácz, E., Illés, E., & Dékány, I. (2006). Enhanced acidity and pH-dependent surface charge characterization of successively oxidized graphite oxides. *Carbon*, 44(3), 537-545.

- Tang, Y., Yang, Y., Xu, J., & Hang, Y. (2008). Passive Q-switching of short-length Tm³⁺-doped silica fiber lasers by polycrystalline Cr²⁺: ZnSe microchips. *Optics Communications*, 281(22), 5588-5591.
- Tang, Y., Huang, C., Wang, S., Li, H., & Xu, J. (2012). High-power narrow-bandwidth thulium fiber laser with an all-fiber cavity. *Optics express*, 20(16), 17539-17544.
- Tan, S. J., Harun, S. W., Ali, N. M., Ismail, M. A., & Ahmad, H. (2013). A multi-wavelength Brillouin erbium fiber laser with double Brillouin frequency spacing and Q-switching characteristics. *Quantum Electronics, IEEE Journal of*, 49(7), 595-598.
- Tao, Z., Ruichang, Y., & Dounan, J. (2005). Analysis on thermophoretic deposit of fine particle on water wall of 10 MW high temperature gas-cooled reactor. *核技术*, 16(1).
- Tu, C., Guo, W., Li, Y., Zhang, S., Zhu, H., & Lu, F. (2008). Multiwavelength YB-doped fiber ring laser based on a Mach-Zehnder interferometer. *Microwave and Optical Technology Letters*, 50(3), 723-725.
- Vicente, S. C., Gamez, M. M., Kir'yanov, A. V., Barmenkov, Y. O., & Andres, M. V. (2004). Diode-pumped self-Q-switched erbium-doped all-fibre laser. *Quantum electronics*, 34(4), 310.
- Von der Linde, D. (1986). Characterization of the noise in continuously operating mode-locked lasers. *Applied Physics B*, 39(4), 201-217.
- Wagner, W. G., & Lengyel, B. A. (1963). Evolution of the giant pulse in a laser. *Journal of Applied Physics*, 34(7), 2040-2046.
- Waje, M. M., Wang, X., Li, W., & Yan, Y. (2005). Deposition of platinum nanoparticles on organic functionalized carbon nanotubes grown in situ on carbon paper for fuel cells. *Nanotechnology*, 16(7), S395.
- Wang, F., Torrisi, F., Jiang, Z., Popa, D., Hasan, T., Sun, Z., ... & Ferrari, A. C. (2012, May). Graphene passively Q-switched two-micron fiber lasers. In *CLEO: Applications and Technology* (pp. JW2A-72). Optical Society of America.
- Wang, X., Chen, Y. P., & Nolte, D. D. (2008). Strong anomalous optical dispersion of graphene: complex refractive index measured by Picometrology. *Optics express*, 16(26), 22105-22112.

- Wei, Z., Wang, D., Kim, S., Kim, S. Y., Hu, Y., Yakes, M. K., ... & Riedo, E. (2010). Nanoscale tunable reduction of graphene oxide for graphene electronics. *Science*, 328(5984), 1373-1376.
- Würger, A. (2008). Transport in charged colloids driven by thermoelectricity. *Physical review letters*, 101(10), 108302.
- Würger, A. (2009). Temperature dependence of the Soret motion in colloids. *Langmuir*, 25(12), 6696-6701.
- Yagoh, H., Murayama, H., Suzuki, T., Tominaga, Y., Shibuya, N., & Masuda, Y. (2006). Simultaneous monitoring method of polycyclic aromatic hydrocarbons and persistent organic pollutants in the atmosphere using activated carbon fiber filter paper. *Analytical sciences*, 22(4), 583-590.
- Yamashita, S., Inoue, Y., Maruyama, S., Murakami, Y., Yaguchi, H., Jablonski, M., & Set, S. Y. (2004). Saturable absorbers incorporating carbon nanotubes directly synthesized onto substrates and fibers and their application to mode-locked fiber lasers. *Optics letters*, 29(14), 1581-1583.
- Yang, H., Hu, H., Wang, Y., & Yu, T. (2013). Rapid and non-destructive identification of graphene oxide thickness using white light contrast spectroscopy. *Carbon*, 52, 528-534.
- Yan, J. A., Xian, L., & Chou, M. Y. (2009). Structural and electronic properties of oxidized graphene. *Physical review letters*, 103(8), 086802.
- Yan, J. A., & Chou, M. Y. (2010). Oxidation functional groups on graphene: Structural and electronic properties. *Physical Review B*, 82(12), 125403.
- Zayhowski, J. J., & Kelley, P. L. (1991). Optimization of Q-switched lasers. *Quantum Electronics, IEEE Journal of*, 27(9), 2220-2225.
- Zhang, L., Liang, J., Huang, Y., Ma, Y., Wang, Y., & Chen, Y. (2009). Size-controlled synthesis of graphene oxide sheets on a large scale using chemical exfoliation. *Carbon*, 47(14), 3365-3368.
- Zhang, W. L., Liu, Y. D., & Choi, H. J. (2011). Graphene oxide coated core-shell structured polystyrene microspheres and their electrorheological characteristics under applied electric field. *Journal of Materials Chemistry*, 21(19), 6916-6921.

- Zhao, J., Pei, S., Ren, W., Gao, L., & Cheng, H. M. (2010). Efficient preparation of large-area graphene oxide sheets for transparent conductive films. *Acs Nano*, 4(9), 5245-5252.
- Zhao, H., Lou, Q., Zhou, J., Zhang, F., Dong, J., Wei, Y., & Wang, Z. (2007). Stable pulse-compressed acousto-optic Q-switched fiber laser. *Optics letters*, 32(19), 2774-2776.
- Zhao, Y., Tang, G. S., Yu, Z. Z., & Qi, J. S. (2012). The effect of graphite oxide on the thermoelectric properties of polyaniline. *Carbon*, 50(8), 3064-3073.
- Zhao, S., Surwade, S. P., Li, Z., & Liu, H. (2012). Photochemical oxidation of CVD-grown single layer graphene. *Nanotechnology*, 23(35), 355703.
- Zhou, Y., Bao, Q., Varghese, B., Tang, L. A. L., Tan, C. K., Sow, C. H., & Loh, K. P. (2010). Microstructuring of graphene oxide nanosheets using direct laser writing. *Advanced Materials*, 22(1), 67-71.

LIST OF PUBLICATIONS AND PAPERS PRESENTED

Journals

- 1) Ahmad, H., Zulkifli, A. Z., Kiat, Y. Y., & Harun, S. W. (2014). Q-switched fibre laser using 21cm Bismuth-erbium doped fibre and graphene oxide as saturable absorber. *Optics Communications*, 310, 53-57.
- 2) Ahmad, H., Zulkifli, A. Z., Thambiratnam, K., & Harun, S. W. (2013). 2.0-Q-Switched Thulium-Doped Fiber Laser With Graphene Oxide Saturable Absorber. *Photonics Journal, IEEE*, 5(4), 1501108-1501108.
- 3) Ahmad, H., Zulkifli, A. Z., Thambiratnam, K., & Harun, S. W. (2013). Q-switched Zr-EDF laser using single-walled CNT/PEO polymer composite as a saturable absorber. *Optical Materials*, 35(3), 347-352.

Conference

- 1) Zulkifli, A. Z., Thambiratnam, K., Ahmad, F., Ahmad, H., S.W. Harun, S. W., (2012). Single Walled CNT / PEO based Saturable Absorber with Zr-EDF for Passively Q- Switched Pulse Laser Generation. Conference: Asia-Oceania Top University League on Engineering (AOTULE) 2012 Student conference, University of Malaya.

Seminars

- 1) Zulkifli, A. Z., Ahmad, H., and Harun, S. W. (31 July 2013). 2 μ m Q-switched Thulium-doped Fiber Laser with Graphene Oxide as Saturable Absorber. Department of Electrical Engineering, Faculty of Engineering, University of Malaya, 50603 Kuala Lumpur,
- 2) Zulkifli, A. Z., Ahmad, H., and Harun, S. W. (10 September 2014). Fabrication Techniques and Characterization of Graphene Oxide Saturable

Absorbers For Q-switching. Department of Electrical Engineering, Faculty of Engineering, University of Malaya, 50603 Kuala Lumpur.